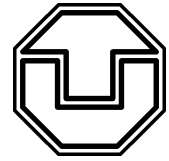


Institut für Biophysik
Fachrichtung Physik
Fakultät Mathematik und Naturwissenschaften
der Technischen Universität Dresden



Mechanics and dynamics of twisted DNA

Dissertation
zur Erlangung des akademischen Grades
Doctor rerum naturalium
(Dr. rer. nat.)

vorgelegt von
Hergen Brutzer
geboren am 06. März 1982 in Oldenburg

November 2012

1. Gutachter: Prof. Dr. Stefan Diez
2. Gutachter: Prof. Dr. Klaus Kroy

Tag der Einreichung: 29. November 2012

Tag der Verteidigung: 04. März 2013

Kurzfassung

Aufgrund einer komplexen Wechselwirkung mit Proteinen ist das Genom in einer Zelle ständig mechanischer Spannung und Torsion ausgesetzt. Daher ist es wichtig die Mechanik und die Dynamik von verdrillter DNA unter Spannung zu verstehen. Diese Situation wurde experimentell mittels einer sog. magnetischen Pinzette nachgestellt, indem sowohl Kraft als auch Drehmoment auf ein einzelnes DNA Molekül ausgeübt und gleichzeitig die mechanische Antwort des Polymers aufgezeichnet wurde.

Als erstes Beispiel wurde der Übergang von linearer zu sog. plectonemischer DNA untersucht, d.h. die Absorption eines Teils der induzierten Verdrillung in einer superhelikalen Struktur. Eine abrupte Längenänderung am Anfang dieses Übergangs wurde bereits im Vorfeld publiziert. In der vorliegenden Arbeit wird gezeigt, dass diese abrupte DNA Verkürzung insbesondere von der Länge der DNA und der Ionenkonzentration der Lösung abhängt. Dieses Verhalten kann mittels eines Modells verstanden werden, in dem die Energie pro Verwindung der ersten Schlinge innerhalb der Superhelix größer ist als die aller nachfolgenden.

Des Weiteren wurden DNA-DNA Wechselwirkungen in der Umgebung monovalenter Ionen durch die Analyse des Superspiralisierungsverhaltens einzelner DNA Moleküle bei konstanter Kraft charakterisiert. Solche Wechselwirkungen sind für die Kompaktierung des Genoms und die Regulation der Transkription wichtig. Oft wird DNA als gleichmäßig geladener Zylinder modelliert und ihre elektrostatischen Wechselwirkungen im Rahmen der Poisson-Boltzmann-Gleichung mit einem Ladungsanpassungsfaktor berechnet. Trotz erheblicher Anstrengung ist eine präzise Bestimmung dieses Parameters bisher nicht gelungen. Ein theoretisches Modell dieses Prozesses zeigte nun eine erstaunlich kleine effektive DNA Ladung von $\sim 40\%$ der nominalen Ladungsdichte.

Abgesehen von Gleichgewichtsprozessen wurde auch die Dynamik eines Faltungsvorgangs von DNA untersucht. Spontane Branch Migration einer homologen Holliday-Struktur wurde genutzt, um die intramolekulare Reibung der DNA zu erforschen. Mittels einer magnetischen Pinzette wurde eine torsionslimitierte Holliday-Struktur gestreckt während die Längenfluktuationen der Zweige mit schneller Videomikroskopie bei ~ 3 kHz aufgezeichnet wurden. Einzelne diffusive Schritte der Basenpaare sollten auf einer sub-Millisekunden Zeitskala auftreten und viel kleiner als die Gesamtfluktuationen der DNA sein. Eine Analyse der spektralen Leistungsdichte der Längenfluktuationen ermöglicht eine eindeutige Beschreibung der Dynamik der Branch Migration.

Die Holliday-Struktur wurde außerdem als nanomechanischer Linearverstärker eingesetzt, um einen einzelnen fluoreszierenden Quantenpunkt durch ein exponentiell abfallendes evaneszentes Feld zu bewegen. Durch die Aufzeichnung der Emission des Quantenpunkts sowohl in dem evaneszenten Feld als auch unter gleichmäßiger Beleuchtung kann die Intensitätsverteilung des Anregungsfelds ohne weitere Dekonvolution bestimmt werden. Diese neue Technik ist von besonderem wissenschaftlichen Interesse, weil die Beschreibung dreidimensionaler inhomogener Beleuchtungsfelder eine große Herausforderung in der modernen Mikroskopie darstellt.

Die Ergebnisse dieser Arbeit werden dem besseren Verständnis einer Vielzahl biologischer Prozesse, die in Verbindung mit DNA Superspiralisierung stehen, dienen und weitere technische Anwendungen des DNA-basierten Linearverstärkers hervorbringen.

Abstract

The genome inside the cell is continuously subjected to tension and torsion primarily due to a complex interplay with a large variety of proteins. To gain insight into these processes it is crucial to understand the mechanics and dynamics of twisted DNA under tension. Here, this situation is mimicked experimentally by applying force and torque to a single DNA molecule with so called magnetic tweezers and measuring its mechanical response.

As a first example a transition from a linear to a plectonemic DNA configuration is studied, i.e. the absorption of part of the applied twist in a superhelical structure. Recent experiments revealed the occurrence of an abrupt extension change at the onset of this transition. Here, it is found that this abrupt DNA shortening strongly depends on the length of the DNA molecule and the ionic strength of the solution. This behavior can be well understood in the framework of a model in which the energy per writhe for the initial plectonemic loop is larger than for subsequent turns of the superhelix.

Furthermore DNA-DNA interactions in the presence of monovalent ions were comprehensively characterized by analyzing the supercoiling behavior of single DNA molecules held under constant tension. These interactions are important for genome compaction and transcription regulation. So far DNA is often modeled as a homogeneously charged cylinder and its electrostatic interactions are calculated within the framework of the Poisson-Boltzmann equation including a charge adaptation factor. Despite considerable efforts, until now a rigorous quantitative assessment of this parameter has been lacking. A theoretical model of this process revealed a surprisingly small effective DNA charge of $\sim 40\%$ of the nominal charge density.

Besides describing equilibrium processes, also the dynamics during refolding of nucleic acids is investigated. Spontaneous branch migration of a homologous Holliday junction serves as an ideal system where the friction within the biomolecule can be studied. This is realized by stretching a torsionally constrained Holliday junction using magnetic tweezers and recording the length fluctuations of the arms with high-speed videomicroscopy at ~ 3 kHz. Single base pair diffusive steps are expected to occur on a sub-millisecond time scale and to be much smaller than the overall DNA length fluctuations. Power-spectral-density analysis of the length fluctuations is able to clearly resolve the overall dynamics of the branch migration process.

Apart from studying intramolecular friction, the four-arm DNA junction was also used as a nanomechanical translation stage to move a single fluorescent quantum dot through an exponentially decaying evanescent field. Recording the emission of the quantum dot within the evanescent field as well as under homogeneous illumination allows to directly obtain the intensity distribution of the excitation field without additional deconvolution. This new technique is of particular scientific interest because the characterization of three-dimensional inhomogeneous illumination fields is a challenge in modern microscopy.

The results presented in this work will help to better understand a large variety of biological processes related to DNA supercoiling and inspire further technical applications of the nanomechanical DNA gear.

Contents

1. The importance of DNA supercoiling	7
2. Manipulating DNA with magnetic tweezers	13
2.1. Instrument design	13
2.1.1. Basic principles	13
2.1.2. Increasing the resolution of magnetic tweezers	15
2.2. Resolving length changes of DNA with Ångström accuracy	17
2.2.1. Resolution limits of the instrument	17
2.2.2. Resolving length changes of DNA	20
2.3. Using Brownian motion to measure force	24
2.3.1. Force dependence of the fluctuations	24
2.3.2. Determination of the mean square displacement	25
3. The DNA buckling transition	29
3.1. DNA supercoiling under tension	29
3.2. Understanding the buckling transition	31
3.2.1. Abrupt buckling measured with magnetic tweezers	31
3.2.2. The width of the buckling transition	31
3.2.3. Kinetics of the buckling transition	34
3.2.4. End loop model for abrupt buckling	35
3.2.5. Estimating the plectoneme formation energies	37
3.2.6. Force dependence of the buckling transition	40
3.2.7. Salt dependence of the buckling transition	42
3.2.8. Supercoiling kinked DNA	43
3.3. Consequences of DNA buckling	45
3.3.1. End loop provides a plectoneme nucleation barrier	45
3.3.2. Plectoneme pinning and energy of DNA bending	46
4. The effective charge of DNA	47
4.1. Challenges in quantifying DNA-DNA interactions	47
4.2. Energetic considerations	47
4.3. An adapted DNA charge describes the experimental findings	52
4.3.1. Comparing the model to the slopes of the supercoiling curves	52
4.3.2. Verification of the model via Monte Carlo simulations	53
4.3.3. Molecular dynamics simulations allow a microscopic insight	55
4.4. Effects from fluctuations	57
4.4.1. Verification of the applied parameters	57
4.4.2. Applying additional entropic energy terms	59
4.4.3. Fluctuations within stretched vs. superhelical DNA	61

4.4.4. Justification of the model neglecting fluctuations	62
4.5. Previous investigations of DNA-DNA interactions	63
4.6. DNA mechanics for various monovalent electrolytes	65
4.6.1. Dependence of the bending rigidity on the type of counterion .	65
4.6.2. DNA supercoiling for different alkaline counterions	67
5. Internal friction of a migrating Holliday junction	71
5.1. Insights into the dynamics of branch migration	71
5.1.1. Dynamics of structural transitions in nucleic acids	71
5.1.2. Monitoring branch migration with magnetic tweezers	72
5.2. Coupled displacement of DNA translation and migration	74
5.2.1. Calculating the range of the branch migration	74
5.2.2. Power spectral density of a coupled system	75
5.2.3. Determination of the time per spontaneous migration step . .	78
5.3. Experimental determination of the friction coefficient	78
5.4. Intramolecular friction in other single molecule assays	81
6. Using DNA as a nanomechanical gear	83
6.1. Characterization of inhomogeneous illumination fields	83
6.2. Components of the biological nano translation stage	86
6.3. Determination of the angle of incidence	87
6.4. Scanning evanescent fields using a pointlike light source	88
7. Conclusion	95
Bibliography	99
List of Figures	109
List of Publications	111
Abbreviations and nomenclature	113
Appendix	119
A. Preparation of the fluidic chamber	121
B. DNA substrate preparation	123
B.1. DNA buckling transition and effective charge studies	123
B.2. Intramolecular friction of a migrating Holliday junction	123
B.3. DNA Holliday junction as a nanomechanical gear	124

1. The importance of DNA supercoiling

The genetic information that encodes the development and functioning of all living organisms is stored in the form of double-stranded deoxyribonucleic acid (dsDNA). The diameter of dsDNA is approximately 2.4 nm, however the length is typically several orders of magnitude larger. The largest human chromosome, for instance, is approximately 220 million base pairs long. If untangled and stretched this corresponds to a length of 7.3 cm, which is much larger than the size of most cells. In eukaryotes the DNA needs to be compacted in order to fit into the nucleus. This compaction is realized by wrapping the DNA around protein complexes forming nucleosomes consisting of histones. Although the genome in prokaryotes is not confined in a nucleus, the circular DNA is compacted by a high degree of negative supercoiling and histone-like proteins. The existence of supercoiled DNA was established by electron microscopy and sedimentation studies in the mid-1960s [1].

The focus of this work is on the mechanical and dynamic response of supercoiled DNA. In mathematics the concept of supercoiling is part of the ribbon theory and is not limited to DNA. The degree of supercoiling refers to the over- or underwinding of a ribbon. Depending on external factors such as the interaction potential between the ribbons, the response of the ribbon to supercoiling varies between two modes (Fig. 1.1). Applied turns can be stored in the form of twist, i.e. the rate of rotation of the ribbon around its axis (Fig. 1.1b). Alternatively the ribbon can vary its amount of writhe, which is defined as a measure of the non-planarity of the ribbon's axis curve. In other words, the amount of writhe corresponds to the average number of crossings of the ribbon that can be detected when observing it from all spatial orientations (Fig. 1.1c).

In the literature the term “supercoil” is sometimes used as a synonym for writhe. This might originate from the etymology of the word, because the prefix “super” indicates that the size of the coils (for DNA typically 50 nm) is much larger than the helix repeat of the molecule itself (for DNA 3.4 nm). Throughout this work, the change of the linking number will be referred to as supercoiling, which is the more popular nomenclature.

Under certain conditions the ribbon may change the distribution of the total amount of supercoiling between twist and writhe for a given amount of over- or underwinding. One such example is the buckling transition of DNA explained in detail in chapter 3. For molecules with a helical structure such as DNA, the sign of the supercoiling is defined with respect to the molecule's helicity. If the induced turns are oriented in the same sense as the helix, supercoils are defined to be positive. Otherwise supercoils will be negative.

In vivo, DNA is mostly present in “B” form [2], which was described by James D. Watson and Francis Crick [3]. In this configuration, the sense of the double helix is right-handed and makes one complete turn around its axis every 10.5 base pairs in solution. This is referred to as the helical pitch. Therefore, if 10 base pairs are

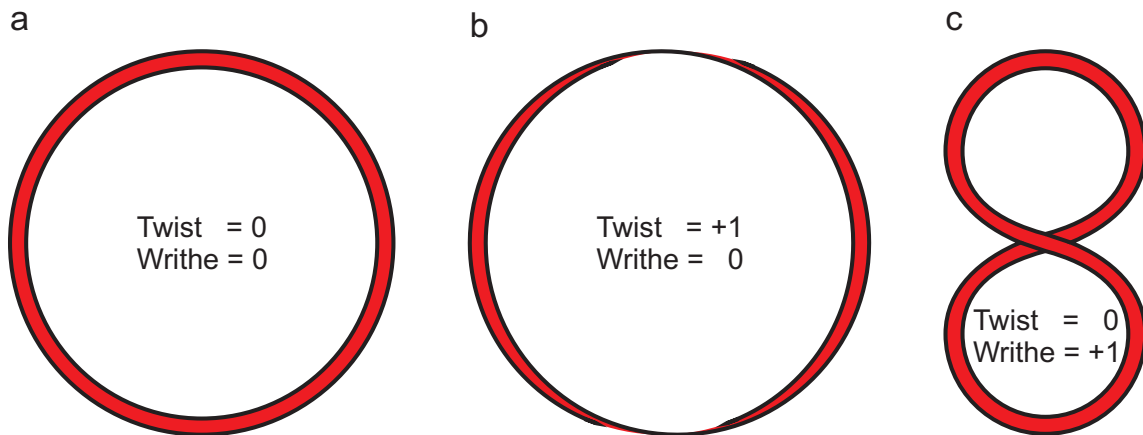


Figure 1.1. Supercoiling of a circular ribbon. (a) Over and underwinding of the ribbon is referred to as supercoiling. The degree of supercoiling is defined as the sum of twist and writhe. (b) Increasing the degree of supercoiling but leaving the ribbon in its circular shape augments the twist. (c) If the writhe, i.e. the number of crossings of the ribbon with itself, increases the torsion is reduced.

unwound, for instance by a helicase enzyme, almost one turn is induced in the DNA.

The interplay between biological function and the state of supercoiling of DNA seems to be omnipresent in the cell. Recently it has been suggested that all DNA transactions in the cell are linked to supercoiling [4]. As a consequence, over- or underwinding would serve as a regulatory signal detected by protein partners, which could contribute to the regulation of many events occurring during cell life.

One illustrating example is the state of gene expression. The expression of some genes in *Escherichia coli* has been shown to crucially depend on the degree of supercoiling of its genome [5]. This bacterium tries to maintain its chromosome in a negatively supercoiled state [6]. If the degree of supercoiling increases, genes are expressed that encode gyrases. These enzymes are able to counteract positive supercoiling by introducing negative supercoils [7]. If, on the contrary, the chromosome is more negatively supercoiled than in its native state, topoisomerase genes are expressed. These enzymes can reduce the amount of torsion by nicking one of the backbone strands. Therefore there seems to be a mutual correlation between supercoiling and gene expression.

On the molecular level, this dependence can be explained by considering how transcription is related to supercoiling. In this process a DNA molecule is transcribed into RNA. An RNA polymerase binds to the DNA and initiates the transcription by pulling the double strand apart over a short stretch to form the so called transcription bubble [8]. Now the polymerization is initiated. Often, the newly synthesized messenger RNA (mRNA) is directly translated by a ribosome into the corresponding sequence of amino acids. Some translated proteins can be integrated immediately in the membrane of the cell, serving as an anchor of the RNA polymerase. Therefore the enzyme is impeded from rotating around the DNA [9], such that positive supercoils are induced in front of the transcription bubble and negative ones behind.

To reduce this torsion topoisomerase I is able to covalently bind to one of the phosphate backbones of the DNA. This breaks the phosphodiester bond of the DNA backbone and thus creates a nick. Now the DNA can swivel around the covalent backbone bond of the opposite strand and remove torsional stress. The reaction is reversible, i.e. the phosphodiester bond reforms as the enzyme leaves, which seals the nick.

Topoisomerases also play an important role in genome replication and cell division [10]: If excessive supercoils were not removed, daughter chromosomes might entangle and chromosome segregation would be hindered.

DNA replication is also affected by supercoiling: In that process helicases bind to the DNA at the origins of replication and form a replication fork. In order for the DNA polymerases to start the copying process of the template strands, the helicase proceeds along the parent DNA by breaking the hydrogen bonds connecting the bases between the strands. As the DNA in front of the fork is relatively long, its high drag coefficient prevents the DNA from balancing the induced torsion by rotations around its axis. Similarly, the helicase-polymerase complex, which consists of several different proteins and is therefore also relatively large, cannot rotate. Therefore progression of the complex generates constant twist. This built-up twist would eventually cause the helicase to stop. Topoisomerases are necessary to remove the excess of twist in front of the polymerase.

Many other biological processes depend on supercoiling. In homologous recombination, the 3' overhang of a damaged DNA molecule and the Rad51 protein form a long filament. This single-stranded nucleoprotein filament invades a recipient DNA duplex with similar or identical sequence forming a displacement loop (D-loop). A Rad54 translocating motor attached to the Rad51 filament end induces supercoils into the template [11]. Negative supercoiling favors unpairing of double-stranded DNA, and thus D-loop formation. Changing the DNA structure by negative or positive supercoiling alters the affinity of DNA binding proteins, possibly resulting in the displacement of proteins that would otherwise block D-loop formation [12].

Furthermore, the degree of supercoiling is correlated to the juxtaposition and relative orientation of DNA sites. It has been shown that supercoiling can increase the probability of juxtaposition of two sites on the DNA by several orders of magnitude and cause an asymmetry in the distribution of their orientation [13]. This can have an influence on site-specific recombination, a type of genetic recombination used by bacteriophages in which DNA strand exchange takes place between segments possessing only a limited degree of sequence homology [14].

Also DNA transposition depends on the juxtaposition of two DNA sites, since for synaptic complex formation the ends of the transposable element have to be in close proximity. In addition, supercoiling favors binding of proteins to the DNA to form the nucleoprotein complex [15]. Furthermore an influence of overwinding on the cleavage of the ends has been reported [16].

As mentioned above the compaction of DNA in eukaryotic cells is realized by wrapping the DNA around nucleosomes. These nucleoprotein complexes constitute chromatin fibers. Each nucleosome is wrapped by DNA 1.65 times, which corresponds to the same amount of negative writhe. However, the overall supercoiling density is

only reduced by 1, because the remaining 0.65 turns increase the twist in the DNA. The cell can compensate for a change of twist in the genome by the association or dissociation of histones. Thus chromatin serves as a torsional buffer.

The wrapped DNA cannot diffuse to remote areas until released by nucleosome removal [17]. As a consequence of the chromatin organization, the majority of DNA supercoils is fixed in the eukaryotic genome and is known as constrained supercoil density. The unconstrained or diffusible supercoils must be accommodated within the linker DNA (regions separating the nucleosomes). The dynamic interplay between broadly distributed constrained supercoils and the local unconstrained supercoils in the eukaryotic genome is the underlying basis for many structural models of the nucleosome complex [18]. The ratio between constrained and diffusible supercoil density depends on the rates of gyrase supercoiling and transcription elongation [19].

The examples mentioned show that DNA supercoiling is important for a large variety of biological processes. To better understand how supercoiling contributes to cellular function, it is essential to know the mechanical response of DNA upon overtwisting. A breakthrough for this topic was accomplished more than a decade ago, when Croquette and coworkers showed how to twist a single DNA molecule under an applied tension using a technique called “magnetic tweezers” [20].

Many transitions that DNA undergoes during supercoiling as well as important supercoiling parameters have been carefully characterized and described. This includes structural transitions of B-DNA during supercoiling [21, 22], the torsional rigidity of DNA [23] as well as the twist-stretch coupling [24, 25], the direct measurement of torque during supercoiling [26, 27], and the dynamics of supercoil release [28].

In this thesis a transition was studied which occurs upon twisting DNA under tension. At a critical torque level the molecule undergoes a dynamic transition, the so called buckling, during which twist energy is transferred into writhe and vice versa. Magnetic tweezers were used to observe in real time how the DNA buckles, i.e. how it forms a superhelical structure (chapter 3).

The double strands of the DNA in this superhelical structure are in close proximity. As the DNA is charged the distance between the strands varies relative to the concentration of counterions in the buffer solution. The supercoiling assay presented in chapter 4 allows a direct measurement of the amount of DNA that is stored per superhelical turn, which can be translated into an effective linear charge density of the DNA. The charge is a fundamental property of DNA which governs its biological function by influencing DNA folding, packaging [29], pairing [30], and interactions with other biological macromolecules [31].

While the buckling transition and the effective charge in a DNA superhelix can be described by equilibrium quantities, *in vivo*, the supercoiled DNA structures are highly dynamic. Supercoils can be, for instance, created, propagated and removed on a DNA molecule. Studying the dynamics of supercoils with magnetic tweezers is, however, difficult since the friction between the double strands in a formed superhelix is small compared to the viscous drag of the magnetic microsphere to which the DNA is tethered [28]. Therefore a method is presented to study molecular friction, a non-equilibrium quantity, that occurs during fast, few nm-sized refolding processes of nucleic acids. Spontaneous branch migration of a homologous Holliday junction

which is torsionally confined in a magnetic tweezers assay serves as an ideal system where such friction can be investigated (chapter 5).

As the refolding processes are thought to occur in one base-pair steps possibly on a sub-millisecond time scale, the conventional magnetic tweezers instrument has been improved to increase the stability as well as the spatio-temporal resolution. The resolution limits of this new instrument are presented in chapter 2.

Based on the Holliday junction assay used to study molecular friction a DNA construct was developed which could be used as a nanomechanical translation stage to move a single fluorescent quantum dot through an exponentially decaying evanescent field (chapter 6). This practical application allowed to calibrate the penetration depth of the illumination in a total internal reflection geometry, however, can in principle be used to characterize a broad range of three-dimensional inhomogeneous illumination fields, which is a challenge in modern microscopy.

This demonstrates that DNA supercoiling can not only be used to study fundamental parameters and transitions on DNA but also be applied as a nanotechnological tool.

2. Manipulating DNA with magnetic tweezers

2.1. Instrument design

2.1.1. Basic principles

For many biological functions the compacted DNA needs to be accessible (see chapter 1). In vivo, the DNA can be compacted, locally unwound, and even cut by enzymes. This means that the DNA is constantly subjected to force and torque. This condition can be experimentally reconstructed by manipulating a single DNA molecule and observing its response to external influences. The technique used predominantly in this work is called magnetic tweezers.

The basic design of the magnetic tweezers instrument employed here is depicted in Fig. 2.1. Within a fluidic chamber a streptavidin-coated superparamagnetic microsphere 1 μm in diameter (MyOne, Invitrogen, Carlsbad, CA, USA) is tethered to a DNA molecule carrying biotinylated bases at one end. The other end of the DNA contains digoxigenin-modified bases so that a stable attachment to a glass surface coated with the corresponding antibody (Roche, Penzberg, Germany) is guaranteed.

Once the DNA molecule is anchored to the glass surface, force and torque can be induced in the nucleic acid by changing the distance and the angular orientation of a pair of permanent NdFeB magnets (W-05-N50-G, Supermagnete, Uster, Switzerland) relative to the fluidic chamber. To this end the permanent magnets are attached to two motorized stages. The magnetic bead follows the rotations of the permanent magnets because a magnetization anisotropy of the microsphere causes an alignment of its dipole moment with the field of the permanent magnets. If the DNA molecule is bound to the microsphere and the substrate surface via multiple linkers, rotations of the bead induce a torque in the nucleic acid.

The two most important parameters which can be determined with a conventional magnetic tweezers instrument are the extension of the DNA and the applied force. As the dimensions of the nucleic acid are too small to visualize the DNA in an ordinary light microscope, the magnetic microsphere is used as a probe. While the extension of the DNA can be determined directly from the vertical distance of the microsphere to the glass surface (see Fig. 2.1), the force is inferred from its lateral fluctuations (see section 2.3).

The position of the microsphere is detected using an inverted microscope and 3D particle tracking: The sample is illuminated through the gap between the magnets by a 660 nm light emitting diode (LED) which is focused via a system of lenses onto the sample. As the diameter of the microsphere is of the same order of magnitude as the wavelength used for illumination, the interference of the diffracted light waves results in a pattern (see Fig. 2.1). This diffraction pattern is directly used for the determination of the lateral coordinates by cross correlation techniques, which are

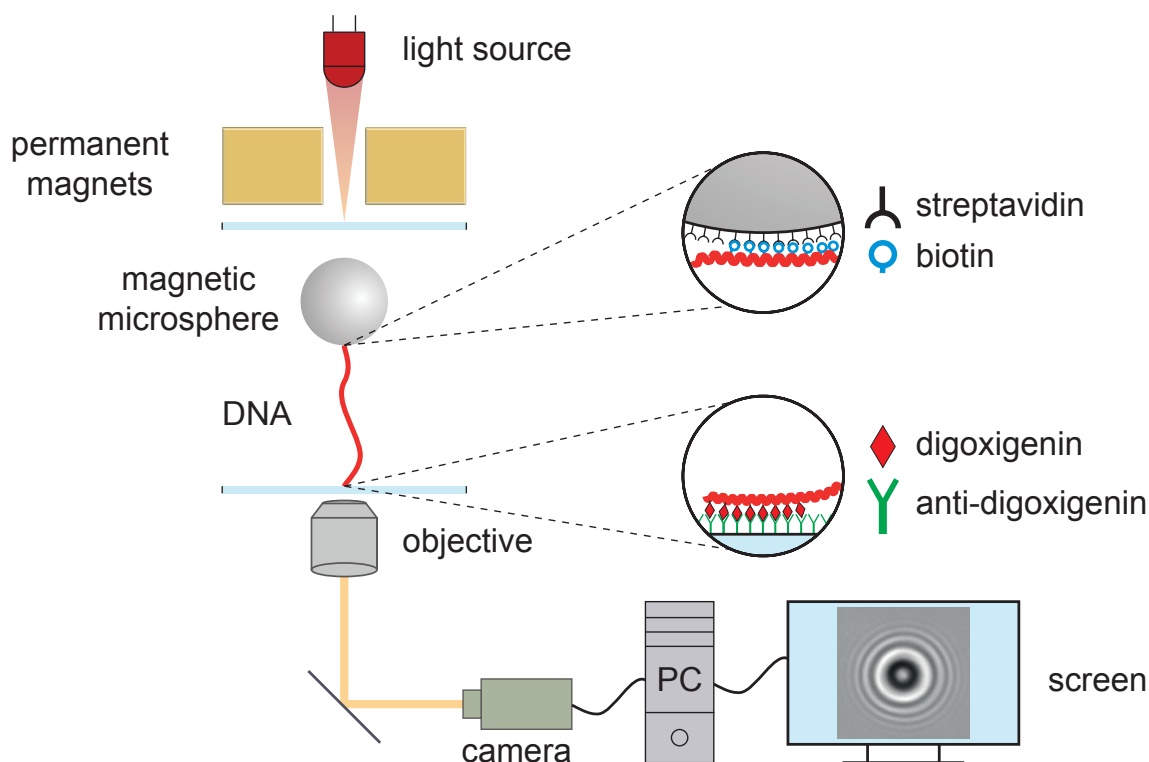


Figure 2.1. Schematic illustration of the magnetic tweezers apparatus. A DNA molecule is tethered between a glass surface and magnetic microsphere within a fluidic chamber. Permanent magnets above the chamber can be moved vertically in order to change the force exerted on the magnetic bead. The attachment of the DNA molecule to the glass slide and to the microsphere is realized via antibody-antigen and biotin-streptavidin modifications. The sample is illuminated by a light source and imaged via an objective on the chip of a CCD camera. A computer including a frame grabber is used to calculate the DNA extension and the force acting on the nucleic acid from the diffraction pattern of the microsphere.

based on Fourier transforming the recorded image. The axial position is extracted from the pattern following a calibration. The size of the circular pattern depends on the distance of the microsphere to the focus. To guarantee a high precision with a pronounced diffraction pattern the bead is imaged in overfocus by an oil-immersion objective located underneath the fluidic chamber. The corresponding tube lens is then positioned in the optical path such that the image is focused on the chip of a CCD-camera (TM-6710CL, JAI Pulnix Inc, San Jose, CA, USA). The focal position of the objective can be moved as it is mounted on a piezo scanner with sub-nanometer resolution (PIFOC P-721.CDQ, PI, Karlsruhe, Germany).

To correct for external noise the position of the magnetic bead is determined with respect to a non-magnetic reference microsphere attached to the surface of the fluidic chamber. Images of both beads are acquired simultaneously with a frequency of 120 Hz and are analyzed in real-time.

For the work presented in this thesis three different instruments were used. All of

them are custom-made and therefore constantly developed further in order to improve their stability and increase the resolution. The basic version of the magnetic tweezers instrument as shown schematically in Fig. 2.1 was used for most of the measurements presented in chapters 3 and 4. An instrument combining a fluorescence microscope with a magnetic tweezers apparatus was employed for the experiments performed in chapter 6. For a detailed description of this hybrid instrument see also Ref. 32.

2.1.2. Increasing the resolution of magnetic tweezers

The structure of double stranded DNA consists of regularly spaced base pairs connecting two phosphate backbones. In several biological processes, such as DNA replication and transcription, the hydrogen bonds between the bases are broken so that other molecules can gain access to the now single-stranded regions of the DNA. As the base-pairs constitute discrete entities, one expects to observe distinct changes in the structure of the DNA when following such processes in an experiment given a sufficient spatio-temporal resolution.

The magnetic tweezers instrument presented in this thesis allows to study the interaction between enzymes and DNA. In the corresponding assays the DNA is usually linearized, such that conformational variations of the DNA can be detected as a length change. To observe the extension variation of the DNA upon rupture of the hydrogen bonds connecting two bases, “base-pair resolution” is desired.

Assays have been described to follow the length change of DNA upon hairpin unwinding by a helicase with magnetic tweezers in real time [33]. In this configuration, unwinding of a base pair creates two regions of single stranded DNA. As the distance between two nucleotides corresponds to approximately 5.7 Å, one should expect a length change of approximately 1.1 nm. However, the spatio-temporal resolution of the instrument did not allow the observation of the opening of single base-pairs. Several improvements to the basic instrument described in section 2.1.1 were implemented with the aim to resolve length changes of the DNA on the few Ångström scale.* One aspect of this work was to find the resolution limits of the improved magnetic tweezers instrument.

The major disadvantage of typical video-tracking with a CCD camera is that it is relatively slow (up to 120 Hz) compared to position determination by means of quadrant photodiode detectors. Furthermore the resolution of camera based tracking is limited by the photo shot noise of its detector, which is associated with the particle nature of light. One advantage of camera based particle tracking compared to photodiode detectors is its simplicity and the ability to monitor several particles simultaneously. A method to target the DNA tethering to specific locations of the substrate has been published. Due to the high density of molecules on the substrate surface the position of up to 450 microspheres could be tracked in parallel [34].

Based on the advantage related to video-tracking a large effort has been made to minimize its limitations. To reduce the relative contribution of shot noise to the detected signal, the number of detected photons is maximized. This is realized by

*Improvements to the hardware were implemented by Daniel Klaue.

increasing the number of pixels used for the analysis of each image by using a large magnification. In addition, the acquisition speed is augmented. For this the CCD detector was replaced by a CMOS-camera (EoSens CL, Mikrotron, Unterschleißheim, Germany). With this camera two dimensional particle tracking at 10,000 frames per second with moderate accuracy has been reported [35]. To determine the axial coordinate of the microsphere with high precision many pixels should be analyzed in parallel. Therefore the calculations necessary for the tracking were transferred from the central processing unit (CPU) to the graphics processing unit (GPU) on the graphics card (GeForce GTX 480, Nvidia, Santa Clara, CA, USA). This is advantageous because the GPU is able to process many more operations in parallel than the CPU.[†] Currently simultaneous three dimensional tracking of two microspheres (each 160x160 pixels) can be performed at 3 kHz.

At acquisition rates larger than 500 Hz, the LED is not able to provide enough intensity to guarantee sufficient photon statistics. Therefore a mercury arc lamp (LSB610, LOT-Oriel, Darmstadt, Germany) was used to illuminate the sample.

To increase the mechanical stability the design of the instrument was also modified. Rather than the objective being mounted on a piezo scanner which can only be translated in the vertical direction the sample cell is mounted on a 3D positioning piezo stage (P-517.3CD, PI, Karlsruhe, Germany). This stage can be moved with sub-nanometer accuracy in all three dimensions. Additionally, its position is recorded using a data acquisition (DAQ) card (USB-6281 M, NI, Austin, TX, USA).

The magnetic tweezers instrument was placed on an active damping table (TS300LT, Table Stable Ltd., Zwillikon, Switzerland). The entire instrument was located in an isolated room to shield it from thermal changes due to air flow and acoustic noise. The power supplies and controls as well as the computer connected to the instrument were placed outside this room.

The orientation of the polarization of the permanent magnets was changed to maximize the applicable force: While the orientation of their poles was horizontally parallel in the standard configuration, they were placed vertically antiparallel in the new design according to Ref. 36. Due to the vertical alignment of the magnetizations, a reduction of the gap size between the magnets allowed the force on a 1 μm sized magnetic particle to increase by a factor of 2 to approximately 12 pN.

Apart from the GPU-based image analysis, several other improvements were implemented in the tracking algorithm. The recorded images were corrected for fixed-pattern noise (FPN) of the camera prior to analysis. FPN is due to the fact that individual pixels can have different sensitivities and offsets. With this correction, simultaneous tracking of a magnetic bead and a non-magnetic reference microsphere was still possible at 2.5 kHz. Additionally a feedback loop to the piezo stage was implemented to keep the relative distance of the fluidic cell to the optical axis in all three dimensions constant.

The results of the high-resolution test measurements are shown in section 2.2. With this increased spatio-temporal resolution it was then possible to measure intramolecular friction which occurs during refolding of nucleic acids (see chapter 5).

[†]Improvements to the software were implemented by Alexander Huhle.

2.2. Resolving length changes of DNA with Ångström accuracy

2.2.1. Resolution limits of the instrument

In the experiments shown the magnetic microsphere, which serves as a probe for the determination of the DNA length and the applied force, moves due to collisions with the molecules of the liquid environment. The quality of the information about the DNA therefore depends on the accuracy with which the position of the microsphere can be determined. To maximize this precision two requirements should be fulfilled. Firstly, the sample chamber should be isolated from the surroundings, i.e. the effect of external sources of disturbance such as thermal, mechanical, and electronic noise, should be minimized. Secondly, the actual measurement should be performed with highest possible precision.

To guarantee the first condition, the design of the instrument was optimized to greatly reduce undesirable external influences (see section 2.1.2). For this instrument precautions were taken to decouple the sample under study from external noise sources such as mechanical vibrations, intensity changes from the illumination, and the unwanted thermal expansion of the solid instrumental parts due to changes of the room temperature.

To also fulfill the second condition, the contribution of shot noise to the detected signal should be minimized (see section 2.1.2). The photon statistics can be improved by increasing the number of photons used for the analysis of each image. This is realized by maximizing both the temporal resolution as well as the magnification.

Initially the relative contribution of external noise to the detected signal is probed. To achieve this, the time trajectory of the position of a particle which is immobile is recorded (see Fig. 2.2). Completely restricting the motion of a particle in an aqueous solution at room temperature is impossible due to Brownian motion. However, here the motion of a microsphere was greatly limited by firmly attaching it to a glass surface. For the detailed protocol see Appendix A.

To determine the different sources of external noise, it is useful to display the signal not only in the temporal space, but also in the frequency domain using a Fourier transform. This transformation is described thoroughly in Ref. 37. The Fourier transform contains a real and an imaginary part, such that it is more convenient to analyze the square of the absolute value, the power spectrum or power spectral density (PSD). If the noise disturbing a signal is uncorrelated, all frequencies contribute equally to the signal (white noise), corresponding to a plateau in the PSD. The value on the ordinate multiplied by a certain frequency interval gives the corresponding mean-square displacement (MSD) or variance to this frequency interval.

The PSDs shown in Fig. 2.2b clearly demonstrate that the system is affected by external sources of noise. According to the shape of the PSD and the frequencies at which the disturbance occurs it is possible to distinguish three types of external noise (thermal, mechanical, and photon statistics) that couple into the system. The effect of thermal noise which is due to changes in the room temperature, can be seen predominantly in the axial direction as a low frequency drift component. Precautions were taken in the design of the instrument to remove mechanical low frequency noise,

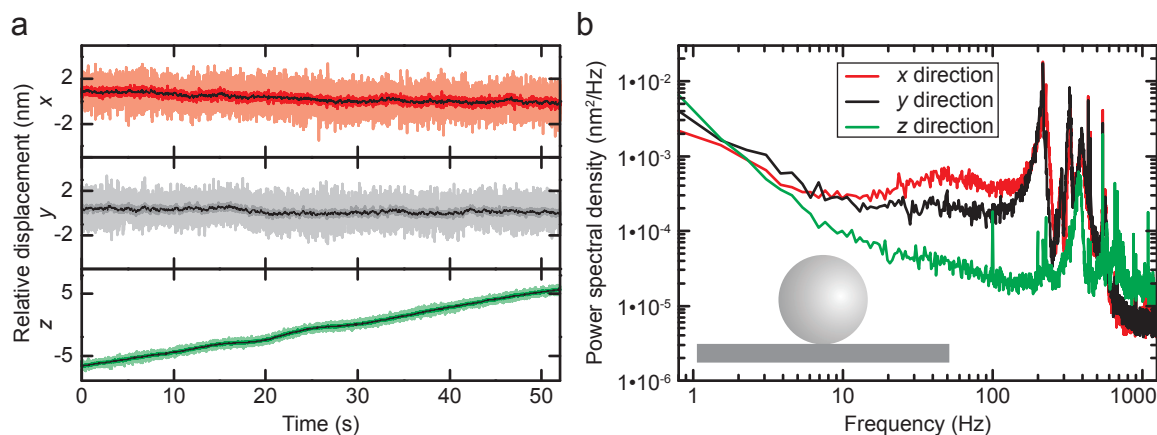


Figure 2.2. Three dimensional tracking of an immobilized microsphere. (a) A $3.2 \mu\text{m}$ sized polystyrene microsphere was immobilized on a glass surface in a solution containing 1 M NaCl. In the lateral dimensions the system is more stable than in the axial direction, where the system drifts approximately 14 nm in one minute. Images were recorded at 2500 Hz and the position of the bead extracted in real time. Shown also is a smooth to 100 and 10 Hz. (b) The power spectral density of the time traces shown in a. The PSD can be used to determine the different sources of external noise (see text). These experiments were performed together with Alexander Huhle.

e.g. oscillations of the building (see section 2.1.2). Therefore this is most likely due to expansion of the individual components.

The broad but well defined peaks present in all directions correspond to the resonance frequencies of the piezo stage. In the lateral directions the stage can move $100 \mu\text{m}$ while in the axial direction its range is only $20 \mu\text{m}$. Therefore it is softer in the lateral directions, such that the peaks of PSD are larger by one order of magnitude in the lateral directions than in the axial direction. The stage is stiffer in the axial direction causing the resonance peaks to be shifted to higher frequencies. The spikes at multiples of 100 Hz in the z -PSD most likely correspond to higher harmonics from the illumination with the mercury arc lamp.

All of these external influences can be greatly reduced by simultaneously tracking a second immobile microsphere, which serves as a reference. Fig. 2.3a shows the time trajectory of the differential position of two microspheres in all three dimensions. For the single microsphere immobilized on a surface shown in Fig. 2.2, the drift of the system caused a change in the axial direction of 14 nm within one minute. This drift is reduced to the sub-Ångström level when subtracting the position of a second immobilized microsphere (see Fig. 2.3). Furthermore the root mean square displacement (RMS) in the lateral directions decreases from 7 \AA for single to 1 \AA for differential bead tracking. The influence of thermal, mechanical, and electronic noise on the measurement signal can be greatly reduced by using a stationary reference particle. Therefore in all the magnetic tweezers measurements shown in this work the position of the magnetic microsphere was determined with respect to such a reference microsphere.

For tracking with respect to an immobilized reference bead, there is still some

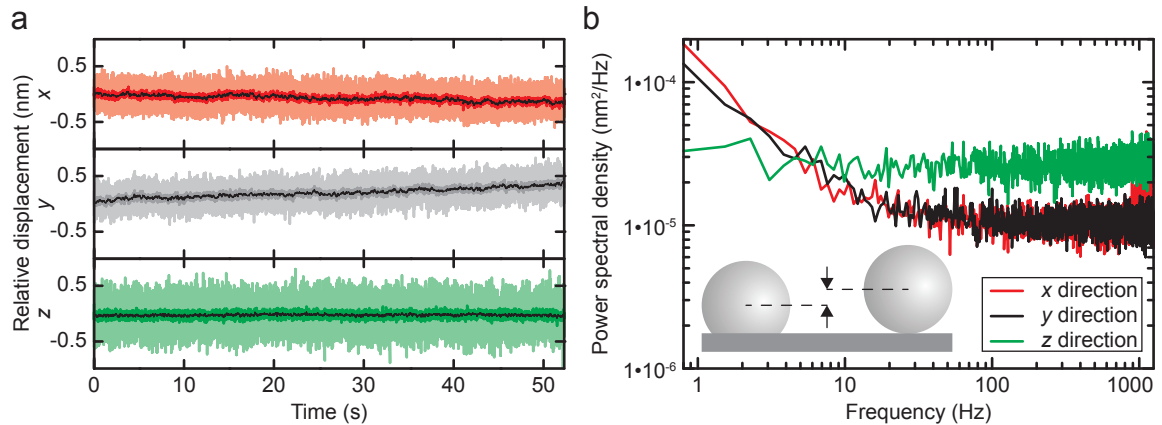


Figure 2.3. 3D differential tracking of two immobilized microspheres. (a) The two $3.2 \mu\text{m}$ sized polystyrene microspheres were immobilized on a glass surface in a solution containing 1 M NaCl and tracked simultaneously. Images were recorded at 2500 Hz and the positions of the beads extracted in real time. Shown also is a smooth to 100 and 10 Hz. (b) The power spectral density of the time traces shown in a. In both lateral directions one can see that there is still some drift in the differential coordinates, which corresponds to an increasing PSD towards smaller frequencies. This is most likely due to an improper attachment of the microspheres to the substrate surface. These experiments were performed together with Alexander Huhle.

low frequency drift contributing to the detected signal in the lateral directions (see Fig. 2.3b). This is most likely due to an improper attachment of the microspheres to the substrate surface. Nevertheless, even for small frequencies differential tracking reduces the overall noise in the axial direction by two orders of magnitude (compare Figs. 2.2b and 2.3b).

In addition testing the stability of the magnetic tweezers instrument, the spatio-temporal resolution was probed. To this end the piezo stage, on which the fluidic cell was mounted, was moved with sub-Ångström accuracy in the axial direction. As the components for the image detection are fixed, a motion of the piezo stage and consequently of the sample with respect to the optical axis is detected as a movement of the microsphere. Such “mimicked” position changes in the axial direction of a $3.2 \mu\text{m}$ sized polystyrene microsphere immobilized on a glass surface are shown in Fig. 2.4.

In this experiment the system could not be directly corrected for drift by means of a reference microsphere immobilized on the surface. Therefore the system drifts several nanometers during the time of the experiment. Nevertheless steps of the piezo stage with a size of only 3 \AA on the second time scale are clearly seen in the detection channel of the microsphere. This is remarkable keeping in mind that the spacing between two consecutive base pairs corresponds to 3.3 \AA for double stranded DNA in B-form.

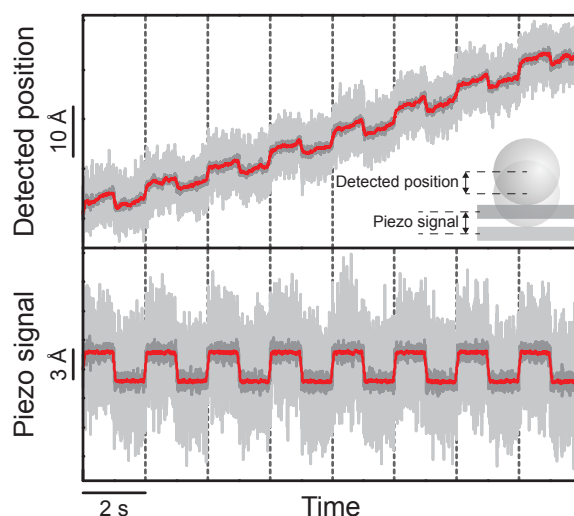


Figure 2.4. Mimicked motion of a fixed microsphere by moving the piezo stage. Moving the piezo stage on which the fluidic cell is mounted allows to mimic the motion of a fixed particle with respect to the optical axis. (*Bottom*) The piezo stage was moved in the vertical direction every second by a distance of 3 \AA up and down, respectively. (*Top*) The axial position of a $3.2 \mu\text{m}$ sized polystyrene microsphere immobilized on a glass surface in a solution containing 1 M NaCl was tracked simultaneously. Although the entire system drifts several nanometers within the time of the measurement, the 3 \AA steps can clearly be resolved. Data were recorded at 2500 Hz (light gray) and smoothed to 100 (dark gray) and 10 Hz (red). These experiments were performed together with Alexander Huhle.

2.2.2. Resolving length changes of DNA

In the previous section the stability and the resolution has been demonstrated which can be achieved when tracking a fixed microsphere. In the actual experimental assay, however, the microspheres which are tracked are not immobilized on the substrate surface, but are tethered to a DNA molecule which is attached to a glass surface. Such a tethered particle is much more subjected to Brownian motion than a stationary particle and therefore displays a larger mean square displacement.

By applying a force to the magnetic microspheres such that the DNA molecule is stretched, one can reduce the mean square displacement of the bead caused by the thermal forces. Therefore, in order to detect small length changes of the DNA which are due to the separation of the double-strand, it is advantageous to apply a relatively high force to the DNA. This force depends on the size and the magnetization of the microspheres, the strength of the permanent magnets, and the magnet configuration. Fig. 2.5 shows the resulting traces of a $1 \mu\text{m}$ sized magnetic microsphere tethered to a DNA molecule subjected to a force of 12 pN .

The mean square displacement of the microsphere depends also on the length of the tether. A shorter DNA molecule displays a smaller mean square displacement. Here a double stranded DNA molecule was used with an approximate length of 1.9 kbp . This is the typical length of the molecules used in chapters 3 and 4.

The fluctuations in the axial direction are much lower than in the lateral directions.

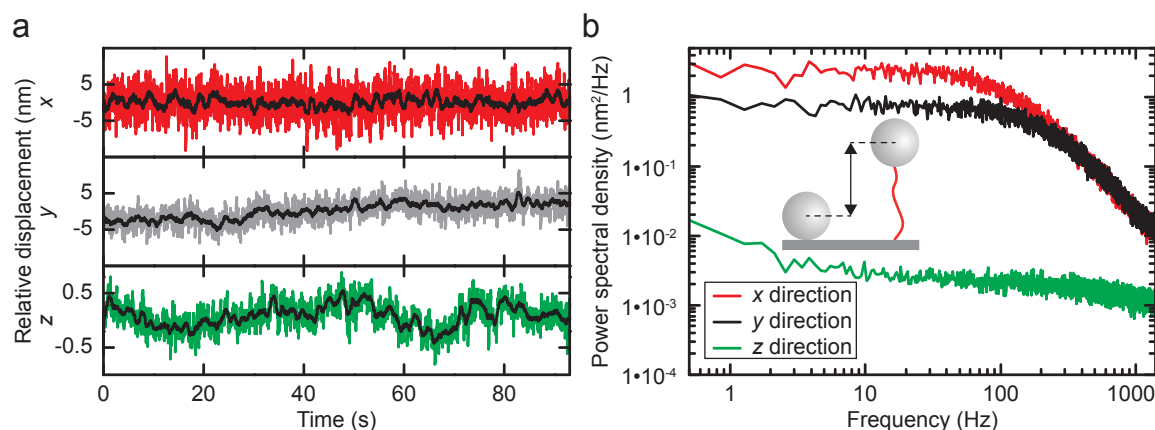


Figure 2.5. 3D tracking of a magnetic microsphere tethered to a DNA molecule.

(a) The $1\ \mu\text{m}$ sized magnetic bead was tethered to an approximately 1.9 kbp long DNA molecule and its position measured at a force of 12 pN in a solution containing 300 mM NaCl in 10 mM phosphate buffer at pH 7.4. The magnetic microsphere was tracked with respect to a reference bead which was immobilized on the substrate surface. Images were recorded at 2800 Hz, however, for illustrative purposes only a smooth to 100 and 10 Hz is shown. (b) The power spectral density of the time traces shown in a follow the shape of a Lorentzian characteristic for a tethered particle undergoing Brownian motion. In the axial direction a component of low frequency drift couples into the measured signal. For more details see the text. The root mean square displacements are 19, 15, and 1.5 nm in the x , y , and z direction, respectively.

This is due to the external force which is oriented in the direction of the gradient of the applied magnetic field. In the magnet configuration used here (see section 2.1), this gradient is directed in the z direction reducing the fluctuations of the microsphere in the axial direction.

The overall shape of the power spectral density shown in Fig. 2.5b varies from the PSD of an immobilized particle (see Fig. 2.3b). While smaller frequencies contribute equally to the PSD, with increasing frequency the relative contribution to the PSD decreases based on the spatial limitation caused by the tether. This is the characteristic shape of the PSD for a tethered particle undergoing Brownian motion and is called Lorentzian. The physical problem of a tethered particle which is overdamped and moves in a viscous medium can be solved analytically. The solution can then be used to fit the PSD and to calculate the mean square displacement and consequently the force. This is shown in section 2.3.

The mean-square displacement in the x direction is larger than in the y direction (Fig. 2.5). This is due to the preferential orientation of the magnetic moment of the microsphere along the field lines of the permanent magnets, which is defined here as the y direction. The consequences of this pinning effect for the motion of the magnetic bead is discussed in more detail in Ref. 33.

Although the position of the tethered microsphere was determined with respect to a non-magnetic microsphere immobilized on the substrate surface, some low frequency oscillations still couple into the detected signal. This is seen in all three dimensions,

however, the relative contribution is most obvious in the axial direction (Fig. 2.5). A direct correlation of these low frequency oscillations between the spatial dimensions was not found. Comparing the contribution of the low frequency noise between the lateral directions one finds that the oscillations are more pronounced in the direction of the magnetic field (y) than perpendicular to it (x). This has been confirmed by turning the magnetic field by 90° (data not shown).

To find the source of these low frequency oscillations a large set of experiments has been performed (data not shown). However, the origin of this phenomenon has yet to be determined. For completeness an outline of the experiments realized so far is given in the following.

One aspect of the assay which was tested was the attachment of the DNA both to the substrate surface and the magnetic microsphere. If the origin of the low frequency oscillations were based on an instability of the attachment of the DNA to the substrate surface, oscillations should be detected only in the axial direction. As the oscillations are also detected in the lateral directions, this explanation can be discarded.

To determine if the low frequency oscillations are due to an instability at the attachment on the other end of the DNA, i.e. to the magnetic microsphere, experiments with a DNA construct containing a single biotin-streptavidin bond between the nucleic acid and the bead have been performed. These experiments, however, displayed a similar amount of low frequency noise.

In addition a different type of magnetic microsphere (MagSense, MagSense Life Sciences, W. Lafayette, IN, USA) was tested yielding similar results. To exclude that the ends of the DNA unspecifically stick to the magnetic microsphere, both commercially and self-made BSA-blocked beads were tested with similar outcome.

Currently these results indicate that the low frequency oscillations observed in the tracking of the magnetic microsphere originate from some intrinsic properties of the beads themselves. For instance, the magnetic domains in the microsphere slowly could change their orientation. These changes might be prevented by tempering the magnetic beads prior to the actual experiment. However this hypothesis should be corroborated in further studies.

Theoretical modeling considering DNA length fluctuations allows verification of the measurement (see chapter 5) and shows that apart from the low frequency oscillations the detected signal corresponds exclusively to the Brownian noise of the bead. This is remarkable because the Brownian motion of the bead defines the thermal noise limit of the assay, which cannot be overcome.

Based on this result the actual objective defined in the introduction to this chapter, i.e. the determination of the spatio-temporal resolution which can be achieved with the tethered particle assay, could be pursued. To this end the resolution of the tethered particle assay is probed similarly to the experiment shown in Fig. 2.4: The piezo stage, on which the sample cell is mounted, was moved along the optical axis, while a constant force was applied to the magnetic bead. The motion of the stage is detected in the channel recording the motion of the magnetic bead as if the microsphere would move up and down (Fig. 2.6).

Due to the nature of this experiment, the system could not be corrected for drift directly by means of the reference microsphere immobilized on the surface. The overall

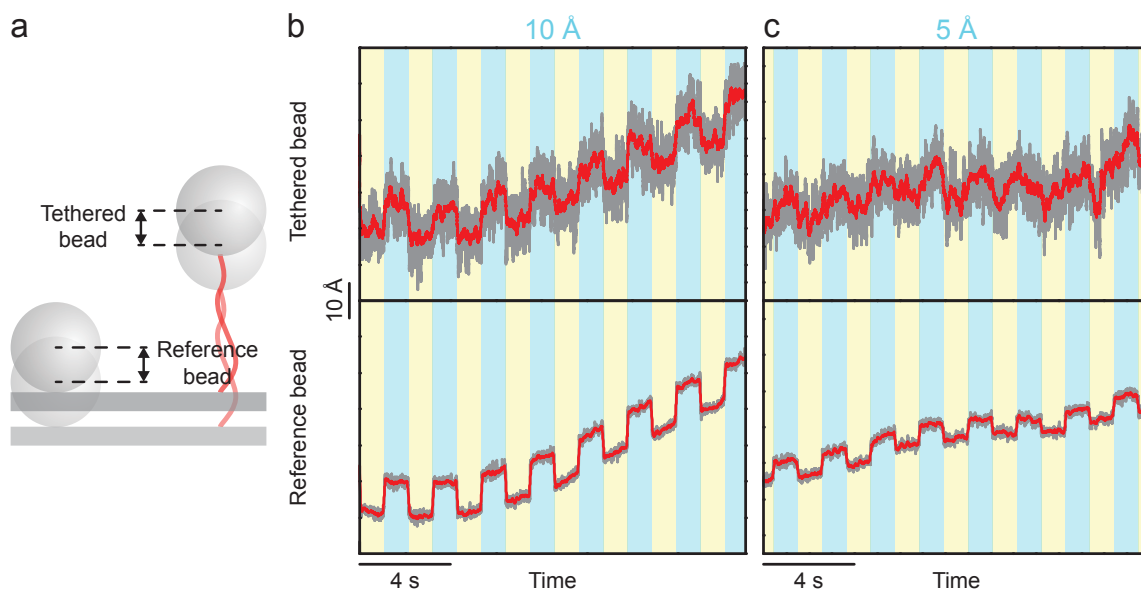


Figure 2.6. Mimicked motion of a microsphere tethered to a DNA molecule. (a) Discrete length changes of a $1\ \mu\text{m}$ sized magnetic microsphere tethered to a DNA molecule (*top*) and a $3.2\ \mu\text{m}$ sized polystyrene microsphere immobilized on a glass surface (*bottom*) are mimicked simultaneously by means of the piezo stage. The stage was moved a distance of (b) 10 and (c) 5 Å in 1.1 second intervals. Images were recorded at 3000 Hz, however, for illustrative purposes only a smooth to 100 (gray) and 10 Hz (red) is shown. The temporal evolution of the positions of both microspheres shows the influence of drift. Nevertheless even the 5 Å steps can be resolved. The DNA had a length of 1.9 kbp carrying multiple biotin and digoxigenin modifications at the ends. Experiments were performed in 300 mM NaCl in 10 mM phosphate buffer (pH 7.4) at a stretching force of 12 pN.

drift of the system can be corrected for by subtracting a temporal average over the position of the reference microsphere from the measured location of the magnetic bead. However, in the actual experiments, i.e. when the length changes of the DNA are not mimicked by the piezo stage but actually occur, the position can be determined with respect to a reference particle, which should further improve the resolution (see section 2.2.1).

The stage was moved with steps of discrete size in approximately one second intervals. 5 Å steps can still be resolved (see Fig. 2.6c). This resolution is the highest that has been reported yet for DNA length measurements with magnetic tweezers. In a review which was published this year, Bryant et al. stated that the current resolution limits of magnetic tweezers corresponded to the unwinding of 3 bp (corresponding to a DNA length change of 3.4 nm) at a time resolution of approximately one second [8]. With the improvements that were made to the magnetic tweezers instrument it was shown that at the same temporal resolution even 1 bp steps (corresponding to a DNA length change of 1.1 nm) should be resolved unambiguously. As an exemplary system hairpin unwinding experiments as shown in Ref. 33 could be performed.

2.3. Using Brownian motion to measure force

2.3.1. Force dependence of the fluctuations

As mentioned in section 2.2.2, the magnetic microsphere which is tethered to the DNA is constantly fluctuating due to collisions with the surrounding molecules. However, when an external force F_{mag} is applied to the bead, the DNA is stretched and the fluctuations occur around an equilibrium position. To quantify this force the physical system consisting of the DNA tethered to the magnetic microsphere can be approximated as an inverted pendulum (Fig. 2.7). The pendulum length corresponds to the DNA's extension L . Once the pendulum is moved out of its equilibrium position by an angle α , the magnetic force causes a restoring force F_b which drives the pendulum back to its equilibrium position:

$$F_b = F_{\text{mag}} \cdot \sin \alpha = F_{\text{mag}} \cdot \frac{\Delta y}{L} = k_y \cdot \Delta y$$

$$\text{where } k_y = \frac{F_{\text{mag}}}{L} \quad (2.1)$$

is the trap stiffness. Note that F_b is actually oriented along the tangent line to the arc on which the pendulum moves. However, for magnetic tweezers measurements, the extension of the typically used DNA constructs is much larger than their fluctuations. Therefore the vertical extension change due to the fluctuations is neglected.

Furthermore, in the y direction the bead is pinned (see above), such that it will rotate around its attachment point to the DNA as it moves away from the equilibrium

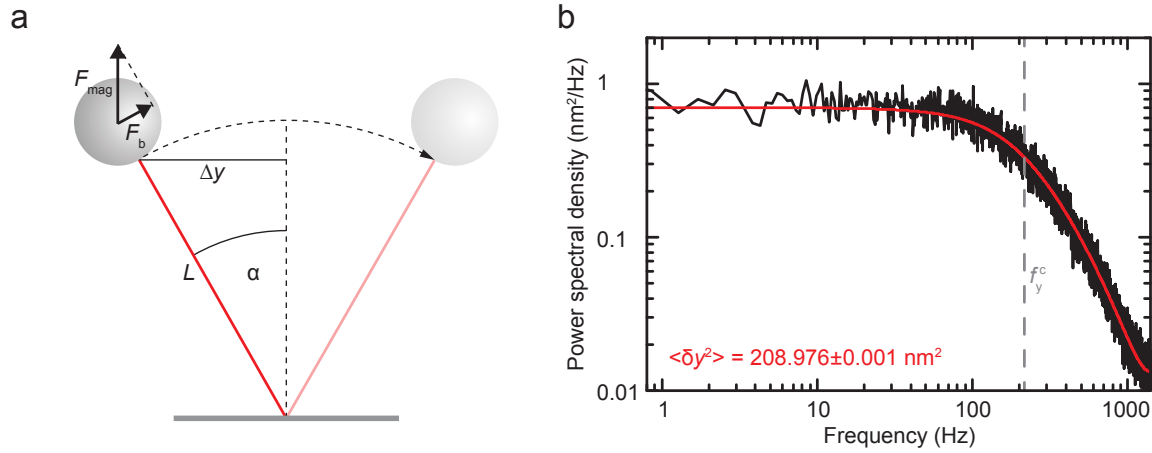


Figure 2.7. Force calculation from the microsphere fluctuations. (a) The physical system of the DNA (red line) tethered to a microsphere (gray sphere) can be modeled by an inverted pendulum of length L . The stretching force F_{mag} produces a back driving force F_b as soon as the bead is moved out of its equilibrium position. Note that in the y direction the bead cannot rotate around its axis. (b) The power spectral density of the fluctuations of the magnetic microsphere in the y direction (shown in Fig. 2.5) can be fit with a Lorentzian curve (Eq. 2.11). This fit defines the cutoff frequency f_{yc} and allows to calculate the mean square displacement $\langle \delta y^2 \rangle$. The MSD in return can be used to calculate the force acting on the particle via Eq. 2.3.

position. This effect can be neglected as long as the deflections from the equilibrium position are small compared to the length of the DNA.

The motion of the pendulum can be described by a harmonic potential. The mean energy of such a one dimensional oscillator E_{osc} is related to the thermal energy via the equipartition theorem [20]. This principle dictates that the energy stored in each degree of freedom of a system corresponds to half its thermal energy:

$$E_{\text{osc}} = \frac{1}{2}k_y \langle \delta y^2 \rangle = \frac{1}{2}k_B T. \quad (2.2)$$

where k_B is the Boltzmann constant, T the absolute temperature, and $\langle \delta y^2 \rangle$ the mean square displacement (MSD). According to this relation it is possible to determine the trap stiffness solely from the measurement of the positional variance. Inserting Eq. 2.1 into Eq. 2.2 yields the magnetic force that acts on the bead

$$F_{\text{mag}} = \frac{k_B T \cdot L}{\langle \delta y^2 \rangle}. \quad (2.3)$$

The stretching force can be calculated from the fluctuations in both lateral directions independently. In the magnetic tweezers instrument used here the y direction is defined by the imaginary line connecting the mid-points of the permanent magnets. Therefore, in the y direction the bead is pinned, i.e. it cannot rotate around the axis crossing its midpoint in the x direction. Hence the pendulum length corresponds exactly to the extension of the DNA. In the x direction the forces can be calculated analogously, however, as the bead is free to rotate around the axis crossing its midpoint in the y direction, the radius of the bead has to be added to the mean DNA length.

2.3.2. Determination of the mean square displacement

Although it is possible to find the mean square displacement directly from the fluctuations of the lateral coordinates of the magnetic microsphere, here the MSD is determined following a Fourier transformation into the frequency space. One major advantage is that corrections due to instrumental limitations, such as the finite acquisition frequency of the camera, can be performed with some elementary mathematical operations in the frequency domain.

The equation of motion of an oscillator in a fluid undergoing Brownian motion can be described by the Langevin equation [38]:

$$m\ddot{y}(t) + \gamma\dot{y}(t) + k_y y(t) = f_{\text{therm}}(t). \quad (2.4)$$

In this differential equation, the first summand refers to the inertial force acting on the particle of mass m . The second term corresponds to the frictional force with drag coefficient γ . The third summand accounts for the fact that the particle is tethered to a surface and that there is a restoring force caused by the interaction of the particle with the field from the permanent magnets (see section 2.3.1). f_{therm} refers to the thermal force the particle experiences in the viscous solution due to collisions with surrounding solvent molecules.

These collisions are stochastic processes, such that the corresponding force has a Gaussian probability distribution with the following auto-correlation function $R_{f_{\text{therm}}}$ as a function of time τ [39]:

$$R_{f_{\text{therm}}}(\tau) = \langle f_{\text{therm}}(t) f_{\text{therm}}(t - \tau) \rangle = 2k_{\text{B}}T\gamma \cdot \delta(\tau) \quad (2.5)$$

where δ is the Dirac delta function

$$\delta(\tau) = \delta(-\tau) \quad \text{and} \quad \int_{-\infty}^{\infty} \delta(\tau) d\tau = 1. \quad (2.6)$$

Eq. 2.5 guarantees that the thermal forces are uncorrelated in time. The actual random force has a finite correlation time corresponding to the collision time of the molecules, such that the delta function is an approximation. However, the Langevin equation describes the motion of a macroscopic particle which occurs on a much larger time scale than the collisions with the solvent molecules.

The Fourier transformation of Eq. 2.4 gives:

$$Y(f) = \frac{F_{\text{therm}}(f)}{-m(2\pi f)^2 - i\gamma(2\pi f) + k_y} \quad (2.7)$$

where $Y(f)$ and $F_{\text{therm}}(f)$ are the Fourier transforms of $y(t)$ and $f_{\text{therm}}(t)$, respectively, which are functions of the frequency f . The power spectral density of the thermal force is the Fourier transform of the autocorrelation function (Eq. 2.5):

$$|F_{\text{therm}}(f)|^2 = 2 \int_{-\infty}^{\infty} R_{f_{\text{therm}}}(\tau) e^{-2\pi i f \tau} d\tau. \quad (2.8)$$

The factor of two in this equation is due to the fact that in the measurement of the position of the bead only positive frequencies are detected. Consequently the one-sided power spectrum has to be considered twice. Furthermore, the autocorrelation function is symmetrical [39], such that Eq. 2.8 can be simplified:

$$|F_{\text{therm}}(f)|^2 = 2 \int_{-\infty}^{\infty} R_{f_{\text{therm}}}(\tau) \cos(2\pi f \tau) d\tau = 4k_{\text{B}}T\gamma. \quad (2.9)$$

This demonstrates that the thermal force is independent of the frequency. Furthermore this equation has an important implication known as the Fluctuation-Dissipation theorem [40]: The amplitude of the force depends only on the drag coefficient and not on the stiffness or the mass.

To better understand the system it is useful to compare the contribution of the inertial force with the one from the drag force: In general, if $\gamma^2 < 4mk_y$, the system is underdamped [39]. On the contrary, overdamping occurs when $\gamma^2 > 4mk_y$. In case of a spherical particle of radius R_s moving in a medium with viscosity η the drag coefficient can be calculated according to Stokes's law:

$$\gamma = 6\pi\eta R_s. \quad (2.10)$$

In a typical magnetic tweezers experiment, $\eta = 10^{-3} \text{ kg}/(\text{s} \cdot \text{m})$ and $R_s = 10^{-6} \text{ m}$, yielding $\gamma = 10^{-8} \text{ N} \cdot \text{s}/\text{m}$. A standard value for the mass of a magnetic microsphere is $m = 10^{-15} \text{ kg}$ and for the trap stiffness $k_y = 10^{-9} \text{ N}/\text{m}$. Therefore the system is highly overdamped.

The time constants of a highly overdamped system correspond to $\tau^{\text{inert}} = m/\gamma$ for the inertial force and $\tau_y^c = \gamma/k_y$ for the drag force [39]. In a typical magnetic tweezers experiment, τ^{inert} is on the order of nanoseconds, while τ_y^c is on the order of seconds. The highest sampling frequency for the experiments shown in this work was 2.8 kHz and therefore much too small to detect inertial influences on the microsphere. Hence the inertial contributions to the equation of motion (Eqs. 2.4 and 2.7) can be neglected.

The PSD of the Fourier transform of the equation of motion $Y(f)$ is given by:

$$|Y(f)|^2 = \frac{4k_B T \gamma}{k_y^2} \frac{1}{1 + \left(\frac{f}{f_y^c}\right)^2}, \quad (2.11)$$

with the characteristic cutoff frequency

$$f_y^c = \frac{1}{2\pi\tau_y^c} = \frac{k_y}{2\pi\gamma}. \quad (2.12)$$

This PSD corresponding to the motion of a tethered particle is the so called Lorentzian curve and can be seen as a fit in Fig. 2.7b. In the regime above the cutoff frequency, Brownian motion dominates the movement of the bead with $1/f^2$ -noise. This resembles the situation of a “free” particle diffusing in a fluid. For frequencies smaller than the cutoff frequency the motion of the bead is governed by damping.

The relation between the mean square displacement and the power spectral density is described in Parseval’s theorem [41]:

$$\langle \delta y^2 \rangle = \int_{-\infty}^{\infty} |y(t)|^2 dt = \int_0^{\infty} |Y(f)|^2 df. \quad (2.13)$$

One should note that the integration limits change when integrating over the Fourier transform because in this derivation the Fourier transform has been defined for the one-sided power spectrum (see above). Inserting Eq. 2.11 into Eq. 2.13 yields:

$$\langle \delta y^2 \rangle = \frac{4k_B T \gamma}{k_y^2} \int_0^{\infty} \frac{1}{1 + \left(\frac{f}{f_y^c}\right)^2} df. \quad (2.14)$$

Using Eq. 2.12 the prefactor to the integral can be simplified further:

$$\langle \delta y^2 \rangle = \frac{2k_B T}{\pi k_y f_y^c} \int_0^{\infty} \frac{1}{1 + \left(\frac{f}{f_y^c}\right)^2} df. \quad (2.15)$$

The integral can be solved analytically yielding:

$$\langle \delta y^2 \rangle = \frac{2k_B T}{\pi k_y f_y^c} \left[f_y^c \arctan \left(\frac{f}{f_y^c} \right) \right]_0^{\infty} = \frac{k_B T}{k_y}. \quad (2.16)$$

This equality is the same as the one based on the equipartition theorem (Eq. 2.2) for the energy of a one dimensional oscillator. Therefore a fit of the power spectral density allows to calculate the mean square displacement, which can in return be used to calculate the force acting on the DNA.

However, one should note that the data of the fluctuations are obtained from the images that were recorded with a camera. This camera has, of course, a finite exposure time and acquisition frequency and therefore acts as a filter. Two major effects have to be accounted for: Firstly, the recorded intensity of each frame corresponds to an average during the exposure time (windowing effect). Therefore the amplitude of the signal is reduced. Nevertheless, the exposure time is known and therefore can be compensated for [33].

Secondly the Nyquist–Shannon sampling theorem postulates that in order to exactly reconstruct a signal, the sampling frequency has to be at least twice the largest frequency contained in the signal. The bandwidth of the signal produced by the fluctuations of the magnetic bead is unlimited, such that aliasing is inevitable. However, the acquisition frequency though finite is known, which allows incorporation of a corresponding correction in the theory [33].

3. The DNA buckling transition

3.1. DNA supercoiling under tension

As described in chapter 1, DNA supercoiling in living organisms is a direct consequence of the DNA helical structure. It arises during essential cellular processes, such as replication and transcription, when the corresponding cellular factors follow the helical path of the molecule [42, 43]. Supercoiling needs therefore to be counterbalanced [44], but fulfills also important tasks in genome compaction and transcriptional regulation [45].

The magnetic tweezers instrument described in the previous chapter can not only be used to apply force to a DNA molecule, but also to induce torque in the nucleic acid. This allows overtwisting of the DNA while monitoring simultaneously its mechanical response. In the experiment shown in Fig. 3.1, a single DNA molecule was twisted under constant tension. At first the DNA length stays approximately constant as nearly all induced supercoils are stored in the form of twist (Fig. 3.1b and c). Once a critical torque level is reached, the molecule undergoes a transition: it buckles and enters the plectonemic phase (from the Greek *plect*, meaning “braid”, and *neme*, meaning “string” [46]) in which part of the DNA forms a superhelical structure. Additionally added turns are seen in a linear decrease of the DNA length. The formed superhelix buffers any subsequently applied twist as writhe [47]. While torque increases linearly with the number of added turns before buckling, it remains constant in the plectonemic phase.

The transition between linear and plectonemic phase was for a long time thought to occur gradually, based on the shape of the supercoiling curves, i.e. plots of DNA length versus added turns [48]. Recently, however, a discrete and abrupt buckling, seen as a sudden, major DNA length change, has been reported [49]. While most previous measurements had been carried out using magnetic tweezers, this new study employed optical tweezers, which due to continuous rotation allowed a higher resolution of the supercoiling curves. Though the force dependence of the abrupt buckling transition has been characterized, its exact origin remained unclear and it has been speculated that it reflects the formation of the initial plectonemic loop [49].

Here the dependence of the abrupt buckling on the concentration of monovalent ions and on the length of the DNA molecule was investigated using magnetic tweezers. While the presence of an abrupt buckling at increased concentrations of monovalent ions was confirmed, it was found to become less pronounced and finally to disappear at low (20 mM) concentrations of monovalent ions. Also a strong dependence of the abrupt buckling on the DNA length was observed. Quantitative analysis of the postbuckling state occupancy during supercoiling shows that the structure formed during buckling is not fixed, but rather variable. It can buffer considerably more than one supercoil in the form of writhe depending on the applied force, the DNA length

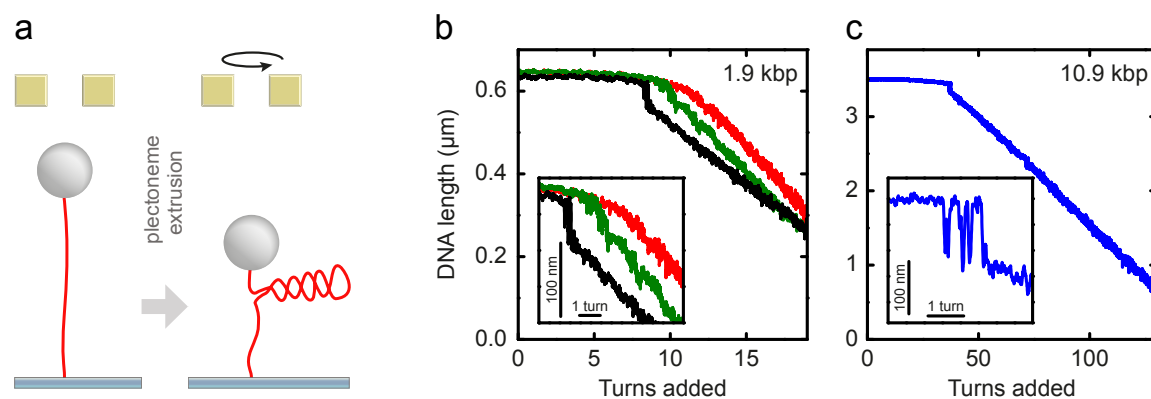


Figure 3.1. Buckling transition at different ionic strengths and DNA lengths. (a) The cartoons illustrate the experimental configuration and the transition from linear to superhelical DNA (red line). The magnetic bead (gray sphere) and the pair of magnets (yellow squares) are also shown. (b) An ~ 1.9 kbp DNA molecule held at a constant force of 3.0 pN is continuously twisted with a frequency of 0.5 Hz and its length is recorded simultaneously. Curves are shown for Na^+ concentrations of 20 mM, 60 mM and 320 mM (red, green and black line). Inset: Enlarged view on the supercoiling curves of the main figure at the buckling transition. (c) Supercoiling curve for a 10.9 kbp DNA molecule twisted with 1 Hz at 3.0 pN force in buffer containing 320 mM Na^+ . Inset: Enlarged view on the supercoiling curves of the main figure at the buckling transition. Data were taken at 300 Hz and smoothed to 20 Hz. All measurements were performed at room temperature in 10 mM phosphate buffer at pH 7.5, supplemented with varying amounts of NaCl to achieve the final Na^+ concentrations.

and the ionic strength of the solution. As the buckling transition itself is spread over a certain finite range of applied turns, the buckling structure was found to vary throughout the width of the transition, i.e. more writhe can be accommodated at higher numbers of turns.

This behavior can be well understood within a model in which a higher energy per writhe is required to extrude the end loop compared to form subsequent turns of the superhelix. Using estimates for the relevant energies the dependence of relevant buckling parameters, e.g. the buckling equilibrium point and the associated torque change, on the different conditions can be reproduced almost quantitatively. Additionally a kinked DNA substrate was investigated, for which “prebuckling” was observed, i.e. an abrupt buckling before the actual superhelix formation. This behavior provides independent evidence of the end loop model.

These results provide insight into the energetics of end loop formation and reveal, as a consequence, the presence of single and multiplectonemic states of supercoiled DNA. Furthermore, they suggest that the plectoneme position on kinked DNA substrates can be pinned to a fixed position.

3.2. Understanding the buckling transition

3.2.1. Abrupt buckling measured with magnetic tweezers

Abrupt buckling upon DNA supercoiling has only recently been discovered using optical tweezers [49]. This technique, however, requires an active feedback in order to keep the force constant upon changes of the DNA length. To exclude artifacts of the particular measurement technique, magnetic tweezers were employed here to detect abrupt buckling at the onset of supercoiling. In contrast to optical tweezers, magnetic tweezers can be considered as a constant force device over the length range of interest. For the supercoiling experiments a short DNA molecule of ~ 1.9 kbp length was used, similarly as employed previously [49]. In contrast to the “standard” magnetic tweezers measurements, in which the DNA length is measured at discrete supercoiling steps of full turns, DNA was supercoiled in a continuous fashion providing a similarly high rotational resolution as the optical tweezers experiments [49].

At low amounts of monovalent ions (20 mM Na^+) an abrupt buckling was not observed but rather a smooth transition from the linear to the plectonemic phase (Fig. 3.1b, red line). This is more in line with the traditional picture of DNA supercoiling [48]. However, when increasing the ionic strength (to 60 and 320 mM Na^+), a sudden jump, i.e. an abrupt buckling, can be observed prior to plectoneme formation (Fig. 3.1b, green and black lines). Notably, with increasing salt the abrupt buckling becomes more pronounced and occurs at fewer added turns, while the length change per turn (i.e. the slope) of the supercoiling curve after the transition is reduced (see chapter 4).

Also the abrupt buckling for a long DNA molecule of 10.9 kbp at 320 mM Na^+ was tested, and found it to be even more pronounced (Fig. 3.1c). The jump size increased notably in length. In addition, the buckling transition ranged over several turns, and comprised many fluctuations between the pre- and postbuckling state.

This demonstrates that abrupt buckling is also observed in constant force measurements with magnetic tweezers. In addition to previous observations the abrupt buckling was found to depend strongly on the ionic strength and on the length of the DNA.

3.2.2. The width of the buckling transition

The transition from pre- to the postbuckling state must coincide with an abrupt reduction of the DNA twist and thus the formation of writhe, since only increasing twist drives the transition. The width of the transition should then provide information about the abrupt twist reduction. Therefore the population of pre- and postbuckling state under equilibrium conditions was measured. DNA molecules were held at constant force and time traces were recorded at different discrete numbers of added turns N , distributed over the width of the buckling transition (Figs. 3.2a and b). Near the buckling transition, the DNA molecule rapidly fluctuates between a pre- and postbuckling state for a fixed number of added turns. In the histograms of the time traces this can be seen as two peaks, which are well fit by a Gaussian function. With increasing amount of added turns, the postbuckling state gets more populated and

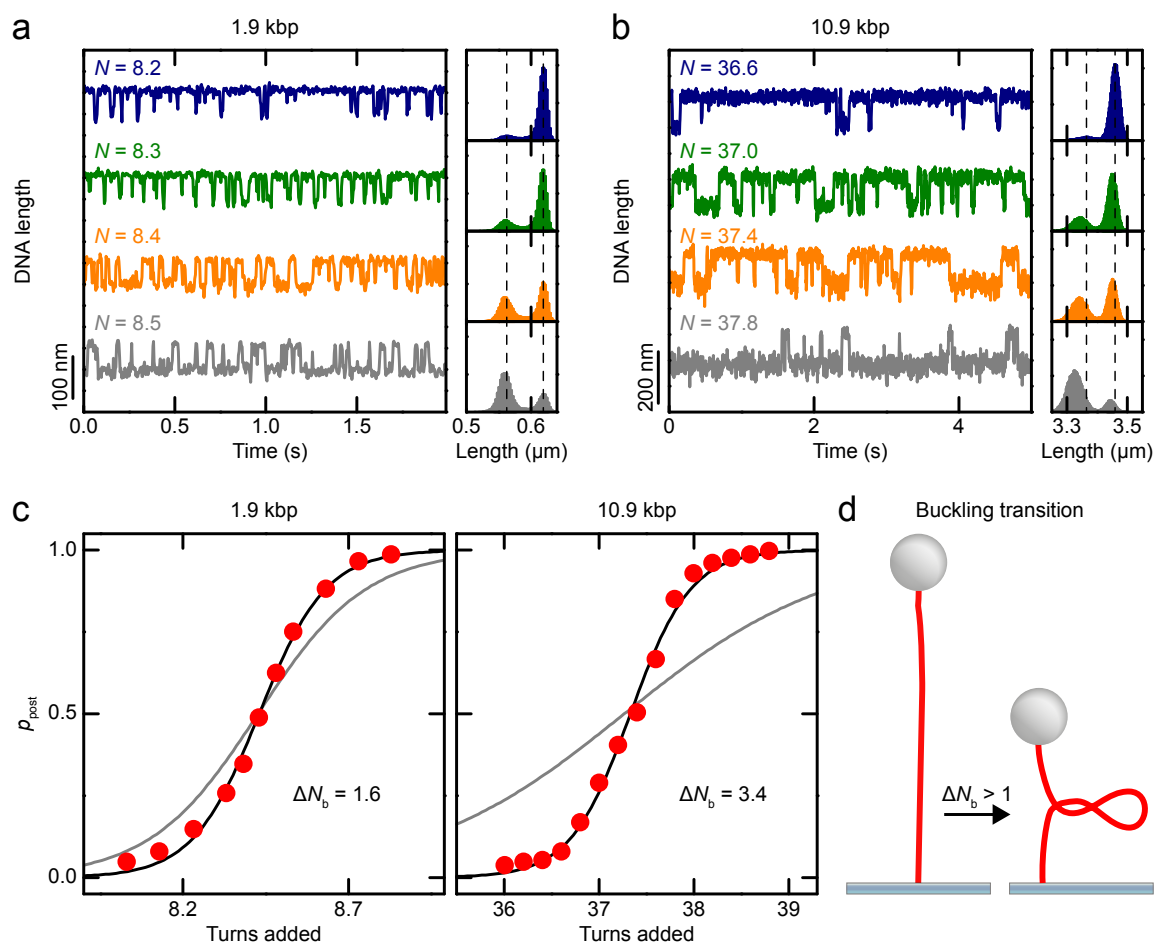


Figure 3.2. Equilibrium occupancy of the pre- and postbuckling state. (a) 1.9 kbp and (b) 10.9 kbp DNA molecules were held at a constant force of 3.0 pN in buffer containing 320 mM Na^+ . Time traces were recorded at different amounts of added turns N in vicinity of the buckling transition. Data were taken at 300 Hz. Normalized length histograms are shown on the right. The DNA was observed to rapidly fluctuate between two distinct states, the pre- and the postbuckling state. Dotted lines are centered on the peaks of the uppermost histogram and indicate the shift of the states throughout the transition. (c) Occupancy of the postbuckling state as function of added turns for both DNA lengths (red dots). Experimental conditions are as in A. Solid lines are fits to the data according to Eq. 3.5, where ΔN_b was taken to be free (black line, N_b of best fit shown in graph) or fixed to $\Delta N_b = 1$ (gray). (d) Illustration representing the behavior of DNA at the buckling transition, which can involve the formation of a structure comprising more than 1 turn of writhe.

the corresponding peak becomes relatively larger. From Gaussian fits to the peaks the probability for the postbuckling state to be populated as function of added turns was determined (Fig. 3.2c).

A simple expression for the postbuckling state population can be derived assuming that for undergoing buckling a fixed free energy penalty E_b has to be paid. For example, E_b must include the displacement of the magnetic bead and increased DNA bending. The buckling is accompanied by a twist reduction due to the formation of

writhe. It occurs when E_b is close to the change in twist energy. Prior to buckling, the free energy of the DNA upon supercoiling is given by [50, 51]:

$$E_{\text{pre}}(N) = \frac{1}{2} \frac{C_s}{L_0} (2\pi)^2 N^2, \quad (3.1)$$

where L_0 is the contour length of the DNA and C_s is the effective DNA torsional modulus with [50]:

$$C_s = C \left[1 - \frac{C}{4p \cdot k_B T} \left(\frac{k_B T}{p \cdot F} \right)^{1/2} \right]. \quad (3.2)$$

C denotes the DNA torsional modulus, p the bending persistence length, and F the applied force. For the torsional modulus and the persistence length values of $100 k_B T \text{ nm}$ [23] and 45 nm were used, respectively. Eq. 3.2 accounts for the fact that due to DNA writhe fluctuations not all added turns contribute to the twist stored in the DNA.

Upon buckling the DNA twist energy is reduced. However, the energetic penalty E_b for the formation of the buckling structure has to be overcome, which provides for the free energy of the postbuckling state:

$$E_{\text{post}}(N, \Delta N_b) = E_b + \frac{1}{2} \frac{C_s}{L_0} (2\pi)^2 (N - \Delta N_b)^2, \quad (3.3)$$

where ΔN_b is the amount of twist, which is transferred into writhe during buckling. Within this simple two state model, the probability that the postbuckling state p_{post} is occupied can be calculated using Boltzmann statistics:

$$p_{\text{post}} = \frac{1}{1 + \exp[(E_{\text{post}} - E_{\text{pre}})/k_B T]}. \quad (3.4)$$

Inserting Eqs. 3.1 and 3.3 into this expression yields

$$p_{\text{post}} = \frac{1}{1 + \exp \left[\frac{C_s}{L_0} (2\pi)^2 (N_b - N) \Delta N_b / k_B T \right]} \quad (3.5)$$

with N_b being the number of added turns at the point of buckling equilibrium, where the pre- and the postbuckling state are equally populated. N_b is then given by:

$$N_b := N \Big|_{E_{\text{pre}}=E_{\text{post}}} = \frac{E_b}{\frac{C_s}{L_0} (2\pi)^2 \Delta N_b} + \frac{1}{2} \Delta N_b. \quad (3.6)$$

Surprisingly, fits of the experimentally obtained postbuckling state occupancy with Eq. 3.5 provide values for ΔN_b which are considerably larger than 1 turn (Fig. 3.2c). At 3.0 pN and 320 mM Na^+ one obtains for the writhe within the buckling structure $\Delta N_b = 1.6 \pm 0.1$ and 3.4 ± 0.2 turns for the short and the long DNA molecule, respectively. Remarkable is also the DNA length dependence of ΔN_b . This suggests that upon abrupt buckling not a fixed structure is formed, such as a first end loop, but rather a continuous structure, such as a plectonemic superhelix with multiple turns (Fig. 3.2d).

3.2.3. Kinetics of the buckling transition

In addition to studying the equilibrium of the pre- and postbuckling states, also the kinetics at the buckling transition were analyzed. To extract the residence times of the individual states, threshold values were applied to assign each time point to the pre- or postbuckling state. From this a binary step function was reconstructed and residence times were calculated.

The residence times appear exponentially distributed for the short molecules (Fig. 3.3a), while a minor second exponential component appears for the long DNA (not shown). The mean residence times τ_b^{pre} and τ_b^{post} change exponentially with added turns (Fig. 3.3b) in agreement with a two state system. The torque in the DNA molecule changes the height of the energy barrier for undergoing the transition. One can describe the torque dependence of τ_b^{pre} and τ_b^{post} by adding the torque multiplied by the angular distance to the barrier as an additional term into an Arrhenius equation, which results into:

$$\tau^* = \tau_b \cdot \exp \left[-\frac{C_s}{L_0} (2\pi)^2 (N - N_b) \Delta N_b^* / k_B T \right], \quad (3.7)$$

where τ_b is the mean residence time at the buckling transition. ΔN_b^* is substituted by ΔN_b^{pre} or $-\Delta N_b^{\text{post}}$ corresponding to the twist difference between the transition state and the prebuckling or postbuckling state, respectively. Fitting Eq. 3.7 to the experimental data, the transition state was found to be approximately half-way between the pre- and the postbuckling state for both molecule lengths (Fig. 3.3b).

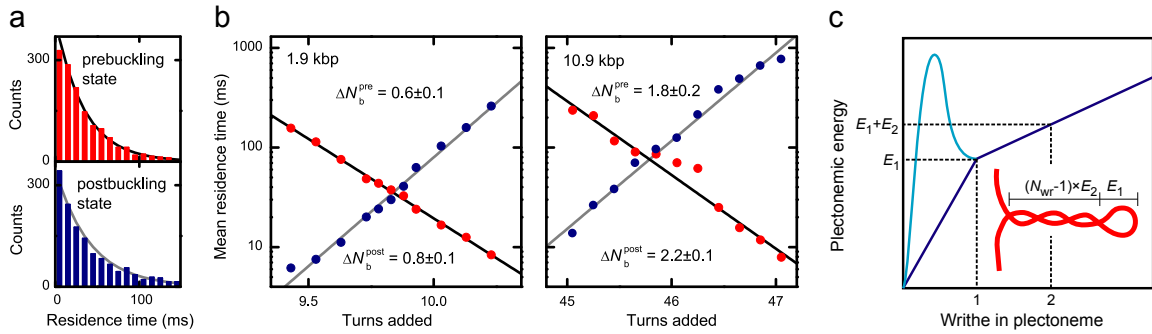


Figure 3.3. Kinetics of the buckling transition. Shown data is for 4.0 pN and 320 mM Na^+ . (a) Distributions of the residence times for the pre- and postbuckling state close to the buckling equilibrium (9.8 turns) for the 1.9 kbp DNA molecule. The solid lines represent a single exponential function with the mean residence time as characteristic decay time. (b) Mean residence times of the prebuckling (red filled circles) and the postbuckling states (blue filled circles) as function of added turns for the 1.9 kbp and 10.9 kbp DNA molecule. Solid lines are exponential fits to the data according to Eq. 3.7. The resulting twist differences to the transition state ΔN_b^{pre} and ΔN_b^{post} are given in the figure. (c) Schematic drawing of the hypothetical energy landscape for plectoneme formation. Independent of the actual landscape for the end loop (dark blue straight line and light blue line with transition state), the supercoiling energy attains E_1 after 1 turn and increases with E_2 for each subsequent turn. Inset: Illustration of the plectoneme formation energies E_1 and E_2 .

Understanding of the energetic barrier needs further work, since there might not be common transition pathways from prebuckling to postbuckling state and vice versa. At 320 mM Na⁺ and 3.0 pN force one obtains $\tau_b = 35.5 \pm 0.5$ and 75.7 ± 0.8 ms for the short and the long molecule, respectively. Thus, τ_b increases with molecular length. This might be due to slower diffusion of the larger plectonemic structure for the long molecule. Furthermore, it was found that τ_b decreases, i.e. transitions become more frequent at lower ionic strength and lower force (data not shown). Generally, the transition between the pre- and the postbuckling state was observed to occur considerably faster than observed previously with optical tweezers [49]. This might be due to different response dynamics for both tweezers systems. Also, the additional potential set by the optical trap leads to different energy landscapes for buckling, which can affect its dynamics.

3.2.4. End loop model for abrupt buckling

The observations made so far, in particular the length dependent writhe of the buckling structure, are consistent with a plectonemic superhelix formed upon abrupt buckling. However, so far the structural and energetic basis underlying the observed behavior remains unclear.

For a plectonemic superhelix an apparent discontinuity can be found at the end loop, which resembles more a planar DNA loop (Fig. 3.3c). For a given DNA segment length it is energetically more favorable to form one turn of the superhelix than a circular loop. Therefore, it is reasonable to assume that the energy for the first turn of the superhelix (end loop) is larger than for any subsequent superhelical turn. This is similar to an approach developed by Daniels et al., which only recently became available [52].

Let E_1 be the free energy for the first turn of writhe in the plectoneme, which comprises the additional energy for the end loop formation. E_2 shall denote the free energy of every subsequent writhe within the plectoneme (Fig. 3.3c). With N_{wr} denoting the writhe of the plectoneme, the free energy of the DNA after buckling for $N_{wr} \geq 1$ is given by:

$$E_{\text{post}}^p(N, N_{wr}) = E_1 + E_2(N_{wr} - 1) + \frac{1}{2} \frac{C_s}{L_0} (2\pi)^2 (N - N_{wr})^2. \quad (3.8)$$

The mean writhe $N_{wr,0}$ for a given number of added turns N is then obtained by minimizing Eq. 3.8 with respect to N_{wr} . Hence, one obtains $N_{wr,0}$ and the corresponding postbuckling energy $E_{\text{post},0}^p$:

$$N_{wr,0} = N - \frac{E_2}{\frac{C_s}{L_0} (2\pi)^2}, \quad (3.9)$$

$$E_{\text{post},0}^p = E_1 + E_2 \left[N - \frac{1}{2} \frac{E_2}{\frac{C_s}{L_0} (2\pi)^2} - 1 \right]. \quad (3.10)$$

Inserting the last equation together with Eq. 3.1 into Eq. 3.4 provides now the probability for the DNA to be in the postbuckling state p_p within the framework of

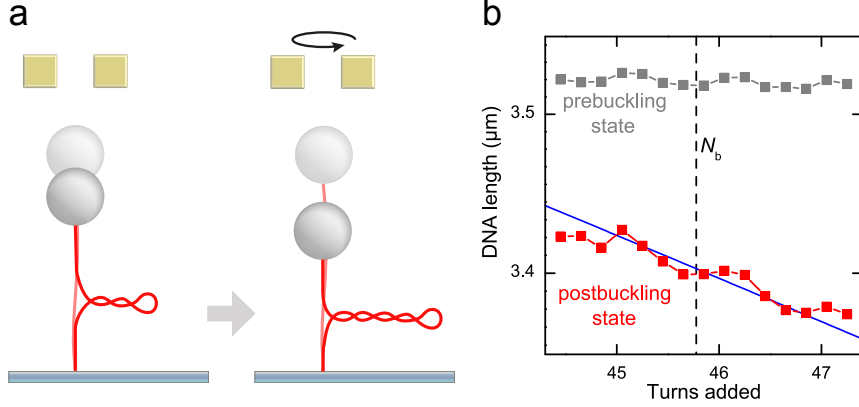


Figure 3.4. Mean position of the pre- and postbuckling state. (a) The extension of a DNA molecule (10.9 kbp) held at constant force (4.0 pN) and ionic strength (320 mM Na⁺) was recorded at different amounts of applied supercoils N in the vicinity of the buckling transition. The writhe of the forming plectoneme is not constant over the buckling transition, but increases linearly with the applied supercoils according to Eq. 3.9. This can indeed be seen in the experimental traces (b) as a gradual shift of the postbuckling level, which corresponds to the postbuckling slope (solid blue line). The buckling point defined where pre- and postbuckling state are equally populated is represented by the dashed black line.

the end loop model:

$$p_p = \frac{1}{1 + \exp \left\{ \frac{C_s}{L_0} (2\pi)^2 (N_b^p - N) \left[\Delta N_b^p + \frac{(N - N_b^p)}{2} \right] / k_B T \right\}}. \quad (3.11)$$

In analogy to the simple model above, N_b^p represents the position of the buckling transition, i.e. when pre- and postbuckling state are equally populated:

$$N_b^p := N \big|_{E_{\text{pre}} = E_{\text{post}}} = \frac{E_2}{\frac{C_s}{L_0} (2\pi)^2} + \Delta N_b^p. \quad (3.12)$$

ΔN_b^p is the average writhe of the abruptly forming plectoneme at the buckling equilibrium point N_b^p , which can be derived by:

$$\Delta N_b^p := N_{\text{wr},0} \big|_{N=N_b^p} = \left[\frac{2(E_1 - E_2)}{\frac{C_s}{L_0} (2\pi)^2} \right]^{1/2}. \quad (3.13)$$

In contrast to the simpler model the writhe of the forming plectoneme is now predicted to increase linearly with the added turns, and not to be a constant over the transition (see Eq. 3.9). This can directly be confirmed by the experiments, since the postbuckling level shifts gradually towards lower DNA length over the transition (see histograms in Fig. 3.2 and Fig. 3.4). One should note that within this derivation N_{wr} is limited not to be smaller than 1, since the actual energy landscape for the end loop formation is unknown (Fig. 3.3c). However, as long as $\Delta N_b^p \geq 1$, the actual

energy landscape for the first turn (e.g. a linear increase with or without an offset, or an additional transition barrier) does not matter, because independent of the actual landscape the same results are obtained (Fig. 3.3c). As it was found that $\Delta N_b^p \geq 1$ for the experimental data, this model is well applicable.

3.2.5. Estimating the plectoneme formation energies

If the plectoneme formation energies E_1 and E_2 are known, one can predict the mean torque Γ and the mean DNA length L as a function of the added turns and applied force using the expressions derived above

$$\Gamma(N, F) = \frac{C_s}{L_0} 2\pi (N - N_{\text{wr},0} \cdot p_p), \quad (3.14)$$

$$L(N, F) = L_0 \cdot z(F, \Gamma) - \left[\Delta L_1 + (N_{\text{wr},0} - 1) \cdot \frac{dL}{dN} \right] \cdot p_p, \quad (3.15)$$

where $z(F, \Gamma)$ is the relative extension of the DNA [50], ΔL_1 the length reduction for the end loop, and dL/dN the slope of the supercoiling curves after the buckling transition.

The extension of DNA stretched at a constant force appears shorter than its contour length due to thermal fluctuations. Additionally, before buckling the extension of DNA gets reduced upon twisting. This is due to writhe fluctuations [53]. The incomplete stretching as function of force F and torque Γ was account for by using the expression for the relative extension derived by Moroz and Nelson, which is given by [50]:

$$z(F, \Gamma) = 1 - \frac{1}{2} \left[\frac{p \cdot F}{k_B T} - \left(\frac{\Gamma}{2k_B T} \right)^2 - \frac{1}{32} \right]^{-1/2}, \quad (3.16)$$

where p denotes the bending persistence length.

To estimate the loop length ΔL_1 as well as the corresponding free energy E_1 to form the end loop, the mechanical energy required to extrude a perfect circular loop of radius R out of a stretched DNA molecule was calculated. The writhe of such a circular loop was assumed to be 1 turn. This is similar to the simple-loop model used previously to derive an estimate for postbuckling torque and slope [48], except that here the DNA shortening is corrected by the relative extension of the DNA [54]. In this case one can write:

$$E_1 = 2\pi R F \cdot z(F, 0) + 2\pi R \frac{1}{2} \frac{k_B T \cdot p}{R^2}. \quad (3.17)$$

The first part of the sum represents the change in potential energy due to shortening of the DNA against the applied force. The second part of the sum represents the bending energy of the DNA within such a loop. Incomplete DNA stretching was accounted for, which essentially lowers the change in potential energy for a given loop length, by introducing $z(F, 0)$ as a correction term. For simplicity, the torque dependence of the DNA extension is neglected, since it represents only a minor correction.

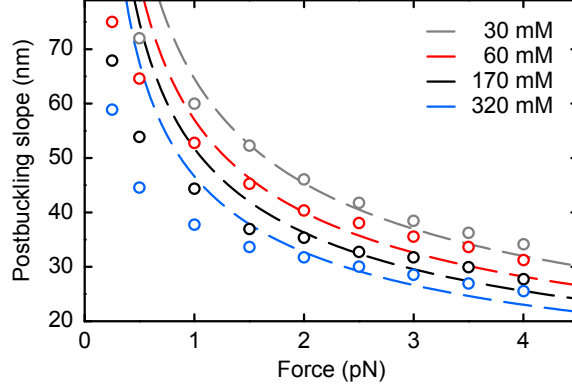


Figure 3.5. Slopes from the supercoiling curves vs. theoretical predictions. The experimentally obtained slopes from the supercoiling curves were compared with theoretical predictions according to the composite model by Marko [51]. Theoretical predictions (dashed lines) were calculated as described [49, 51] for empirically determined values of the plectonemic twist stiffness of 31, 28, 24, and 21 nm, to approximate the measured slopes at 30, 60, 170 and 320 mM Na⁺, respectively. Particularly at elevated ionic strength, the theoretical prediction fails to correctly reproduce the force dependence of the measured slopes correctly [27].

Minimizing the end loop energy with respect to R provides the energetically favored radius of the end loop and correspondingly the length reduction ΔL_1 :

$$\Delta L_1 = 2\pi R_{\min} \cdot z(F, 0) = \left[\frac{k_B T \cdot p \cdot z(F, 0)}{2F} \right]^{1/2}. \quad (3.18)$$

Combining Eqs. 3.17 and 3.18 one obtains for the end loop energy:

$$E_1 = 2\pi [2k_B T \cdot p \cdot F \cdot z(F, 0)]^{1/2}. \quad (3.19)$$

The composite model by Marko also allows calculating the postbuckling slope [51], for which an expression has been derived [49]. Using only non-reduced parameters it results in:

$$\frac{dL}{dN} = \frac{2\pi \left[1 - \frac{1}{2} \left(\frac{k_B T}{p \cdot F} \right)^{1/2} - \frac{C^2 \cdot P \cdot g \cdot \left(\frac{k_B T}{p \cdot F} \right)^{3/2}}{8(C_s \cdot k_B T)^2 \cdot \left(1 - \frac{P}{C_s} \right)} \right]}{\left[\frac{2P \cdot g}{1 - \frac{P}{C_s}} \right]^{1/2} \cdot \left(\frac{1}{P} - \frac{1}{C_s} \right)}, \quad (3.20)$$

with P being the plectonemic twist stiffness, which is a freely adjustable parameter depending on the ionic strength of the solution. Thus P can be obtained by fitting experimental data (Fig. 3.5). One obtains values for P of 31, 28, 24, 21 $k_B T$ nm for 30, 60, 170, 320 mM Na⁺, respectively, in good agreement with previously published data [51, 55]. One should note, however, that the composite model [51] does not provide a satisfactory description of the postbuckling slope over the full range of applied forces [27]. An alternative model with only one fit parameter for the entire range of ionic strengths based on charge reduction of the DNA is discussed in more

detail in chapter 4. The parameter g in Eq. 3.20 corresponds to the negative free energy of stretched, nicked (freely swiveling) DNA given by:

$$g = F - \left(\frac{k_B T \cdot F}{p} \right)^{1/2}. \quad (3.21)$$

To obtain an estimate for the free energy of every subsequent writhe within the plectoneme E_2 , the expression for the postbuckling torque Γ was used, which was also derived within this composite model [51]:

$$E_2 = 2\pi\Gamma = 2\pi \left(\frac{2P \cdot g}{1 - \frac{P}{C_s}} \right)^{1/2}. \quad (3.22)$$

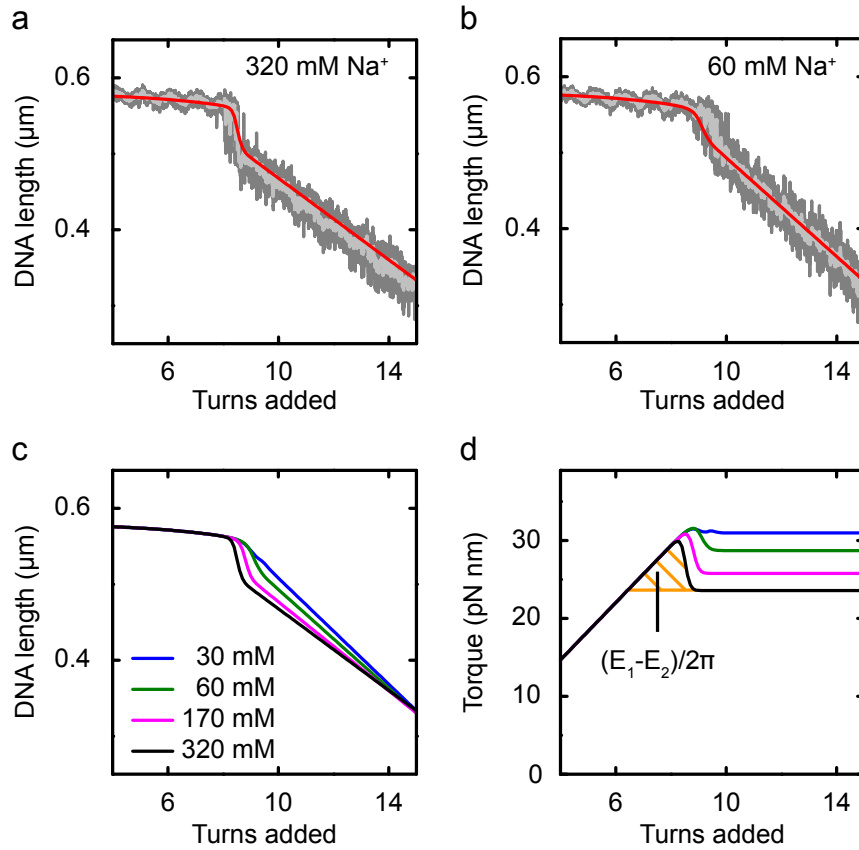


Figure 3.6. Measured supercoiling curves and predictions from the end loop model. (a, b) Supercoiling curves for a 1.9 kbp DNA molecule at 3.0 pN in a buffer containing 320 mM and 60 mM Na⁺ (as indicated). Data were taken at 300 Hz (dark gray) and smoothed to 20 Hz (light gray). The solid red line is the prediction from the end loop model according to Eq. 3.15 using estimates for the plectoneme formation energies E_1 and E_2 (Eqs. 3.19 and 3.22, respectively). (c) Salt dependence of supercoiling curves and (d) torque development as predicted by the end loop model. The shaded area between the torque overshoot and the postbuckling torque under the black curve corresponds to the difference between the end loop energy E_1 and superhelix formation energy E_2 .

Using Eqs. 3.11 to 3.19, the DNA length and the torque upon DNA supercoiling at constant force can now be predicted. Examples of measured and predicted supercoiling curves can be seen in Figs. 3.6a and b. Most importantly this model can well describe abrupt buckling. Despite simple estimates for E_1 and E_2 , one obtains remarkable agreement with the experimental data regarding the buckling point, the width of the transition and the jump length.

Also supercoiling curves and the associated torque at different salt concentrations was calculated (Figs. 3.6c and d). As for the experimental data (Fig. 3.1b) the buckling transition becomes less pronounced at lower salt concentrations. The presence of an abrupt buckling transition is associated with an overshoot of the torque, arising from the sudden writhe formation within the plectoneme (Fig. 3.6d). The energetic difference between the end loop formation energy E_1 and the superhelix-formation energy E_2 corresponds to the area enclosed by the torque overshoot and the postbuckling torque (shaded area in Fig. 3.6d). Thus, the torsional overshoot and correspondingly the abrupt buckling transition are required to ensure the compensatory work for end loop formation. With decreasing ionic strength the electrostatic repulsion between the DNA strands in the plectoneme increases, which is associated with an increase of the postbuckling torque and correspondingly of E_2 (Fig. 3.6d). For the end loop, electrostatics plays supposedly a minor role due to the larger DNA-DNA distance within the loop. It should therefore change much less with the ionic strength. Therefore, the difference between E_1 and E_2 becomes smaller with decreasing ionic strength, which readily explains the disappearance of the abrupt buckling.

3.2.6. Force dependence of the buckling transition

To further support the end loop model for abrupt buckling several parameters obtained from experiment and theoretical prediction were compared. Though only estimates for E_1 and E_2 were used, important trends, such as the scaling with the molecule length, should be correctly predicted.

Experimentally, the jump size upon abrupt buckling L_{jump} at the postbuckling population was obtained by fitting a double Gaussian distribution to the histograms of the DNA length (Figs. 3.2a and b). N_b^p and ΔN_b^p were obtained by fitting the postbuckling state population with Eq. 3.11, which provided similar values as Eq. 3.5 (not shown). At low forces (<1 pN), where the buckling transition became too fast, N_b^p was determined from straight line fits to the supercoiling curves. For high forces, both methods were found to produce consistent results. The plectoneme formation energies E_1 and E_2 were calculated from N_b^p and ΔN_b^p according to the following relations, which were derived from Eqs. 3.12 and 3.13:

$$E_2 = \frac{C_s}{L} (2\pi)^2 (N_b^p - \Delta N_b^p), \quad (3.23)$$

$$E_1 = \frac{1}{2} \frac{C_s}{L} (2\pi)^2 \Delta N_b^{p^2} + E_2. \quad (3.24)$$

First the force dependence of these parameters at 320 mM Na^+ for both the long and the short molecule was evaluated. Within the end loop model the jump size at

the buckling transition can be written as:

$$L_{\text{jump}} = \Delta L_1 + (\Delta N_b^{\text{P}} - 1) \cdot \frac{dL}{dN} + L_0 \cdot \left[z \left(F, 2\pi \frac{C_s}{L_0} N \right) - z \left(F, 2\pi \frac{C_s}{L_0} (N - \Delta N_b^{\text{P}}) \right) \right], \quad (3.25)$$

where the first term of the sum accounts for the length reduction by the end loop, the second term for the other turns of the plectoneme, and the third one for the extension change due to the abrupt reduction of the torque during the transition. L_{jump} was found to increase with DNA length (Fig. 3.7a), which is correctly reflected by the theoretical prediction. For the high force regime, the absolute jump length is also well described. However, at low forces, where the jump size is found to remain constant (short molecule) or to decrease slightly (long molecule) a different trend is predicted. Similar behaviors and jump sizes were also found for the lower salt concentrations (not shown). One should note that Forth et al. reported a large increase of the jump size when decreasing the force and no dependence on the length of the DNA [49]. In the measurements presented here all jump sizes were directly obtained from Gaussian fits to the DNA length distribution at the buckling equilibrium, leaving very little room for ambiguity. Furthermore, the abrupt buckling was especially well resolved for the long DNA molecule. Also, the observed DNA length dependence of the jump size agrees well with the observed length dependence of ΔN_b^{P} , the writhe change during buckling (see Fig. 3.2c and below), since a longer plectoneme should also contain more DNA. One should note that small changes in the expression for E_1 can remarkably change the force dependence of the jump length, while retaining the trend for the other parameters [52]. Beyond simple estimates for E_1 a more elaborate theory is required to substantiate the observed jump lengths.

For ΔN_b^{P} the model presented here predicts a scaling with the square root of the DNA length (Eq. 3.13). Therefore, N_b^{P} does not increase linearly with DNA length but is slightly reduced. To highlight this behavior, the data for the two DNA lengths were scaled linearly in case of N_b^{P} (Fig. 3.7b) and with the square root of the DNA length in case of ΔN_b^{P} (Fig. 3.7c). Within error the prediction can indeed be confirmed. Also the general trend and magnitude for the two parameters with increasing force are well described, though ΔN_b^{P} and the corresponding torque jump upon buckling $\Delta \Gamma_b$ are slightly overestimated.

For E_2 , which is directly related to the postbuckling torque, the data is in agreement with the prediction from Marko et al. [51] (Fig. 3.7d, top). Only a slight variation of the postbuckling torque was observed for both DNA lengths, which reflects the experimental error of the procedure. One should note that the absolute value of E_2 depends directly on the torsional modulus of the DNA, for which a value of $100 k_{\text{B}}T \text{ nm}$ is used. Thus, considering a lower torsional modulus for example $94 k_{\text{B}}T \text{ nm}$ [27] will reduce the obtained values for E_2 and the postbuckling torque.

In addition the energy difference between E_1 and E_2 was obtained, which can be considered as nucleation barrier for plectoneme formation. It amounts to several $k_{\text{B}}T$ at 320 mM Na^+ for the force range considered (Fig. 3.7d, bottom), which should strongly favor the existence of only a single plectoneme (see section 3.3.1 below). Similar to

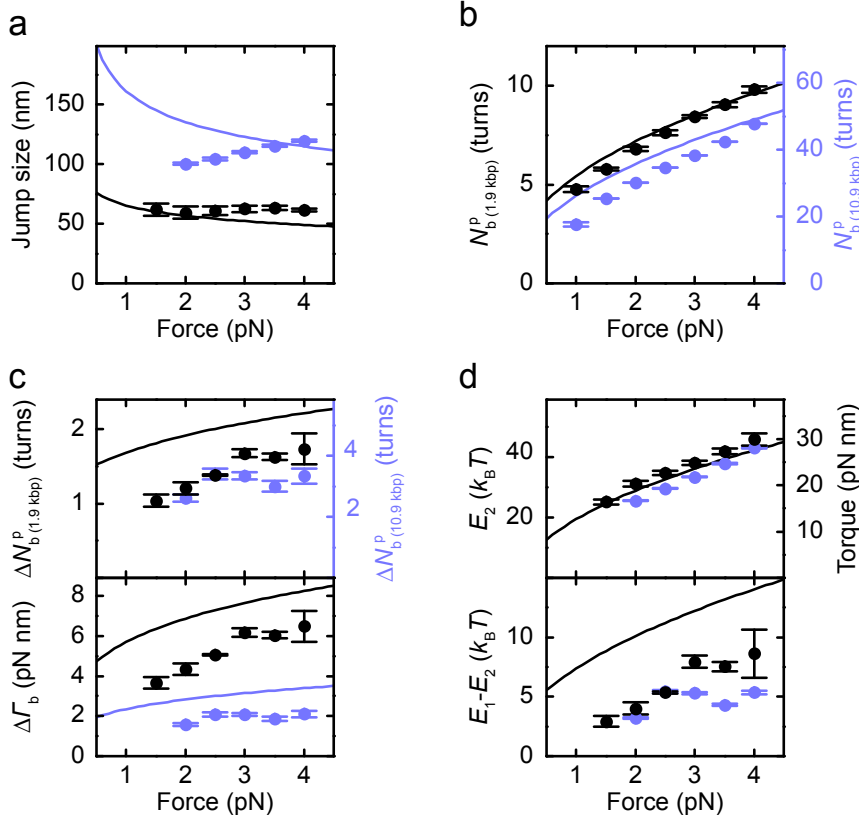


Figure 3.7. Force dependence of the buckling transition. The characteristic parameters of a 1.9 kbp (black) and a 10.9 kbp DNA molecule (blue) were determined at the buckling transition for various forces. The ionic strength was kept constant at 320 mM Na^+ . Experimental values are shown as filled circles, predictions from the end-loop model as solid lines. In case of an overlap, only the black curve is depicted. (a) Jump size at buckling equilibrium. (b) Position of the buckling equilibrium. To highlight the DNA length dependence, the right axis, corresponding to the 10.9 kbp DNA molecule, was scaled linearly with DNA length compared to the left axis corresponding to the 1.9 kbp DNA molecule. (c) Change of twist transferred into writhe during buckling ΔN_b^P at buckling equilibrium and corresponding torque change $\Delta \Gamma_b = 2\pi C_s/L \cdot \Delta N_b^P$. The expected scaling of ΔN_b^P with the square root of the DNA length is highlighted by scaling the axes accordingly (Eq. 3.13). (d) Top: Superhelix-formation energy E_2 and inferred postbuckling torque. Bottom: Energy difference between the end loop formation energy E_1 and E_2 . Error bars represent the statistical error of the data.

ΔN_b^P , the energetic difference between E_1 and E_2 is also slightly overestimated by the prediction, though the general trend is well described.

3.2.7. Salt dependence of the buckling transition

For the shorter DNA molecule, also the buckling parameters at different Na^+ concentrations in particular 60, 170 and 320 mM were characterized (Fig. 3.8). The general trends are well reproduced by the model presented here. Worth highlighting is the

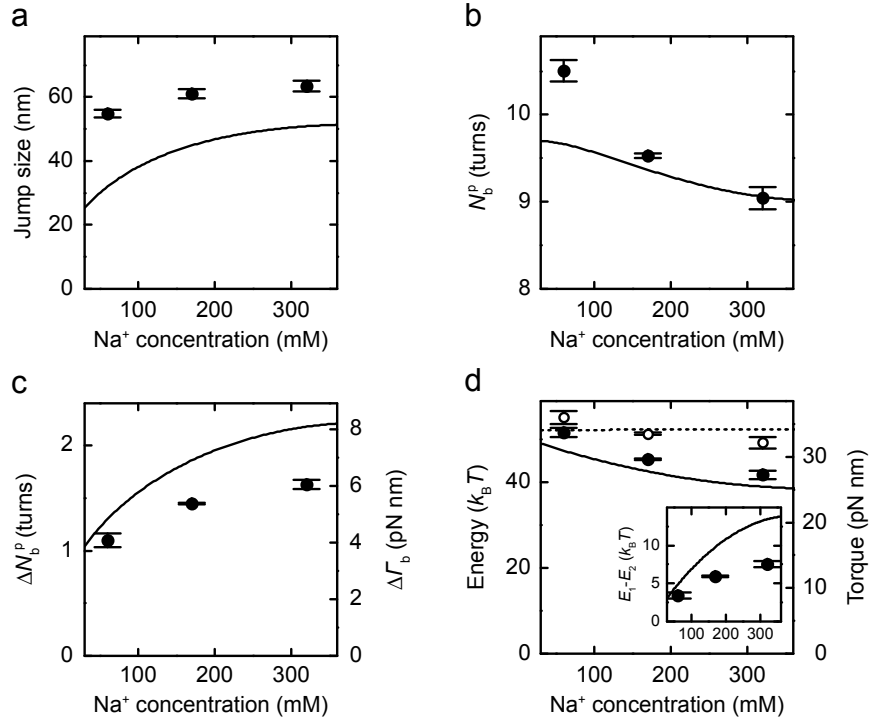


Figure 3.8. Salt dependence of the buckling transition. The parameters characterizing the transition of a 1.9 kbp DNA molecule were measured at differing ionic strength. The applied force was constant at 3.5 pN. Experimental values are shown as circles. Predictions from the end loop model are shown as black lines. (a) Jump size at buckling equilibrium. (b) Position of the buckling equilibrium. (c) Change of twist transferred into writhe during buckling ΔN_b^P at the buckling equilibrium and corresponding torque change $\Delta \Gamma_b$. (d) Superhelix-formation energy E_2 , inferred postbuckling torque (filled circles and solid line) and end loop formation energy E_1 (open circles and dashed line). Inset: Energy difference between E_1 and E_2 .

increase of ΔN_b^P , $\Delta \Gamma_b$, and $E_1 - E_2$ with increasing ionic strength, which lets the abrupt buckling become more pronounced. Interesting is the measured decrease of E_1 with increasing ionic strength (Fig. 3.8d), which is not included in the simple theory. However, as argued above, E_2 decreases even stronger leading to an increase of $E_1 - E_2$ with increasing ionic strength.

3.2.8. Supercoiling kinked DNA

Generally, the end loop model can well describe the observed abrupt buckling at the onset of plectoneme formation. Together with this simple estimates for the plectoneme formation energies it can well reproduce the scaling and the magnitude of most parameters describing the buckling transition, which provides strong support for the model. For most of the Na^+ concentrations considered here E_1 is larger than E_2 , which causes abrupt buckling. However, if one could locally reduce E_1 to become smaller than E_2 , the model would predict the existence of a “prebuckling” state, i.e. an end loop would form before the subsequent superhelix is formed.

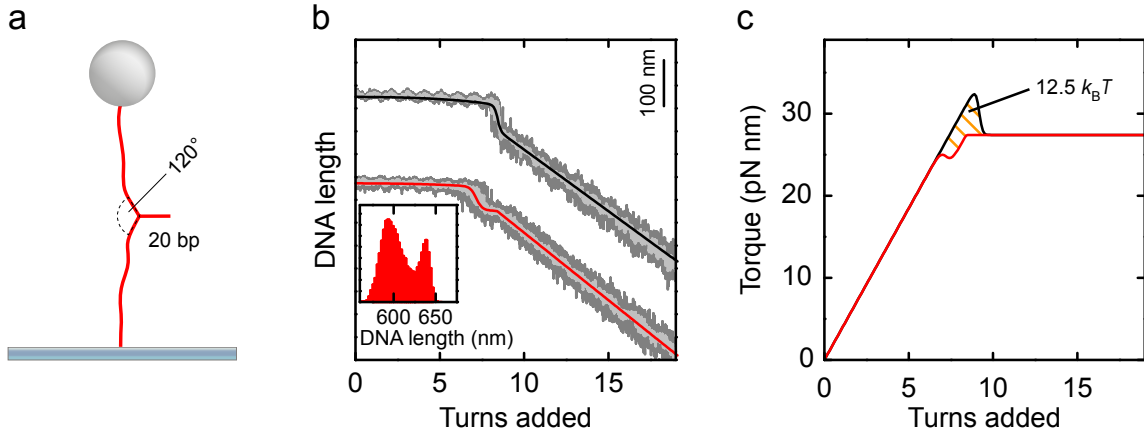


Figure 3.9. Supercoiling kinked DNA. (a) The illustration shows the structure of the DNA kink. A 20 bp hairpin was introduced into the substrate, leading to the formation of a small 3-arm junction. Neighboring arms should join at an angle of approximately 120° . (b) Supercoiling curves for the kinked (lower) and a straight, i.e. unknicked (upper), DNA molecule taken at 3.5 pN and 320 mM Na^+ . Data are acquired at 300 Hz (dark gray lines) and filtered to 20 Hz (light gray lines). Solid red and black lines are calculated according to Eq. 3.15 with the end loop length reduction ΔL_1 , the end loop energy E_1 and the superhelix energy E_2 taken from fits to the data. Inset: Histogram of the DNA length at 7.0 turns for the kinked molecule. (c) Torque development for both molecules as predicted by the model. The shaded area enclosed by the two curves corresponds to the total difference between the end loop energies E_1 for the straight versus the kinked DNA molecule.

To test the prediction, a DNA construct was prepared in which a 3-arm junction was incorporated (see section B.1). This junction introduces a kink of approximately 120° (Fig. 3.9a) and should significantly reduce the end loop formation energy E_1 .

Indeed, in supercoiling experiments prebuckling is found for this substrate. After a first length reduction, occurring much earlier than for a straight DNA molecule, the DNA extension remains constant for almost another turn, during which additional torque builds up. Only then the formation of the superhelix starts causing the linear DNA length decrease with added turns (Fig. 3.9b). Interestingly, the transition at the prebuckling point occurs also abruptly, since two distinct DNA lengths can be identified (Fig. 3.9b, Inset).

Using the expressions derived above for describing DNA length and torque during supercoiling, the supercoiling curves of the kinked DNA can also be reproduced. Therefore one has to choose an appropriate E_1 , which has to be considerably smaller than E_2 . At a force of 3.0 pN and a Na^+ concentration of 320 mM, E_1 is $\sim 4 k_B T$ smaller than E_2 . Using the values for E_1 and E_2 , which best describe the supercoiling curves, one can infer the torque as above from Eq. 3.14. The prebuckling causes the torque to “undershoot” compared to the postbuckling torque. The total difference between the end loop energies E_1 for the straight versus the kinked DNA molecule, corresponding to the area enclosed by the two curves in Fig. 3.9c, is $12.5 k_B T$. This represents an enormous bias for plectoneme nucleation at the DNA kink.

3.3. Consequences of DNA buckling

3.3.1. End loop provides a plectoneme nucleation barrier

In this study the abrupt buckling prior to plectoneme formation was investigated using magnetic tweezers. In addition to the previously reported force dependence [49], the abrupt buckling was found to strongly depend on the ionic strength as well as on the length of the DNA molecule. The data shown here are in agreement with the proposed end loop model [52], in which a higher energy per writhe is required to form the end loop than for subsequent turns in the plectonemic superhelix. Direct support comes from the observed DNA length dependence of the jump size together with the broadening of the transition. Analyzing the transition width (Fig. 3.2c) reveals that the writhe of the postbuckling structure scales within error with the square root of the DNA length. This is a direct consequence of our the model presented in this work, independent of particular values for the plectoneme formation energies. Applying estimates for these energies describes well the dependences of the buckling parameters on the applied force and ionic strength, which provides additional support for the model.

Qualitatively, the dependence on the ionic strength can be understood by an increased repulsion of the DNA strands in the plectonemic superhelix with decreasing ionic strength. Consequently the energy for superhelix formation E_2 increases. Considering that electrostatic interactions within the end loop should play a minor role due to a larger DNA-DNA distance, the difference between the end loop energy E_1 and E_2 decreases and the abrupt buckling becomes less pronounced.

The formation of a second or further plectonemic structures is normally less favorable due to the large end loop formation energy E_1 compared to the smaller energy E_2 required to extend the superhelix. Therefore, plectoneme formation is “nucleation limited”, i.e. for a sufficiently large energetic difference, growth of an already existing plectoneme will be more likely than nucleation and maintenance of an additional one. The obtained values for the energy difference between E_1 and E_2 amount to several $k_B T$ for Na^+ concentrations ≥ 60 mM (Figs. 3.7d and 3.8d). Therefore, under these conditions the presence of only a single plectoneme is much more probable than predicted by a Boltzmann-like distribution for single and multiple plectonemic states.

By contrast, at low ionic strength E_1 can be equal to or smaller than E_2 , in agreement with the observed disappearance of the abrupt buckling transition and the appearance of a smooth and broad transition at 20 mM Na^+ . In this case the presence of multiple plectonemes will be favored. When E_1 is considerably smaller than E_2 , exclusively end loops form. We recently proved this hypothesis by using Monte Carlo simulations for modeling DNA supercoiling at 10 mM monovalent salt [56]. The existence of single, multiple, and more complex plectonemic states needs to be carefully considered for the interpretation of single molecule experiments [28] and the application of theories at low salt concentrations [54, 57].

A more quantitative understanding of abrupt buckling will require rigorous theoretical work. Most importantly, the energetics and shape of the end loop, displaying a tear-drop-like configuration [58], should be appropriately considered. Potential

kinking of the sharply bent plectoneme tip, as well as the salt dependency of the persistence length and the end loop energy need additional attention.

3.3.2. Plectoneme pinning and energy of DNA bending

By introducing a $\sim 120^\circ$ kink into the DNA one can achieve a “prebuckling” state, i.e. buckling that occurred considerably earlier than the actual superhelix formation (Fig. 3.9b). This is a direct consequence of the end loop model, considering that DNA kinking will reduce E_1 to become smaller than E_2 . Therefore it serves as an independent support for the model. Preferential buckling at kinkable regions and regions with discontinuous stiffness has been predicted in static computational models [59] and is now confirmed experimentally.

In contrast to a reduced E_1 at low salt concentrations, the kink acts only locally to favor plectoneme formation at its position. The energetic bias for plectoneme formation at the kink compared to DNA without an artificial kink can reach values in the order of $10 k_B T$ at elevated forces and ionic strength (Fig. 3.9c). Therefore the plectoneme is predicted to be pinned and to stay at the kink position, although this idea still requires independent support. Being able to pin the plectoneme position might be a useful tool, for example for controlled plectoneme extrusion in rotor bead assays [25].

4. The effective charge of DNA

4.1. Challenges in quantifying DNA-DNA interactions

The large linear charge density is a fundamental property of DNA which governs its biological function by influencing DNA folding, packaging [29], pairing [30], and interactions with other biological macromolecules [31]. To develop meaningful quantitative models describing such systems and processes, a precise knowledge of the interaction between two DNA molecules, which is mostly of electrostatic origin, is mandatory. DNA electrostatics is affected by surrounding counter ions, which screen the DNA charge on the scale of the Debye length λ_D . The counter ion cloud is mainly set by the interplay between solute-ion electrostatic attraction and entropic repulsion, for which the Poisson-Boltzmann (PB) equation provides a mean-field description. For highly charged polymers such as DNA, this approach can have considerable limitations arising from the reduced structural detail with which the DNA macromolecule is approximated and the assumption of a continuous counter ion density. To offset these problems, it is common practice to rescale DNA electrostatic potentials with a charge adaptation factor. Values between 70% and 100% of the bare DNA charge density are typically used [46, 60, 61], but the correct parameterization is debated [60]. Often such factors are indirectly obtained from electrophoresis experiments [62], which are unrelated to DNA-DNA interactions [63, 64]. Direct experimental studies of DNA-DNA interaction are rare and themselves limited e.g. to condensed DNA phases [65], short DNA particles [66] or large distances [67, 68]. Despite increasingly sophisticated experiments, an unambiguous quantitative assessment of DNA-DNA interactions has not been achieved yet.

Here this issue was addressed by analyzing the ionic strength-dependent supercoiling response of single DNA molecules held under constant tension in magnetic tweezers experiments. The supercoiling experiments resembled the ones described in the previous chapter, however, here instead of the buckling transition the slope in the superhelical phase dL/dN was analyzed (Fig. 4.1a). This slope depends on the applied force (Fig. 4.1b) and on the ionic strength of the solution (Fig. 3.1b). Several models have been developed to describe this dependence theoretically [51, 54], but a quantitative prediction of the slopes has not yet been achieved [27, 54] (Fig. 3.5).

4.2. Energetic considerations

To provide an improved description of the superhelical regime, the energy per added turn to form an ideal DNA superhelix $E_{\text{tot}}^{\text{sh}}$ with superhelical radius ρ and helical repeat length h in the absence of fluctuations was calculated [46, 54, 60] (Fig. 4.1a),

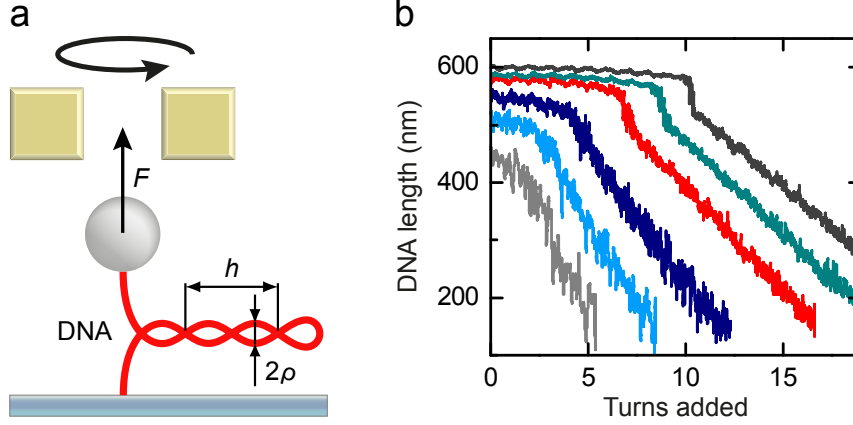


Figure 4.1. Dependence of DNA supercoiling on the force and salt concentration. (a) A DNA molecule is tethered between a glass surface and a $1.0 \mu\text{m}$ magnetic bead. Nearby magnets allow to stretch and twist the attached molecule. Once a critical supercoil density is reached, the end-to-end distance decreases linearly with the number of added turns as the extrusion of a superhelical structure absorbs the additional turns in the form of writhe. The helical repeat length h and the superhelical radius ρ is indicated. (b) DNA supercoiling curves recorded in buffer containing 170 mM Na^+ at stretching forces of 0.25, 0.5, 1.0, 2.0, 3.0 and 4.0 pN (gray, light blue, dark blue, red, green and dark gray lines, respectively) for a 1.9 kbp long DNA molecule. Continuous twisting was carried out at 0.5 Hz. Data was taken at 300 Hz and smoothed to 20 Hz.

with the DNA charge as a free parameter:

$$E_{\text{tot}}^{\text{sh}} = E_{\text{pot}}^{\text{force}} + E_{\text{bend}}^{\text{DNA}} + E_{\text{Estat}}^{\text{DNA}}. \quad (4.1)$$

$E_{\text{pot}}^{\text{force}}$ denotes the potential energy change due to shortening the DNA end-to-end distance against the applied force F , $E_{\text{bend}}^{\text{DNA}}$ the bending energy of the DNA within the superhelix and $E_{\text{Estat}}^{\text{DNA}}$ the DNA-DNA electrostatic interaction energy.

Per added turn, i.e. per superhelical writhe, the DNA length within the superhelix grows by [46]: $[(2\pi\rho)^2 + h^2]/h = dL/dN$, which equals the slope of the supercoiling curves when neglecting fluctuations. $E_{\text{pot}}^{\text{force}}$ is then given by:

$$E_{\text{pot}}^{\text{force}} = F \cdot \frac{dL}{dN}. \quad (4.2)$$

The bending energy per turn can be written as [46]:

$$E_{\text{bend}}^{\text{DNA}} = \frac{dL}{dN} \cdot \frac{1}{2} \cdot p \cdot k_{\text{B}}T \cdot \left[\frac{\rho}{\rho^2 + (h/2\pi)^2} \right]^2, \quad (4.3)$$

where $p = 50 \text{ nm}$ denotes the bending persistence length, k_{B} the Boltzmann constant, and T the absolute temperature. The term within brackets describes the DNA curvature.

One can calculate the electrostatic interaction energy between the two DNA double-strands of the superhelix as previously described [69, 70]. The electrostatic potential Φ

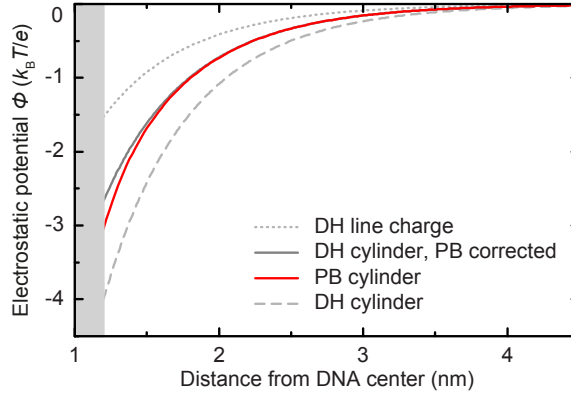


Figure 4.2. Electrostatic potential around the DNA. The DNA is modeled as a charged cylinder and the potential calculated at 170 mM monovalent ions as applied within the theory presented here. For comparison the full Poisson-Boltzmann solution is given as well. A converging numerical solution for the electrostatic potential to the nonlinear PB equation (red line) was obtained from finite-element simulations in a one-dimensional geometry. The solution of the linearized PB, i.e. the Debye-Hückel, equation for a charged, straight line with the same charge density (gray dotted line) was calculated using Eq. 4.4. The solution of the DH equation for the cylindrical geometry (dashed gray line) is obtained as described in the text. Also shown is the DH solution corrected for the high DNA charge density (solid gray line, see text). The obtained potential is in good agreement with the full solution of the PB equation with minor deviations close to the cylinder surface. Since χ_{PB} approximates 1 for low charge densities, the deviations shown in the figure for $\chi_{CA} = 1$ decrease even more for $\chi_{CA} = 0.42$. The cylinder boundaries are represented by a gray box.

around the DNA is described by the Poisson-Boltzmann equation (red line in Fig. 4.2). However, as there exists no analytic solution to this equation, several adaptations are performed. In a basic model, the DNA is approximated as a line with charge density $\chi_{CA} \cdot \xi$, where χ_{CA} is the adjustable charge adaptation factor and $\xi = 2e/0.34$ nm is the nominal charge density. The solution of the linearized PB, i.e. the Debye-Hückel (DH) equation for a charged, straight line with the same charge density (gray dotted line in Fig. 4.2) is obtained by integrating point charge potentials placed at the center-line of the opposite double-strand:

$$\Phi = k_B T \cdot l_B \cdot \chi_{CA} \cdot \xi \int_s \frac{e^{-r(s)/\lambda_D}}{r(s)} ds \quad (4.4)$$

with $l_B = 0.7$ nm being the Bjerrum length in water. $r(s)$ denotes the distance between a point located at position s of the center-line of one double-strand and a fixed point located at the center-line of the other double-strand of the superhelix. Numeric integration is performed over the whole center-line s of the former double-strand.

To describe the actual electrostatic potential more accurately, the DNA is approximated as a cylindrical, uniformly charged rod with a radius of $a = 1.2$ nm. The solution of the DH equation for the cylindrical geometry (dashed gray line in Fig. 4.2) is obtained the same way as in the linear approximation by multiplying ξ with χ_{rod} , a geometry compensating factor; $\chi_{rod} = \lambda_D / [a \cdot K_1(a/\lambda_D)]$, where K_1 is the 1st order

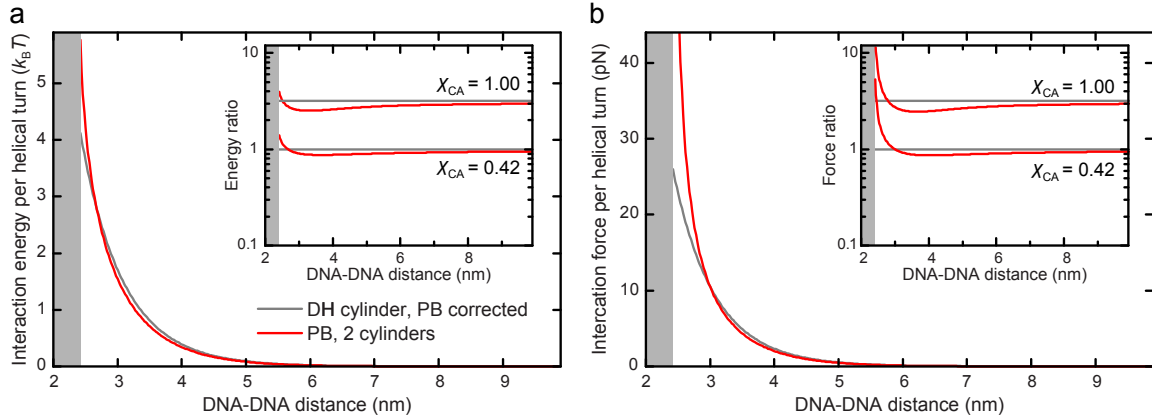


Figure 4.3. Interaction energies and forces between two DNA molecules. The DNA molecules are modeled as two charged cylinders and the energies and forces calculated at 170 mM monovalent within the theory presented here. For comparison the full Poisson-Boltzmann solutions are given as well. The DNA-DNA distance is defined here as the separation of the center-lines of the cylinders. (a) Interaction energies and (b) forces were calculated for two parallel homogeneously charged cylinders. Curves obtained from full PB solutions are shown as red lines. Numerical solutions for the electrostatic potential of the nonlinear PB equation in a bicylindrical coordinate system were obtained as described [72] from finite-element simulations. Simplified calculations as applied in this theory including an adapted DNA line charge density with $\chi_{CA} = 0.42$ are shown as gray lines. The obtained potentials were then used to calculate the interaction energies and forces within the PB formalism [72]. Approximate interaction energies as applied within this theory were calculated according to Eq. 4.5. The insets depict the ratios of the interaction energies and forces obtained from full PB solutions and adapted DH solutions for values of χ_{CA} of 0.42 and 1.00 with respect to the values from the adapted DH solution with $\chi_{CA} = 0.42$. The gray box denotes the DNA-DNA distances at which the two cylinders would intersect each other.

modified Bessel function of the second kind.

Due to the high DNA charge density the solution of the DH equation deviates significantly from that of the PB equation. Therefore, the DH solution was adapted by multiplication with another charge adaptation factor χ_{PB} to fit the PB solution for large distances (solid gray line in Fig. 4.2). Values for χ_{PB} were taken from Stigter [71]. The final adapted line charge ξ^* density results then to $\xi^* = \xi \cdot \chi_{CA} \cdot \chi_{rod} \cdot \chi_{PB}$.

For an ideal infinite superhelix the electrostatic potential is invariant along the DNA contour and the electrostatic interaction energy per added turn is approximately the product of the calculated potential (see Fig. 4.2) and the adapted charge of one of the double-strands [69], $1/2 \cdot dL/dN \cdot \xi^*$:

$$E_{\text{Estat}}^{\text{DNA}} = \frac{1}{2} \frac{dL}{dN} \cdot k_B T \cdot l_B \cdot \xi^{*2} \int_s \frac{e^{-r(s)/\lambda_D}}{r(s)} ds. \quad (4.5)$$

This simplified electrostatic potential yields values similar to the full numerical solution of the PB equation (Fig. 4.3a). The DNA-DNA distance represents the separation of the center-lines of the cylinders, which are used to model the DNA double helices.

Interaction forces can be obtained by differentiating the interaction energies with respect to the DNA-DNA distance (Fig. 4.3b).

Deviations of the simplified calculations from the full PB treatment are small ($<10\%$ for $\chi_{CA} = 0.42$ for DNA-DNA distances larger than 3 nm) compared to changing χ_{CA} from 1.00 to 0.42 (more than 3-fold change) except for small distances where the cylinders almost touch each other (Fig. 4.3). The stronger repulsion at short distances found for the PB solutions cannot explain the small effective charge used to

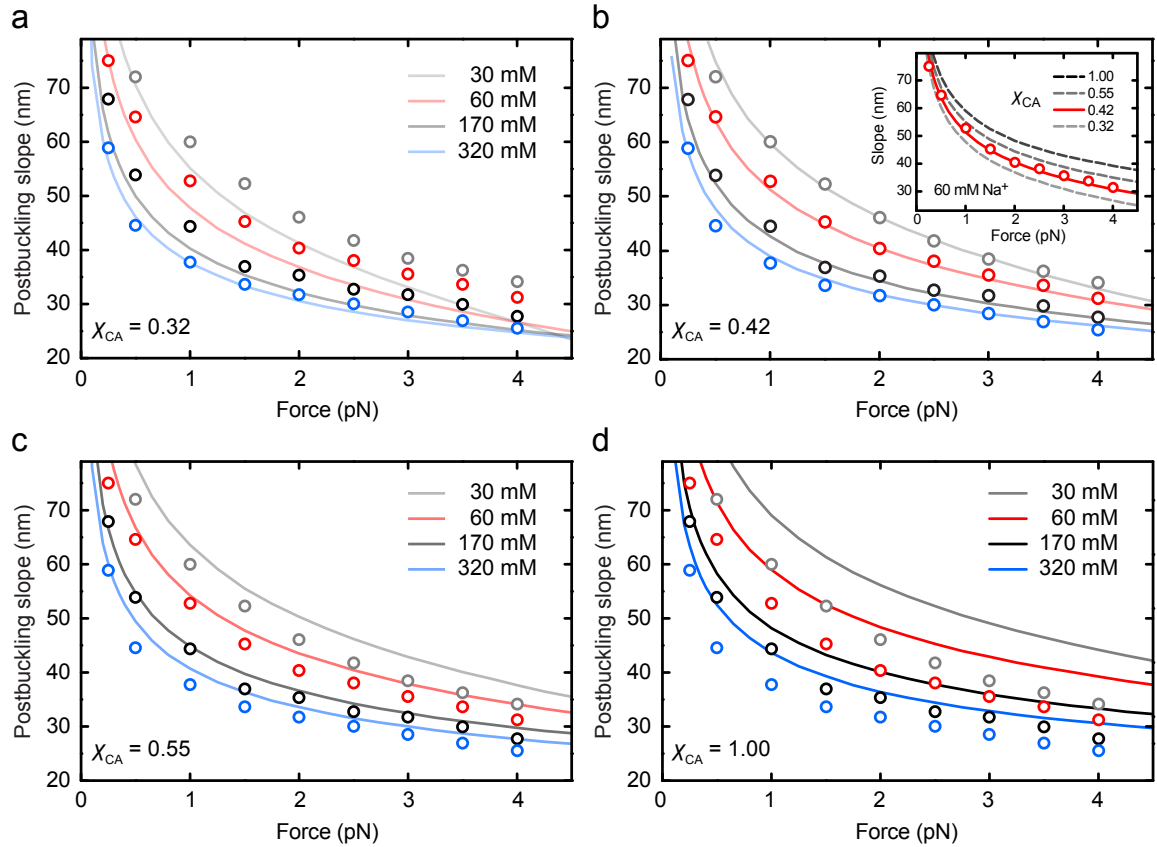


Figure 4.4. Supercoiling slopes for different amounts of charge adaptation. The experimentally obtained slopes from supercoiling curves were compared with predictions of the theoretical model for different values of the charge adaptation factor χ_{CA} . Experimental slopes from Fig. 4.1 are shown as open circles. Predictions for (a) $\chi_{CA} = 0.32$, (b) $\chi_{CA} = 0.42$, (c) $\chi_{CA} = 0.55$, and (d) $\chi_{CA} = 1.00$ are shown as solid lines. Gray, red, black and blue colors indicated values obtained for Na⁺ concentrations of 30, 60, 170 and 320 mM, respectively. (b, inset) Slopes for 60 mM Na⁺ (red circles) together with theoretical predictions for different values of χ_{CA} (lines). DNA substrates consisted of a 1865 bp or a 10.9 kbp linear fragment. At either end ~ 600 bp attachment handles, carrying multiple biotin- or digoxigenin-modified bases, were added by ligation. Supercoiling experiments for forces ≥ 1 pN were carried out exclusively on the short substrate. At lower forces, additional measurements were made using the long substrate in order to obtain more reliable slope values. All measurements were performed at room temperature in 10 mM phosphate buffer at 7.5 pH, supplemented with varying amounts of NaCl to achieve the final Na⁺ concentrations.

describe the supercoiling data, since the interactions calculated from the adapted DH solutions already underestimate the interaction from the PB solutions, which would thus correspond to an even smaller effective value of χ_{CA} .

By combining Eq. 4.1 to 4.5 one can now calculate $E_{\text{tot}}^{\text{sh}}$ and by minimization with respect to ρ and h one obtains the slope dL/dN and the DNA torque $\Gamma = E_{\text{tot}}^{\text{sh}}/2\pi$ for the energetically favored superhelix configuration.

4.3. An adapted DNA charge describes the experimental findings

4.3.1. Comparing the model to the slopes of the supercoiling curves

The predictions of the model presented in this work can be compared with the experimentally obtained slopes of the supercoiling curves for forces between 0.25 and 4 pN (Fig. 4.1b) in buffers containing 30 mM to 320 mM Na^+ . Remarkably, the slopes at all applied forces and ion concentrations are accurately described (Fig. 4.4b). However, achieving the agreement required a substantial reduction of the DNA charge by employing $\chi_{CA} = 0.42$, independent of the salt concentration. Changing χ_{CA} from its optimum value of $\chi_{CA} = 0.42$ leads to a global under- or overestimation of the slopes at all salt concentrations (Fig. 4.4a, c, and d). These deviations occur most prominently at higher forces, i.e. for small superhelix radii (Fig. 4.12b). They are relatively less pronounced (inset in Fig. 4.4b and Fig. 4.6c) at low forces (≤ 1 pN), i.e. larger superhelix radii. This likely explains why previous theoretical work [46, 60] and MC simulations [61, 68] describing the configurations of supercoiled plasmid DNA with larger superhelix radii were less sensitive to the correct choice of χ_{CA} .

The theoretical model accurately describes the slopes of recently available, independently measured supercoiling curves [27](Fig. 4.5a). Since the force dependence of

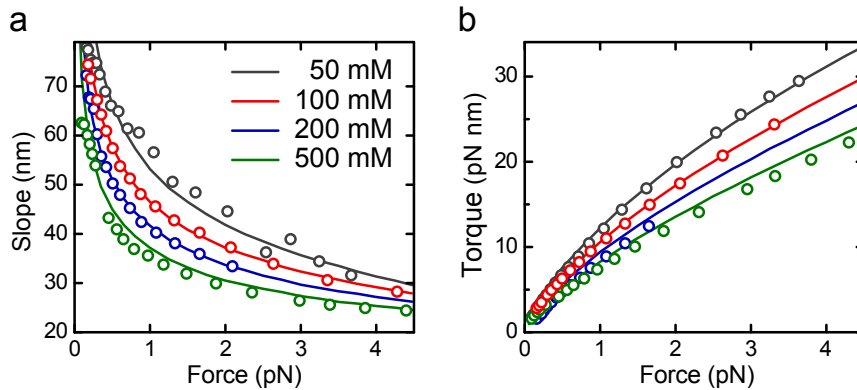


Figure 4.5. Charge adaptation model vs. data from Croquette and coworkers.

The predictions from the theoretical model were compared with data from Ref. 27. (a) Slopes after buckling versus force for different Na^+ concentrations. Circles represent experimental data, solid lines the theoretical prediction for $\chi_{CA} = 0.42$. (b) Torque after buckling as calculated from force-extension data [27]. Colors and symbols are as in a. The slopes at elevated ionic strength and the torques at all ionic strength approximately scale with a power law [27].

slope and torque are linked [73], the model shown here also reproduces the torque in the superhelical phase as obtained from force-extension data [27] (Fig. 4.5b). The obtained χ_{CA} is found to be rather insensitive to other parameters of the model, e.g. changing the weakly salt dependent persistence length by 5 nm alters χ_{CA} only by ± 0.03 .

4.3.2. Verification of the model via Monte Carlo simulations

To exclude the possibility that the small effective charge is an artifact due to neglected fluctuations, coarse-grained Monte Carlo (MC) simulations were carried out

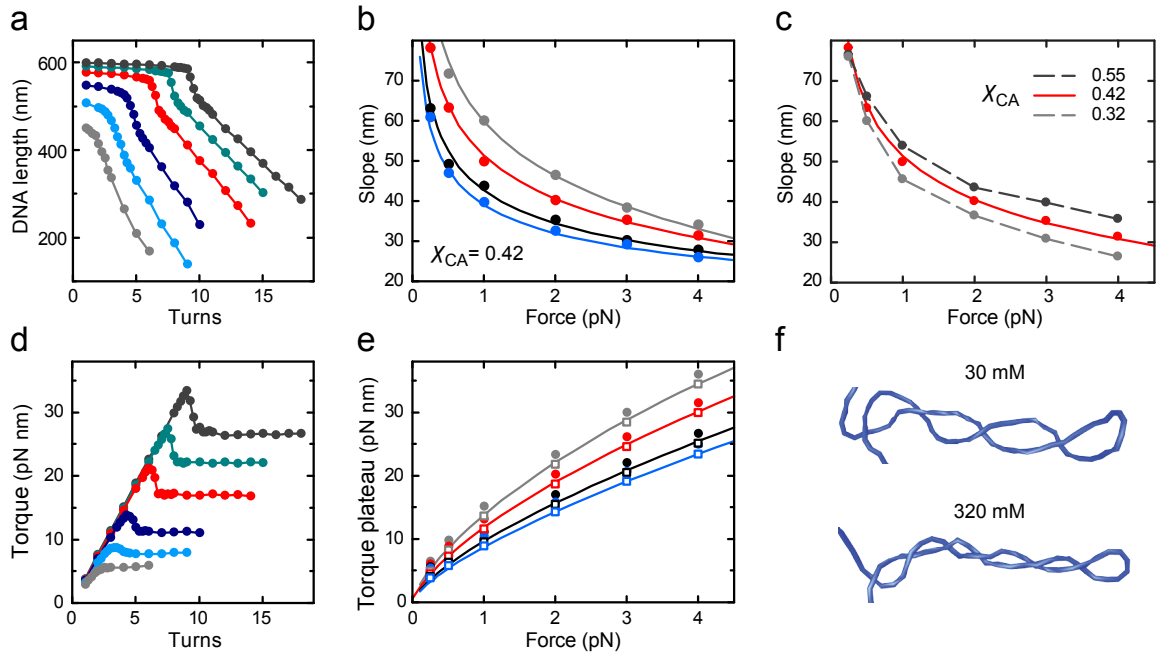


Figure 4.6. Coarse-grained Monte Carlo simulations of DNA supercoiling. (a) Simulated DNA supercoiling curves for 170 mM Na⁺ at stretching forces of 0.25, 0.5, 1.0, 2.0, 3.0 and 4.0 pN for $\chi_{CA} = 0.42$ (colors are as in Fig. 4.1b). Buckling is followed by a linear DNA length decrease with added turns at constant torque. (b) Slopes after buckling obtained from the simulated curves for Na⁺ concentrations of 30, 60, 170 and 320 mM (circles, colors as in Fig. 4.4) and corresponding predictions from the theoretical model for χ_{CA} of 0.42 (solid lines). (c) Slopes from simulated curves at 60 mM Na⁺ for $\chi_{CA} = 0.42$ (red dots) as well as for $\chi_{CA} = 0.32$ and $\chi_{CA} = 0.55$ (gray dots with dashed lines). The prediction for $\chi_{CA} = 0.42$ is shown as a solid red line. (d) Torque during DNA supercoiling for the curves shown in b. (e) Torque after buckling as obtained from the simulations (filled circles) and after subtraction of 1.5 pN nm (open squares) together with the corresponding predictions from the theoretical model for χ_{CA} of 0.42 (solid lines). Na⁺ concentrations and colors are as in c. (f) Snapshots of the formed plectoneme at 1 pN and 8 turns in the presence of 30 and 320 mM monovalent ions.

(Fig. 4.6) [74].* The DNA is modeled as a chain of small cylindrical segments, with equivalent terms describing the potential, bending, and electrostatic energies as in the theoretical model. Additional terms account for the twisting and stretching energy [61].

By performing simulations with different numbers of added turns, supercoiling curves very similar to those observed experimentally were obtained (Fig. 4.6a). $\chi_{CA} = 0.42$, the slopes from simulation, theory, and experiments are in excellent agreement over the entire range of applied forces and ionic strengths (Fig. 4.6b). This provides strong, independent support for a small effective DNA charge. Comparing torque values from the simulations and theoretical model, a good overall agreement is found, except the values from simulations appear globally 1.5 pN nm higher (Fig. 4.6e). This deviation might be due to DNA fluctuations, which are neglected in the model (see section 4.4).

MC simulations furthermore reproduce the experimentally observed abrupt buckling at the onset of the plectonemic phase (Fig. 4.6a), which is accompanied by a torque overshoot (Fig. 4.6d). This buckling transition is a sensitive benchmark and has been used in a further study to evaluate the applicability of various models describing tightly bent DNA conformations.

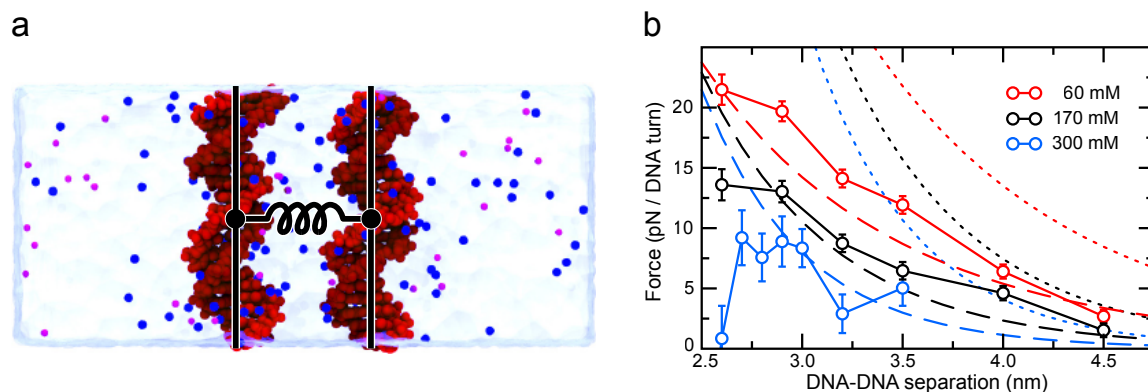


Figure 4.7. Molecular dynamics simulations of two interacting DNA molecules. (a) All-atom model. The DNA atoms are depicted as red spheres, counter- and coions as blue and purple spheres, respectively, and water as a semi-transparent molecular surface. The distance between the DNA molecules was restrained by a harmonic potential, schematically depicted as a spring. (b) Mean force between the DNA molecules from MD simulations (circles, solid lines) alongside the theoretical predictions for $\chi_{CA} = 0.42$ (dashed lines) and 1.00 (dotted lines) at 60 (red) and 170 mM (black) bulk ion concentrations. Data for 300 mM (blue) is reproduced from previous work [76].

4.3.3. Molecular dynamics simulations allow a microscopic insight

To obtain a microscopic verification of the charge adaptation χ_{CA} , all-atom molecular dynamics (MD) simulations [76] were employed (Fig. 4.7a).[†] With this type of simulations the force between parallel DNA molecules at different salt concentrations can be determined and compared to the theory presented earlier (see also Fig. 4.3b). Good agreement was obtained with the force calculated according to the model using $\chi_{CA} = 0.42$ (see section 4.2), and very poor agreement with $\chi_{CA} = 1.0$ (Fig. 4.7b).

To test whether the value found for χ_{CA} is specific to DNA-DNA interactions or is a universal constant for DNA electrostatics, the ion distributions around an

*All of the Monte Carlo simulations referred to in this section were carried out by Robert Schöpflin, René Stehr, and Gero Wedemann. For details about this technique see Ref. 75.

[†]All of the molecular dynamics simulations referred to in this section were carried out by Christopher Maffeo and Aleksei Aksimentiev. For details about this technique see [75].

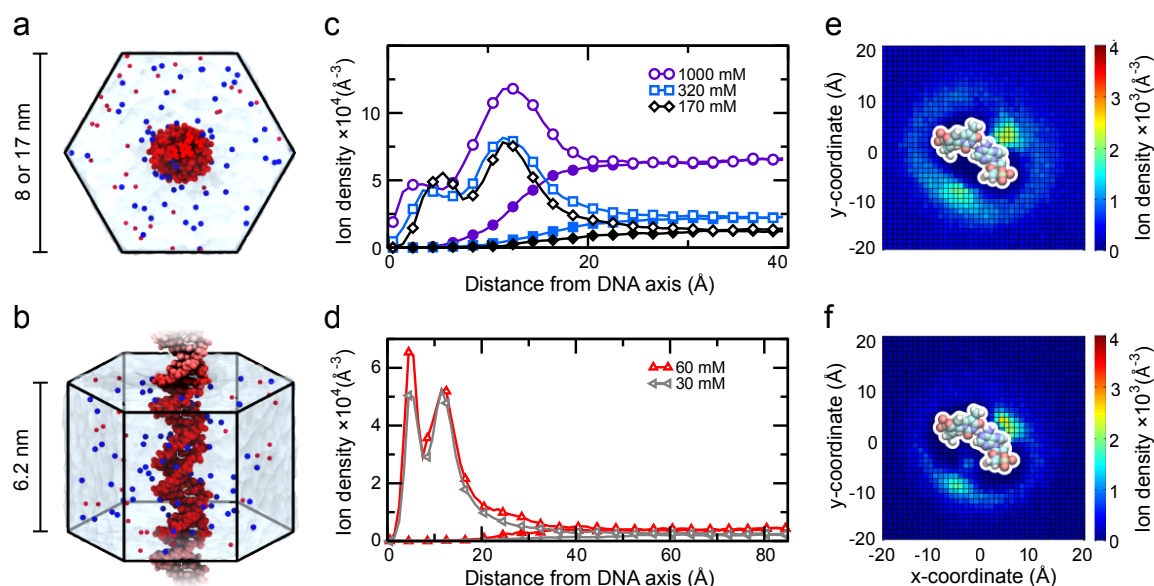


Figure 4.8. The distribution of monovalent ions around double-stranded DNA. (a,b) All-atom model used to find the ion distribution around DNA in MD simulations. The DNA atoms are depicted as red spheres; the counter- and coions are depicted as blue and red spheres, respectively; the water is shown as a semi-transparent molecular surface. (c,d) The radial ion distribution around DNA. Counterion (open symbols) and coion (filled symbols) distributions are shown for (c) 1000, 320, 170 and (d) 60, and 30 mM Na^+ concentrations. (e,f) The 2D counterion density around DNA. A z -dependent rotation was applied in the xy -plane to counter the helical pitch of canonical DNA; the counterion density was subsequently averaged along the z -axis. Data is shown for (e) 320 and (f) 30 mM bulk ion concentrations. A typical basepair is shown after the transformation was applied, indicating the approximate position of the DNA. The transformation has the effect of radially smearing the ion distribution, making it appear as though the ion concentration near the adenine is larger than that near the DNA phosphates (which are located further from the origin). In actuality, more counterions can be found in close proximity of a DNA phosphate than an adenine at a given time.

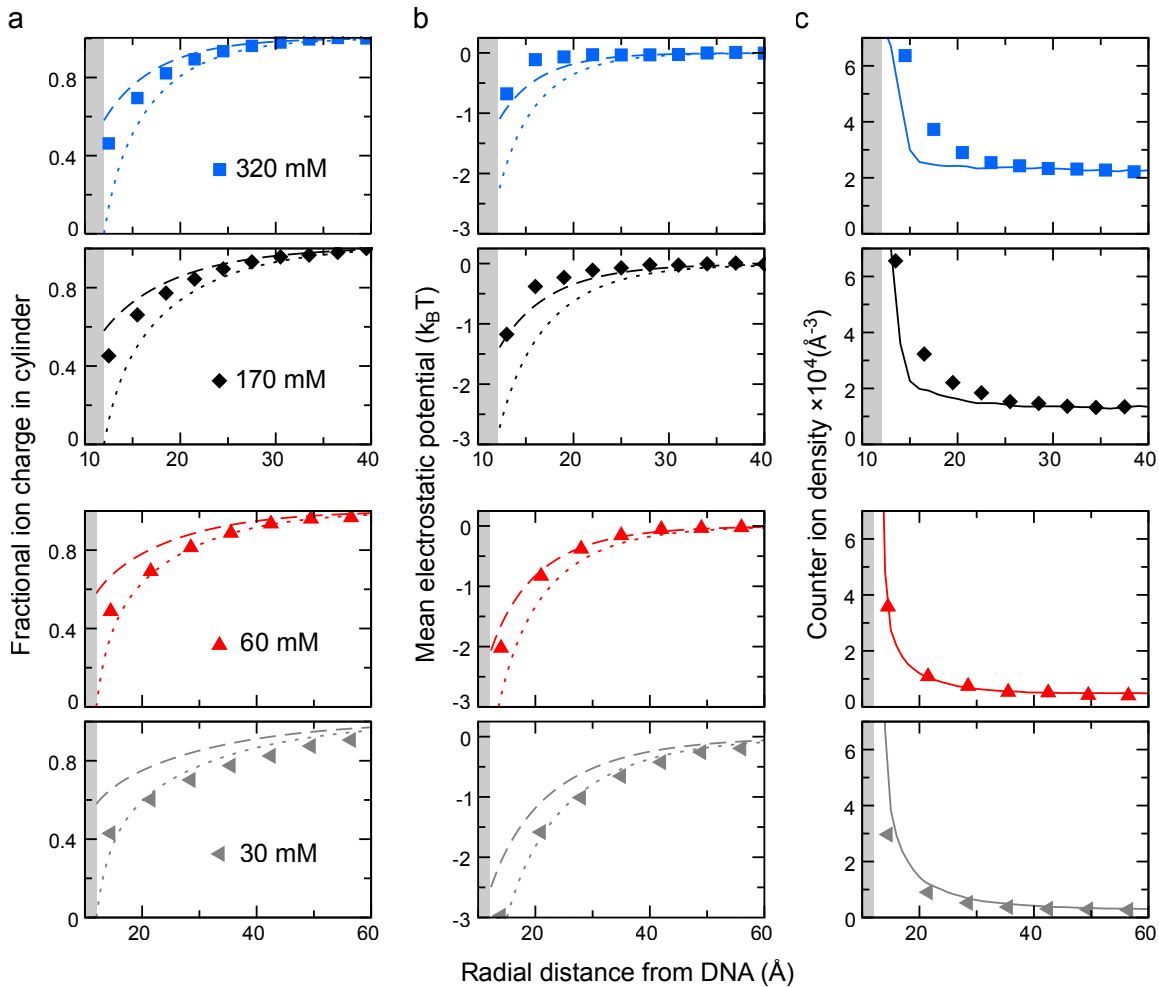


Figure 4.9. Charge distribution and potential around double-stranded DNA. Data resulting from MD simulations described in Fig. 4.8 are plotted as solid symbols. Solutions to the non-linear Poisson-Boltzmann equation for a cylinder of 1.2 nm radius within a hexagonal unit cell (of same size as used in the simulations) are shown for $\chi_{CA} = 1.00$ (dotted lines) and 0.42 (dashed lines) at each ion concentration. The cylinder boundary is represented by a gray box. (a) The fraction of the total ionic charge contained within virtual cylinders of increasing radii as well as (b) the mean electrostatic potential around the DNA nearly matches the PB solution for $\chi_{CA} = 1.00$ at low ion concentration. (c) Comparing the counterion distribution expected from a Boltzmann weight of the potential from the MD simulations in b (solid line) to the directly observed counterion density (symbols) reveals that the mean electrostatics fails to describe the counterion density at high ion concentration.

isolated double-stranded DNA molecule was simulated (Fig. 4.8a and b). The radial ion distribution extended further from the DNA than expected from PB theory with $\chi_{CA} = 0.42$ and approached the distribution for $\chi_{CA} = 1.0$ at low ionic strength (Figs. 4.8d and 4.9a). Thus, the small value for χ_{CA} is specific to DNA-DNA interactions.

At elevated ion concentration, the enclosed charge is somewhere between the PB predictions for $\chi_{CA} = 0.42$ and 1.00 (Fig. 4.9a). The mean electrostatic potential around the DNA was too weak to create the ion distribution as observed in simulation

and as predicted by PB theory (Figs. 4.9b and c). This suggests that ion distributions are not only determined by electrostatics, but that other effects such as correlations in the ion clouds, the non-continuum nature of the dielectric surrounding and ion exclusion can have a significant influence. This in turn is likely to cause the low DNA-DNA interaction forces. Additionally, deviations from the homogeneously charged rod model, such as strongly localized charges at the phosphates and counterions entering the DNA grooves may reduce the interaction forces.

4.4. Effects from fluctuations

It is quite surprising that the model introduced in section 4.2, which neglects fluctuations, provides such an excellent description of the experimentally determined slopes and torques after buckling (see Figs. 4.4b and 4.5). Judging the success of the model by its agreement with the experimental data, one would conclude that it correctly covers the major determinants of superhelix formation under external tension. However, it is also clear that fluctuations should influence the measured parameters. Within this section the reasons for the success of this approach as well as its disadvantages and limitations are discussed.

4.4.1. Verification of the applied parameters

One possible explanation for the agreement of the theoretical approach with the experimental data is that the parameters which enter the formula for the superhelix formation energy $E_{\text{tot}}^{\text{sh}}$ (see Eq. 4.1) were over- or underestimated, thereby compensating the error due to neglected fluctuations.

The only adjustable parameters entering the model are the persistence length p (for which a constant value of 50 nm is taken throughout this chapter) and the DNA charge adaptation factor χ_{CA} . Although the persistence length is expected to depend weakly on the ionic strength [77], varying this parameter within a reasonable range [77] only leads to minor changes of χ_{CA} (changing p by 5 nm alters χ_{CA} only by ± 0.03). Thus, the salt dependence of the persistence length can be neglected within error.

To obtain verification for the charge adaptation factor χ_{CA} , coarse-grained Monte Carlo simulations were carried out (see section 4.3.2) that, by definition, include all fluctuation-based effects, such as undulation enhancement of the electrostatic interactions [60]. No additional entropic energy terms, e.g. due to DNA confinement within the plectoneme [46], are required. The Hamiltonian for the MC simulations includes energy terms corresponding to those in the theoretical model with the same values for the parameters p and χ_{CA} . In addition, the MC simulations include the DNA twist energy, for which a torsional persistence length $p_{\text{tor}} = 100$ nm was assumed [23]. While variations of p_{tor} change the buckling position in an approximately proportional fashion (see chapter 3), they do not impact the slope or torque after buckling. In fact buckling does occur slightly earlier in simulations than in experiments (compare Figs. 4.1b and 4.6a), but this can be adjusted in the simulations by applying a slightly reduced value for p_{tor} of 94 nm as recently reported [27].

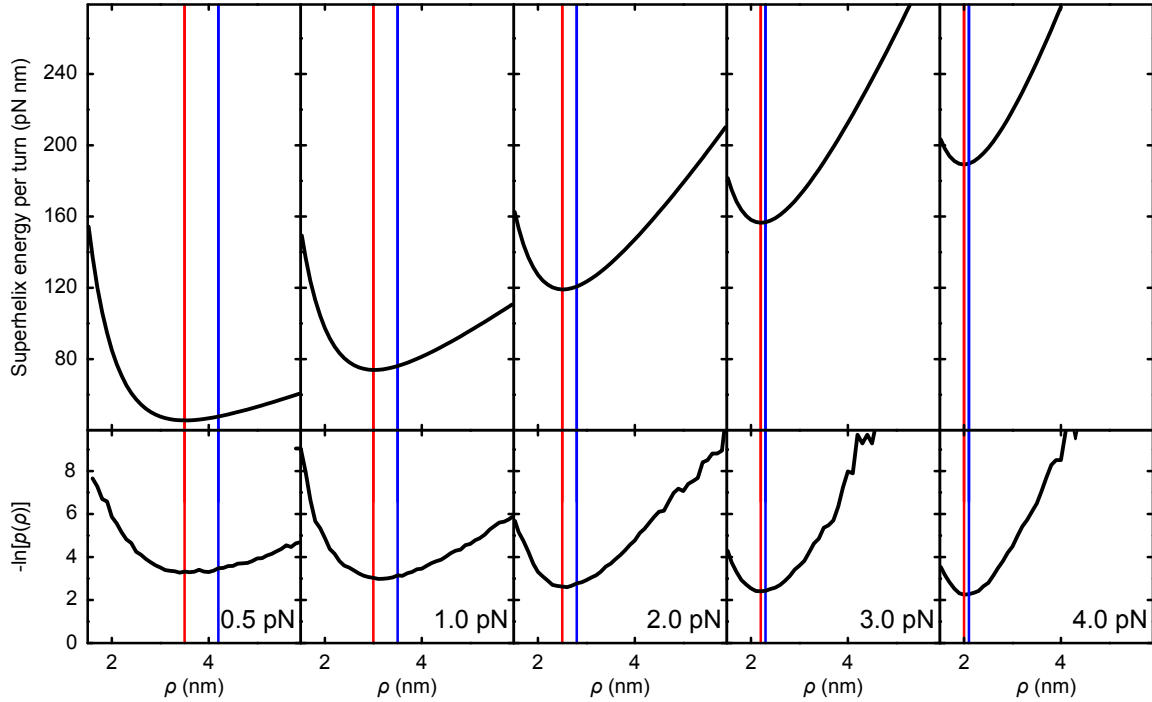


Figure 4.10. Fluctuations of the superhelical radius for various forces. (*Top*) Dependence of the superhelix formation energy $E_{\text{tot}}^{\text{sh}}$ on the superhelical radius ρ around the energy minimum position as calculated from the theoretical model (see Eq. 4.1) at 60 mM monovalent ions. (*Bottom*) Negative natural logarithm of the probability distribution for ρ obtained from coarse-grained Monte Carlo simulations. While the shapes of the energy distributions along ρ as well as the energy minimum positions (red lines) of the theoretical model and the simulations are in good agreement, the mean superhelical radius from the simulations (blue line) is shifted to higher values compared to the position of the energy minimum.

The electrostatic energies as calculated by the theoretical model indeed agree with the MC simulations. In addition, the dependence of the superhelix energy on the superhelical radius ρ was found to agree when calculated using either approach (Fig. 4.10). The superhelix formation energy $E_{\text{tot}}^{\text{sh}}$ was calculated at constant superhelical pitch h from the theoretical model (see Eq. 4.1) and compared to the negative natural logarithm of the probability distribution for ρ obtained from coarse-grained Monte Carlo simulations. It corresponds in arbitrary units to the energy to form a superhelix with radius ρ albeit with non-constant h . While the shapes of the energy distributions along ρ as well as the energy minimum positions of the theoretical model and the simulations are in good agreement, the mean superhelical radius from the simulations is shifted to higher values compared to the position of the energy minimum. This is most pronounced at lower forces. Due to the asymmetry of the energy distribution, deviations of ρ from the minimum position towards higher values are preferred over deviations towards lower values. The good agreement between the shapes of the energy distributions from theory and simulations serves as an independent validation that equivalent energy terms have been used in both approaches.

Mistakes due to imprecise writhe estimates can also be excluded, since the twist is explicitly included for each segment in the MC simulations. Writhe calculations are only carried out to prevent MC moves in which strands would virtually cross each other and change the linking number (defined as twist plus writhe) by ± 2 .

For $\chi_{CA} = 0.42$ the slopes from the MC simulations are in excellent agreement with the ones predicted by the theoretical model (Fig. 4.6b). Therefore, $\chi_{CA} = 0.42$ must be applied in order to describe the supercoiling data given the manner with which the electrostatic interactions are calculated.

4.4.2. Applying additional entropic energy terms

In previous theoretical work on supercoiled plasmid DNA, additional entropic energy terms have been included to model the effect of the confinement that DNA experiences within a tight plectonemic superhelix compared to the more freely fluctuating non-superhelical state. Marko & Siggia [46] considered the additional free energy per DNA length $E_{\text{entr}}/L = [p^{-1/3}(h/2)^{-2/3} + p^{-1/3}\rho^{-2/3}] \cdot k_B T$ to model confinement of the radial fluctuations within the superhelical radius ρ and pitch fluctuations within the superhelical repeat length h . Ubbink et al. [60] considered a similar confinement, where the radial fluctuations are limited to an adjustable confinement length d_r and

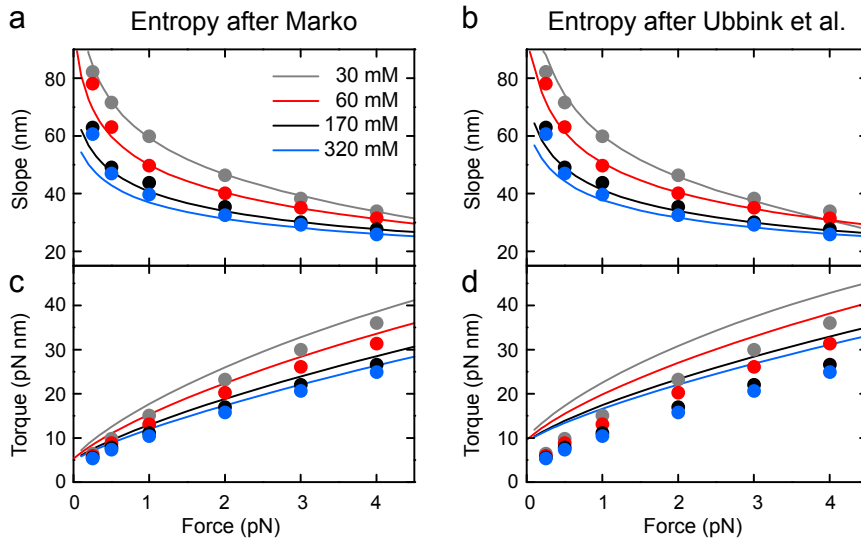


Figure 4.11. Model predictions including fluctuations. (a,c) Slopes, torques after buckling from coarse-grained Monte Carlo simulations together with theoretical predictions that include an entropic energy term after Marko & Siggia [46] (see text for details). (b,d) Slopes, torques after buckling from MC simulations together with theoretical predictions that include an entropic energy term and electrostatic undulation enhancement after Ubbink et al. [60] (see text for details). Data from MC simulations is shown as filled circles, theoretical predictions as solid lines. For both models $\chi_{CA} = 0.45$ was taken, for which best agreement of the slopes was obtained.

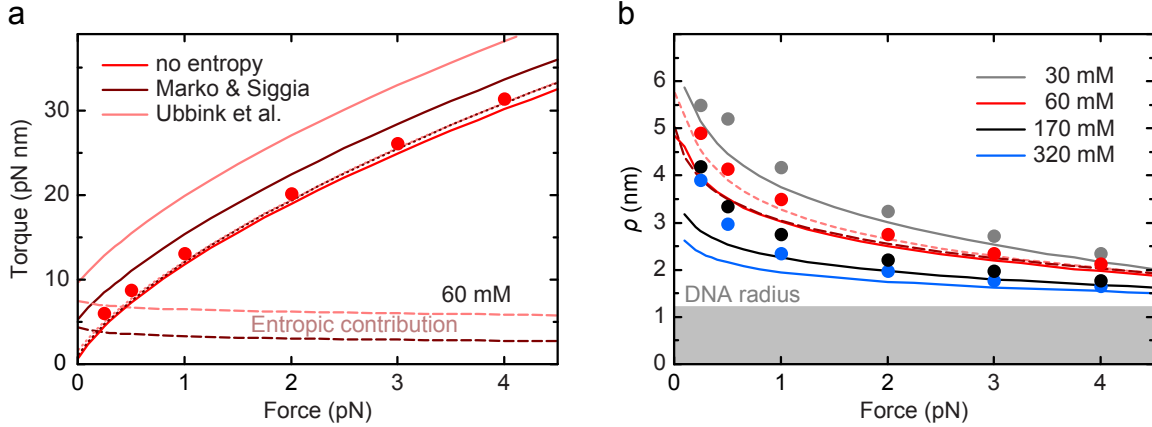


Figure 4.12. Entropic contributions to superhelix formation. (a) Torque after buckling at 60 mM Na⁺ from coarse-grained Monte Carlo simulations (red circles) together with predictions (solid lines) from the theoretical model (see section 4.2), which neglects entropy, and alternative models (see text for details) including entropic terms after Marko & Siggia [46] (brown line) and Ubbink et al. [60] (rose line). Dashed lines represent the entropic contributions to the torque. Dotted lines are obtained from the total predicted torque after subtracting the entropic contributions from the alternative models as well as the electrostatic undulation enhancement of about 2 pN nm (not shown) from the model of Ubbink et al. Predictions were calculated using $\chi_{CA} = 0.42$ for the model excluding entropy and $\chi_{CA} = 0.45$ for the models including entropy. (b) Mean superhelical radius ρ for different salt concentrations obtained from coarse-grained MC simulations (circles) and predictions from the model excluding entropy (solid lines). For 60 mM Na⁺ also the predictions for the two models including entropy are shown (dashed lines, colors as in a).

the pitch fluctuations to $h/2\pi$ with

$$E_{\text{entr}}/L = (3/2)^{8/3} \cdot \left[p^{-1/3} (h/2\pi)^{-2/3} + p^{-1/3} d_r^{-2/3} \right] \cdot k_B T. \quad (4.6)$$

Additionally Ubbink et al. introduced a correction to the electrostatic interaction energy due to radial superhelix fluctuations leading to an enhancement factor of $\exp(2d_r^2/\lambda_D^2)$ compared to the interaction energy in the absence of fluctuations.

To better understand the role of fluctuations, in particular the influence of confining the DNA within the superhelix, the energetic corrections from both theoretical works we included in the theoretical model. While the slopes are well described for $\chi_{CA} = 0.45$, the torques are overestimated considerably by the corrections from both theories (Fig. 4.11). Plotting only the entropic contribution to the superhelix free energy reveals an approximately constant offset to the energy for all forces considered. Subtracting the energetic corrections for confinement and fluctuations provides torque values in close agreement with the theoretical model (Fig. 4.12a). This is because the superhelix parameters hardly change when the additional corrections are applied (shown for ρ in Fig. 4.12b).

From this one can formulate two conclusions: Firstly, including energetic penalties for confinement of the DNA within a tight superhelix does not lead to an increase of the superhelix dimensions. Secondly, the actual free energy contributions of the

fluctuations are considerably smaller than predicted for supercoiled plasmids. The latter is not surprising, since DNA under tension is already significantly confined before superhelix formation compared to relatively freely fluctuating non-superhelical, circular DNA. Additionally, extrusion of a superhelix, which can freely diffuse along and around the stretched part of the DNA, liberates some of the confinement of the stretched configuration. In the opinion this is the most likely reason for the relatively small entropic contributions to the free energy of superhelix formation.

Though the predictions for supercoiled plasmids do not provide a correct quantification of the entropic contributions for DNA under tension, it is interesting to note that they seem to add a constant energetic offset for the range of forces considered. Comparing the torque predictions from the theoretical model with the torque from the MC simulations reveals a constant offset of ~ 1.5 pN nm for all forces and salt concentrations (Fig. 4.6e, see section 4.3.2), which is likely the aforementioned contribution due to fluctuations.

4.4.3. Fluctuations within stretched vs. superhelical DNA

An additional complication arises when considering the influence of fluctuations on DNA length changes. If one considers the average DNA path, i.e. the average over the DNA fluctuations in time, it appears to be always shorter than the contour length of the molecule. Thus, for DNA under tension, the end-to-end distance is always shorter than the contour length and the DNA can be considered as an entropic spring. Consequently, within a DNA supercoiling experiment, the plectonemic superhelix takes up more DNA per added turn than indicated by the slope of the supercoiling curve. To account for the additional DNA sequestered within the average DNA path, previous works [54, 57] solved for superhelix parameters in the absence of fluctuations, as done here, and scaled the resultant slopes by the relative extension z of the DNA at zero twist, defined as the end-to-end distance under the given tension divided by the contour length of the DNA.

This approach, however, ignores the strong dependence of z on the DNA twist, which is particularly large at low forces (see also section 3.2.5). More importantly, only the average DNA path is rescaled but not the relevant energy terms which define the superhelix dimensions.

The superhelix energy should, however, be rescaled to account for the rescaling of the DNA geometry and the resulting rescaled energy should be minimized to produce a new set of superhelix parameters. When rescaling with z as done before [54, 57] one could assume that the fluctuations contributing to z are suppressed within the superhelix (with $z = 1$ within the superhelix) so that only the potential energy imposed by the applied tension would need to be rescaled (i). Alternatively, all energy terms could be linearly rescaled by z (ii). The first possibility would lead to different superhelix parameters and therefore to a different slope prediction than previously determined [54, 57], whereas the second approach would provide slopes (as obtained before [54, 57]) and torques, both rescaled by z .

However, fluctuations do occur within the plectoneme, so $z = 1$ (assumption i) is not obeyed within the plectoneme. Also, the energies for the supercoiled DNA do

not scale linearly with the superhelix dimensions (assumption ii). In particular, the electrostatic interactions do not decrease but rather increase in an approximately exponential fashion upon scaling the superhelix with z . Thus, rescaling all energies linearly (assumption ii) would significantly underestimate the actual electrostatic contribution. In agreement with these arguments, neither approach of rescaling the superhelix energies with z appropriately models the experimental data, since both bias the obtained slopes towards lower values (not shown). Matching the experimental data would require a significantly increased χ_{CA} , which contradicts the results from the MC simulations. Still, the dependence of the slopes on force would be poorly reproduced; adjusting χ_{CA} to obtain agreement for the slopes at elevated forces provides significant underestimation of the slopes at lower forces.

4.4.4. Justification of the model neglecting fluctuations

It seems surprising, that the simple approach presented here, which ignores fluctuations, describes well the experimental findings. A possible reason might be that the relative extension within the superhelix remains unchanged compared to the stretched DNA, i.e. that the bending fluctuations are not affected by the confinement of the DNA within the superhelix with z being constant throughout the molecule. In this case, the superhelix from the theoretical model can be viewed as an effective path obtained after averaging out the fluctuations around it. The superhelical geometry and potential energy due to the applied tension would be correctly described; only the bending energy and the electrostatic interaction energy would change. These changes are considered to be minor, and in case of the electrostatic interactions even to cause a further reduction of χ_{CA} . Comprising more DNA, i.e. more charge, per average superhelical path length together with an enhancement of the effective electrostatic repulsion due to undulations [60] leads to an increased electrostatic contribution, which would need to be adjusted by lowering rather than increasing χ_{CA} . Thus, if assuming a constant z throughout the molecule, the approach is expected to provide a reasonable description of the experimental slopes with minor adaptations for electrostatic and bending energies.

Another way of looking at the problem is to consider the asymmetry of the fluctuations of superhelix radius and pitch. Compared to the energetic minimum position, fluctuations that increase ρ and h are preferred over fluctuations which decrease these parameters due to the asymmetry of the energy landscape (shown for ρ in Fig. 4.10), thereby increasing the slope (one should note here that judging from the energy landscape of the superhelix (not shown), correlated fluctuations of ρ and h are favored over anti-correlated ones). Indeed, at lower forces, the mean superhelix radius obtained from MC simulations is shifted to higher values (Fig. 4.12b) compared to the most probable radius, i.e. the energetic minimum position. However, theory and MC simulation are in excellent agreement for the most probable radius (Fig. 4.10). Thus to some extent, the model underestimates the mean superhelix dimensions by neglecting the asymmetry of fluctuations.

Under these assumptions it is likely that confinement of the tightly wrapped DNA molecule partially suppresses bending fluctuations within the superhelix. This would

increase z within the superhelix and cause a reduction of the slopes as discussed above for the extreme suppression of the bending fluctuations, where $z = 1$ in the plectoneme was considered. (One should note that such a slope reduction is partially compensated by the writhe originating from bending fluctuations [53], which becomes liberated upon suppression of these fluctuations within the superhelix and needs additional accommodation.)

Furthermore, global superhelix fluctuations favor larger averages for the superhelical parameters ρ and h (Fig. 4.10), leading to a balancing increase in the slopes. The torque offset between the theoretical model and the MC simulations can then be viewed as the occupancy of less energetically favorable superhelix geometries due to ongoing fluctuations.

Therefore the striking agreement of this theoretical model with MC simulations and experimental data is due to opposing effects from the fluctuations - a reduced relative stretching within the superhelix versus fluctuations of the superhelix towards larger dimensions. Previous work ignored the latter part and failed to provide a quantitative description of the supercoiling slopes [54, 57]. In any case the model provides a satisfactory way to calculate and predict slopes and torques in supercoiling experiments under tension, which will be helpful for both future experimental [78] and theoretical work [52].

4.5. Previous investigations of DNA-DNA interactions

There exists a large number of previous studies in which DNA-DNA interactions have been probed. This includes e.g. experiments that investigate DNA sedimentation [79], the knotting probability upon cyclization of DNA [80], the geometry of supercoiled plasmids [46, 60, 68, 81], small-angle x-ray scattering of short DNA oligomers [66], DNA condensation by osmotic pressure [65] and many others. Often long DNA molecules in non-condensed phases are used [46, 60, 68, 80, 81], which is similar to the experimental configuration used here. However, in most of these studies charge adaptation factors χ_{CA} of 0.73 [46, 68, 80, 81] or even higher [60] are successfully applied to model the experimental data. In this section it is explained why previous studies found good agreement for charge adaptation factors substantially larger than 0.42 as proposed in this work and why the experiments shown in this work are more precise in quantifying this parameter.

The frequently applied value of 0.73 for χ_{CA} is based on the pioneering work by Stigter and coworkers, who investigated the effective DNA charge in a quantitative fashion [62, 69, 71]. This particular value of χ_{CA} was obtained from electrophoresis measurements [62] and described the experimental data optimally. In these experiments the effective charge has indeed a large influence on the electrophoretic force as recently confirmed [63]. Despite being based on very different physics, DNA-DNA interactions have been modeled widely using $\chi_{CA} = 0.73$ without validation [46, 61, 68, 80, 81]. A charge adaptation factor from Donnan equilibrium measurements published along-side the electrophoretic measurements was found to be lower by 0.2, but has not found similar popularity [62].

When probing DNA-DNA interactions, often the experimental data is modeled with coarse-grained MC simulations. The DNA-DNA interactions in these simulations are either considered by including an effective hard-wall potential with diameter d_{eff} [67, 74, 79–81] or more appropriately by a Debye-Hückel potential adapted to fit the solution of the Poisson-Boltzmann equation at larger distances (as introduced by Stigter [71] and also applied in this work, see Fig. 4.2) [46, 61, 67, 68]. For the latter potential, an effective diameter d_{eff} can be calculated [69]. Comparing the values of d_{eff} that best describe the experimental data with the predicted values according to Stigter [69] for $\chi_{\text{CA}} = 0.73$ provides excellent agreement and reproduces the scaling of d_{eff} with the Debye length λ_{D} and thus the salt concentration [67, 79, 80]. While there is a nearly linear dependence of d_{eff} on λ_{D} according to the theoretical prediction [69], d_{eff} changes only weakly upon considerably variations of χ_{CA} . For example, reducing χ_{CA} 1.7-fold from 0.73 to 0.42 lowers d_{eff} only by about 10% for monovalent ion concentrations between 1 mM and 1 M. Similarly an increase of χ_{CA} from 0.73 to 1.00 increases d_{eff} only by about 5%. Given the scatter of the available experimental data [67, 79, 80] and some deviation due to the applied hard-wall potentials [67], no precise quantification of the charge adaptation factor can be made; values for χ_{CA} of 0.42, 0.73 and 1.00 are all within the error of the data and therefore are not mutually exclusive for the description of previous experiments.

The reason why the experiments shown here are more sensitive to χ_{CA} than previous ones consists of the externally applied tension in the magnetic tweezers assay. At high forces the interwound DNA segments are brought into very close proximity (down to 3-4 nm between the DNA centers, see Fig. 4.12b). This closely approaches or even goes below the effective hard-wall diameter of the DNA. In the experiments listed above the distances between DNA are typically much larger. For example, in experiments with supercoiled plasmids in absence of external force, which are closely related to this work, DNA-DNA distances barely go below 10 nm [68, 81]. Another advantage of the applied, variable tension is that it allows convenient control of the DNA-DNA distance at a fixed salt concentration (see Fig. 4.12b).

Shown in the inset of Fig. 4.4b and in Fig. 4.6c, the greatest influence of χ_{CA} on the slopes of the supercoiling curves is obtained at high forces, as predicted by the theoretical model and the coarse-grained MC simulations. When increasing χ_{CA} from 0.42 to 0.73, the relative change of the slope obtained from the model is $>20\%$ for forces >4 pN and gradually decreases to only 5% at 0.1 pN, at which DNA-DNA distances similar to experiments on supercoiled plasmids are found. Thus, the sensitivity for the particular charge adaptation factor enters with the applied force, but is lost at low forces. Therefore, previous experiments on supercoiled plasmid DNA [68, 74, 81] will be well described for a large range of χ_{CA} .

In addition, one should note that experiments on supercoiled plasmids [68, 81] as well as single-molecule force-extension measurements of supercoiled DNA [74] are more difficult to interpret quantitatively since the DNA twist rigidity strongly influences the configuration of the supercoiled DNA [74, 82]. This arises because a change of the linking number is simultaneously distributed between twist and writhe in a manner that is strongly dependent on the twist rigidity. In contrast, plectonemic supercoiling under constant force is insensitive to the twist rigidity due to the strict partition of the

response to added turns before (twist increase) and after (writhe increase) buckling. The buckling point depends on the twist rigidity but the slopes of the curves do not. Thus the experiments presented in this work circumvent this problem.

4.6. DNA mechanics for various monovalent electrolytes

In the previous sections it has been shown that a reduced charge should be used to describe the interactions of two DNA molecules in close proximity. In our theoretical description and in the Monte Carlo simulations only the valency of the ions has been considered and not the individual size of the ions. Recently, nanopore translocation experiments were used to probe the effective charge for various salts from the alkali group [83]. By means of molecular dynamics simulation it was found that the number of bound counterions does not depend on the type of counterion. However, the duration, and hence strength, of the bond between ions and DNA increases for smaller counterions.

This altered effective charge for different types of counterions was also expected to affect DNA-DNA interactions. Therefore the supercoiling assay described earlier was used to probe the dependence of the DNA bending and the DNA-DNA interactions in the superhelix on the type of counterion. At first it was investigated if the bending rigidity of the DNA varied depending on the size of the counterions in the buffer.

4.6.1. Dependence of the bending rigidity on the type of counterion

To determine how the DNA bending rigidity was affected by the type of alkaline counterion, the dependence of the extension of the DNA on the applied forces was measured. It has already been shown elsewhere that the DNA flexibility is affected by the ionic strength of the solution. This can be observed as a change in the mean extension of the DNA at a given force. Similarly, magnetic tweezers were used here to determine the mean DNA length at a constant force and ionic strength for different alkaline salts. One advantage of this technique is the stability of the assay. In particular it is possible to exchange relatively large volumes of buffer ($> 200 \mu\text{l}$) without detaching the trapped DNA molecule.

Since the effect of the type of counterion was expected to be minor, experiments were performed at a relatively high ion concentration ($\sim 1 \text{ M}$). Besides the typically used sodium ions, the length of the DNA in an environment containing lithium, which is apart from hydrogen the smallest member of the group of alkali metals, was recorded (Fig. 4.13). The forces were calculated from the lateral fluctuations of the magnetic bead as described in chapter 2. For the preparation of the DNA construct with single biotin- and digoxigenin end modifications see Ref. 84.

To quantify the stiffness of the DNA or more general any polymer, the so called worm-like chain (WLC) model is commonly applied [85]. Here the extensible worm-like chain model was fit to the measured data to determine the bending persistence

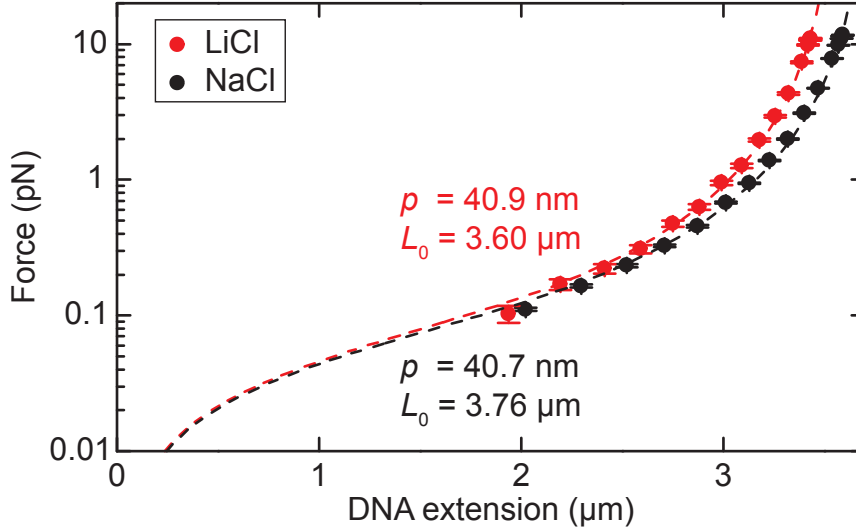


Figure 4.13. DNA force-extension characteristics for different counterions. The force-extension curves were recorded for the same molecule in solutions containing NaCl (black) and LiCl (red) as ionic salts. The DNA extension was determined at different applied forces at an NaCl or LiCl concentration of 990 mM in 10 mM TRIS-HCl at pH 8.0. To guarantee torsional freedom an 11.3 kbp DNA construct with single biotin- and digoxigenin attachments was used. Fits according to the worm-like chain model (Eq. 4.7) are shown as dashed lines, with the indicated values of the bending persistence length p and contour length L_0 .

length p as well as the contour length L_0 from the force-extension dependence [86]:

$$F(z) = \frac{k_B T}{p} \left[\frac{1}{4(1 - z/L_0)^2} - \frac{1}{4} + \left(\frac{z}{L_0}\right) + \sum_{i=2}^7 a_i \left(\frac{z}{L_0}\right)^i \right]. \quad (4.7)$$

The first three terms in the sum within the brackets correspond to the inextensible worm-like chain model [85]. The additional terms were proposed by Croquette and coworkers for the extensible WLC model [86] with coefficients $a_2 = -0.5164228$, $a_3 = -2.737418$, $a_4 = 16.07497$, $a_5 = -38.87607$, $a_6 = 39.49944$, and $a_7 = -14.17718$. Here $T = 24.9$ °C was used.

As one can see in Fig. 4.13, the DNA's bending persistence length p doesn't change within error between the different types of alkalis. However, the contour length L_0 , i.e. the length along the contour of the polymer in the absence of force, is reduced by 4% when changing the ionic environment from Na to Li. This might be due to a stronger binding of Li^+ to the DNA [83]: By screening the negative charge of the DNA more effectively, the distance between two consecutive base pairs might be reduced.

For comparison, in a buffer containing 10 mM phosphate buffer and 300 mM NaCl, a persistence length of 43.3 nm was measured. In the absence of NaCl a value of 47.9 nm was determined (data not shown).

4.6.2. DNA supercoiling for different alkaline counterions

Although no significant change of the bending mechanics of DNA was observed in solutions containing different alkaline electrolytes, there might still be an effect on the torsional properties of DNA. As shown before these properties can be probed by measuring the DNA's response to an induction of torque and since alter its length when being supercoiled. This has been discussed in detail for changes of the ionic strength and the force (see sections 3 and 4.3). Therefore also in this section torsion was induced into the DNA by means of magnetic tweezers. To allow supercoilability of the DNA molecules, the same DNA construct (~ 1.9 kbp) as employed in chapter 3 carrying multiple biotin and digoxigenin labels at the ends was used here.

The corresponding supercoiling curves of one DNA molecule in solutions containing 990 mM of LiCl, NaCl, or KCl at forces between 1 and 4 pN are shown in Fig. 4.14. One

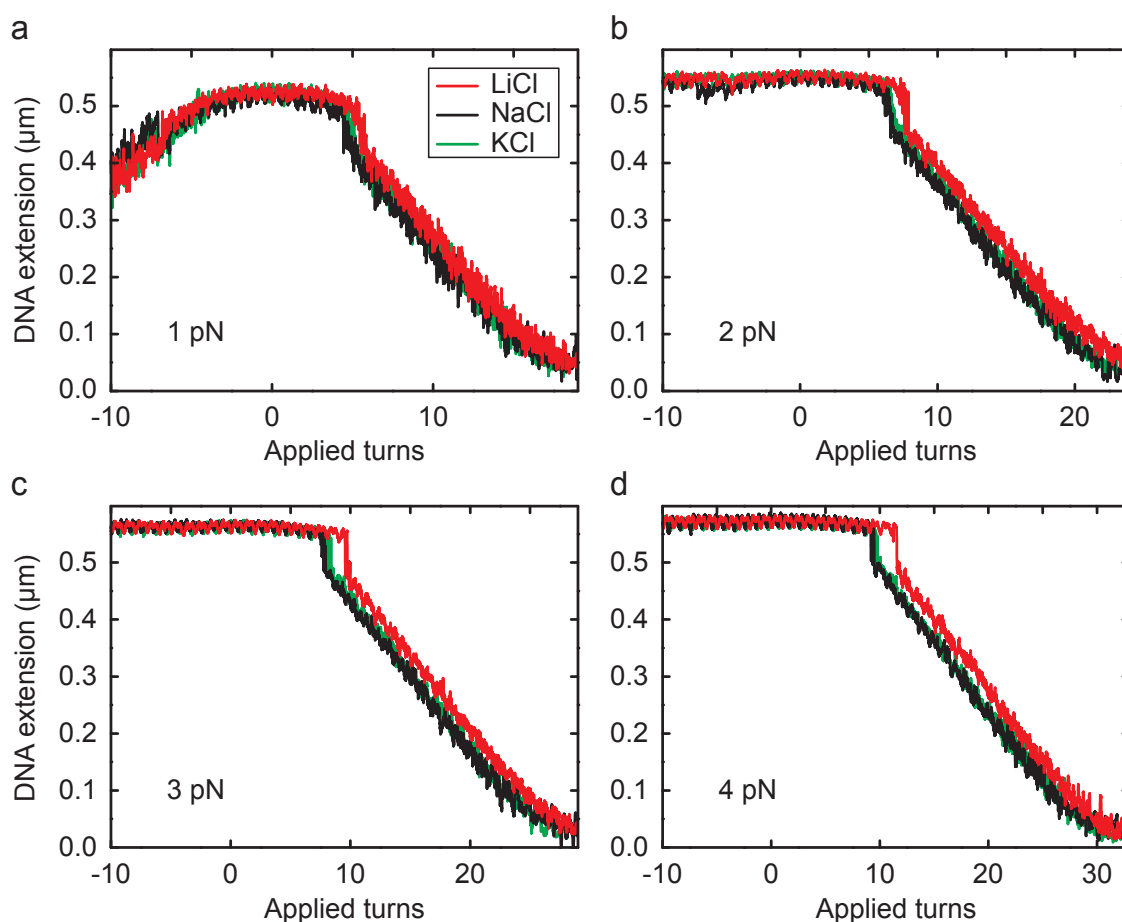


Figure 4.14. Dependence of DNA supercoiling on the type of counterion. The supercoiling curves were determined in the force range from 1 to 4 pN (a-d). An ~ 1.9 kbp long DNA molecule held at the indicated forces is continuously twisted with a frequency of 0.5 Hz and its length is recorded simultaneously. The buffer solution contained 990 mM of LiCl (red), NaCl (black), or KCl (green) in 10 mM TRIS-HCl at pH 8.0. Note that the scaling of the abscissa differs between the images in order to improve the visualization of the curves at each force value. Data were taken at 120 Hz and smoothed to 20 Hz.

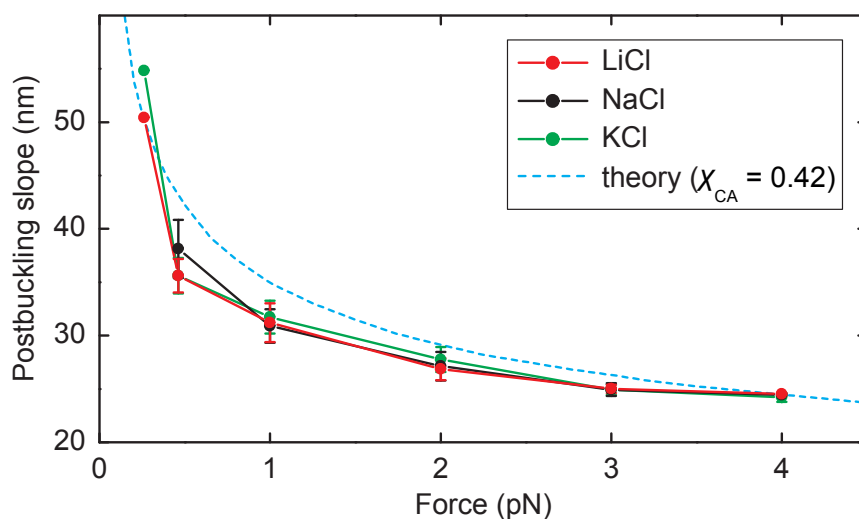


Figure 4.15. Force dependence of the supercoiling slopes for various alkaline salts. The mean value of the slopes was determined from linear fits of the length decrease after the buckling transition shown in Fig. 4.14 for three different molecules. The buffer solution contained 990 mM of LiCl (red), NaCl (black), or KCl (green) in 10 mM TRIS-HCl at pH 8.0. Error bars show the standard error (for the lowest force only a single molecule was analyzed). The dashed line represents the prediction from the theoretical model discussed earlier with a charge adaptation factor of 0.42.

can see that the curves for sodium and potassium chloride are almost superimposable for all measured forces (black and green graphs, respectively). However, the buckling transition, i.e. the onset of the formation of a plectonemic superhelix, occurs much later in the buffer containing LiCl (red curve). Nevertheless, a major change in the postbuckling slope cannot be observed.

To quantify the change of the supercoiling curves in the postbuckling phase for the different alkaline salts, a linear fit was applied to the slopes. The value of its slope corresponds to the amount of DNA consumed in each superhelical turn. If the screening of the electric charge of the DNA depends on the type of salt, this should alter the distance between the double strands in the superhelix and hence the slope in the postbuckling phase. The resulting dependence of the slope on the force for the different alkali metals is shown in Fig. 4.15. To improve the statistical relevance of the experiment, the postbuckling slope was obtained in experiments on three different molecules. Within error no systematic difference among the alkaline salts can be resolved with this technique. However, the model including 42% charge reduction of the DNA presented in section 4.2 reproduces the general trend of the force dependence of the postbuckling slope even for high ionic strengths.

Although there is no significant change in the in the postbuckling slopes either, the position of the buckling transition deviates significantly for experiments in solutions containing lithium chloride compared to sodium or potassium chloride (Fig. 4.14). This shift seems to be force dependent and more pronounced when the DNA is subjected to higher tension. Therefore characteristic parameters of the buckling transition at an applied force of 4 pN were studied in more detail as described in chapter 3.

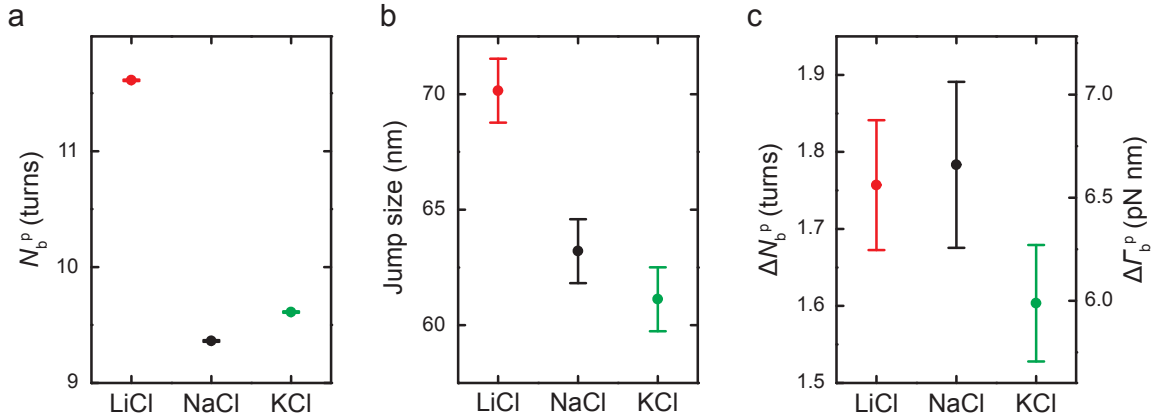


Figure 4.16. Dependence of the buckling transition on the type of counterion. The characteristic parameters describing the transition were determined at an ionic strength of 990 mM and an applied force of 4 pN for the ~ 1.9 kbp long DNA molecule shown in Fig. 4.14. (a) The buckling transition occurs much later (~ 2 turns) for LiCl than for NaCl and KCl. (b) Therefore also the corresponding length jump is $\sim 10\%$ larger for LiCl. (c) However, the amount of twist transferred into writhe during the transition as well as the corresponding torque remains constant within error. The parameters of the buckling transition were calculated as described in chapter 3. The standard error corresponds to the deviation of the fit to the occupancy of the postbuckling state with Eq. 3.11.

Fig. 4.16a shows the position of the buckling transition N_b^P for LiCl, NaCl, and KCl for the molecule shown in Fig. 4.14. For this particular DNA length (~ 1.9 kbp), approximately two additional turns have to be induced in the DNA to reach the buckling transition when changing from NaCl (and KCl) to LiCl.

Furthermore also the length change at the buckling transition increases by approximately 10% (Fig. 4.16b). Interestingly, the amount of twist which is transferred into writhe at the transition ΔN_b^P hardly changes (Fig. 4.16c). This value corresponds to the number of superhelical crossings (loops) that are formed at the transition. Taking into account that there's almost no change in the postbuckling slope for the different alkaline salts, this implies that the diameter of the end loop is much larger (i.e. its curvature is much smaller) for Li^+ than for Na^+ and K^+ .

As the bending rigidity hardly varies for the different types of alkaline counterions, the larger end loop for LiCl cannot be attributed to a larger DNA stiffness. Furthermore it was shown that at the buckling transition the end loop and ~ 0.7 turns of the superhelical plectoneme are formed. The simultaneous formation of both end loop and part of the superhelix was already observed at lower ionic strength (see chapter 3). However, the interaction between the two double strands in the superhelical plectoneme varies only slightly for different alkaline salts, i.e. approximately the same length of DNA is stored in the superhelix.

In conclusion, it seems that the effect of the size of the DNA only affects highly bent DNA structures. Prior to this work several models have been published postulating that such highly bent structures cannot be described accurately by means of a harmonic bending potential, which is used in the WLC model [87]. However, recent Monte

Carlo simulations of the DNA buckling transition revealed that the WLC model is well suited to describe DNA bending on length scales smaller than the persistence length [56].

Traditional models for polyelectrolyte-counterion interactions, such as Poisson-Boltzmann theory (see section 4.2), ignore relevant details, e.g. the discrete nature of charges on DNA, the type of cation, and ion-ion interactions [83]. The dependence of the stiffness in highly bent DNA structures on the type of counterion should be investigated further, for instance, by all atom molecular dynamics simulations and should be accounted for in the models used to describe the mechanics of DNA.

5. Internal friction of a migrating Holliday junction

5.1. Insights into the dynamics of branch migration

5.1.1. Dynamics of structural transitions in nucleic acids

In the molecular processes that have been described so far in this work, i.e. the formation of plectonemes and the interaction between DNA double-strands, mostly equilibrium quantities such as the buckling point and the effective charge density are determined and modeled. However, in vivo the supercoiled DNA structures are highly dynamic (see chapter 1), i.e. supercoils can be created, propagated and removed on a DNA molecule. Understanding the underlying principles is therefore of great interest [88]. Recently the dynamics of individual plectonemes has been visualized. The plectonemes were found to move along the DNA by diffusion or by a fast hopping process, in which the plectoneme vanishes at one position and reforms at a new spot along the DNA. For both processes only an upper bound on a millisecond time scale could be determined [89].

Friction between DNA double strands has been studied earlier with a combination of magnetic and optical tweezers [28]. In these experiments a nick was introduced in supercoiled DNA using a restriction enzyme. This enabled the DNA to reduce the torsion by swiveling around the nick, which caused the double strands to rotate around each other while the plectoneme was released. During the relaxation the extension of the DNA was recorded. The limited resolution of the instrument in combination with the type of experimental assay merely allowed the determination of an upper bound for the time-scale on which this process occurs. The major limitation of the experiment was that the friction between the double strands in the plectoneme is small compared to the viscous drag that the tethered bead experiences in the liquid environment.

In this chapter an alternative approach to study friction that occurs during refolding of a 4-arm junction of nucleic acids is presented. Similar to the plectonemic single molecule assay presented in chapter 4, the DNA structure used for this study has a significant twist-stretch coupling, i.e. a variation of the torsion stored in the molecule results in a length change. The underlying principle of the friction experiments is based on the translation of torsional fluctuations driven by thermal forces into length changes, which can be measured. To this end the DNA is torsionally constrained by means of magnetic tweezers. The thermal forces cause deflections of the DNA from its torsional equilibrium position resulting in a back-driving torque. Therefore the DNA acts like a torsional spring in this assay.

As these length changes due to the refolding occur on a nanometer length and a submillisecond time scale, a high spatio-temporal resolution is required to monitor this process. To achieve the sufficient resolution, the “conventional” magnetic tweezers

instrument has been optimized for stability and resolution as described in chapter 2. Apart from some remaining low frequency oscillations (<1 Hz), the instrument was shown to provide a resolution up to the limit which is set by the thermal noise of the probe.

5.1.2. Monitoring branch migration with magnetic tweezers

In section 2.3 it was shown how the lateral fluctuations of a tethered microsphere trapped with a magnetic tweezers instrument can be used to calculate the force that is acting on the tether in the axial direction. Similarly the fluctuations in the axial direction can be used to extract information about the stiffness of the tether. In addition it is possible to determine the time scale on which hydrogen bonds connecting the base pairs in a double strand DNA molecule are opened and closed due to thermal fluctuations from the variance in the axial direction. To this end a Holliday junction is used which serves as a torsional spring and couples torsional variations into longitudinal length changes (see Fig. 5.1a).

A Holliday junction is a four-arm junction of double strand DNA. It is a central intermediate of double strand break repair by homologous recombination in prokaryotes and eukaryotes [91] and transports crossovers between neighboring chromosome pairs over large distances. In this four-arm DNA junction the opposing arms may be homologous, i.e. possess identical sequences with respect to the junction center (Fig. 5.1b). In the absence of external constraints this junction is mobile. Thus, if one pair of

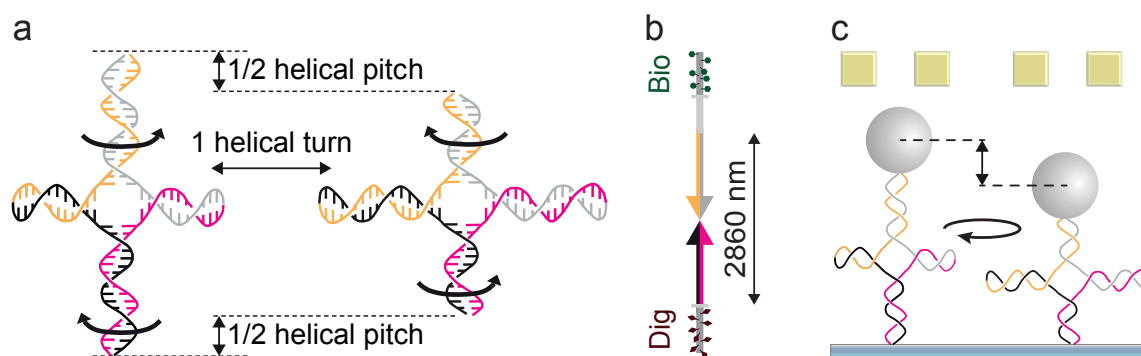


Figure 5.1. Branch migration of a Holliday junction. (a) Schematic representation of a Holliday junction (after Ref. 90 and modified). In the drawn four-arm DNA junction the opposing arms possess identical sequences with respect to the junction center. In the absence of external constraints the junction is mobile such that one pair of homologous arms can expand at the expense of the other. Since DNA has a helical structure, branch migration causes twisting of the arms with one turn per helical pitch moved. (b) To study branch migration with magnetic tweezers a DNA fragment was used which consisted of a 9.5 kbp long central piece, which included an 8.4 kbp long palindromic region and two handles with multiple biotin- and digoxigenin modifications. (c) Due to the twist stretch coupling which occurs during branch migration, a length variation of the side arms can be observed as an extension change once the DNA molecule is bound to a magnetic bead and stretched with magnetic tweezers.

opposing branches increases, the other pair will decrease, and vice versa. Since DNA has a helical structure, branch migration causes the arms to twist with one turn moved per helical pitch (of ~ 3.6 nm). Vice versa branch migration can directly be induced and controlled by adjusting the DNA twist (Fig. 5.1c) as demonstrated in recent single-molecule measurements using magnetic [90] and optical tweezers [92].

When the hydrogen bonds on opposite sides of the junction open simultaneously, the junction uses this liberated energy to form new bonds in the other two arms of the junction. Due to the twist stretch coupling such length changes, can, in principle, be detected with magnetic tweezers when torsionally constraining the DNA molecule between the substrate surface and a magnetic bead. However, the length changes are overlaid by the intrinsic fluctuations in the entire DNA molecule. Therefore the system has to be decoupled in order to distinguish the contribution of the fluctuation due to spontaneous branch migration from the overall fluctuations. This is done by modeling the system as consisting of two coupled springs of different stiffness (see section 5.2).

For the fluctuation measurements with magnetic tweezers a DNA construct with a total length of 9.5 kbp (without the handles necessary for binding to the substrate surface and the magnetic microsphere) has been designed (see Fig. 5.1b). The major part (8.4 kbp) of the DNA consisted of a palindromic sequence followed by a 1.1 kbp spacer region to the bead. For a detailed protocol of the preparation of the DNA construct see Appendix B.2.

To extrude the Holliday junction approximately 400 negative turns with respect

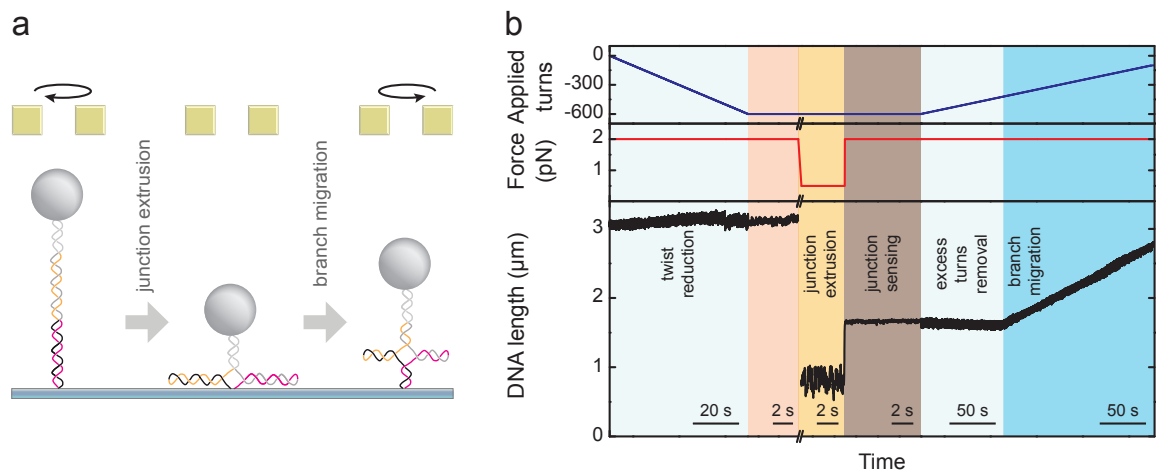


Figure 5.2. Extrusion of the Holliday junction in the magnetic tweezers. (a) Schematic representation of the procedure to extrude the Holliday junction from a linear DNA molecule with magnetic tweezers followed by induced branch migration. (b) Junction extrusion is seen as a DNA shortening that covers the full length of the repeat ($1.5 \mu\text{m}$). The onset of branch migration can be seen as a linear increase of the DNA length with the number of turns added (~ 3.5 nm/turn). The force applied during scanning corresponded to 2 pN. Data were acquired at 120 Hz. Note that the construct used here corresponds to the one described in chapter 6. For a more detailed description of the junction extrusion see the text.

to the helicity of the stretched double-strand DNA molecule are applied in a 1 mM phosphate buffer (Fig. 5.2). The trace shown in Fig. 5.2b was recorded for a slightly different construct used for the experiments described in chapter 6. The extrusion of the Holliday junction is favored in a buffer of low ionic strength due to the counterions screening the charge of the DNA and thus stabilizing the double helix. Subsequently the force is lowered to 0.5 pN to stimulate the spontaneous extrusion of the junction from the linear inverted repeat. At this force it is difficult to distinguish between the formation of the junction and supertwisting structures. Therefore the force is increased back to its original value, which is set high enough to avoid supertwisting structures. Junction extrusion is seen as a DNA shortening that covers the corresponding length of the repeat ($\sim 1.4 \mu\text{m}$). Over the whole range of this palindromic region branch migration can be induced by rotating the magnets above the sample. Even at the highest force that could be achieved in this assay (9.6 pN) branch migration could be driven over the entire palindromic sequence, which corresponds to 800 helical turns (data not shown).

5.2. Coupled displacement of DNA translation and migration

5.2.1. Calculating the range of the branch migration

Once a Holliday junction has been extruded it undergoes spontaneous branch migration, which is only driven by thermal forces. The objective of this study was to determine the characteristic parameters describing this process.

The coupling between the DNA extension change of the Holliday junction during spontaneous branch migration δz_{Hj} and the rotation change of the Holliday junction $\delta \vartheta_{\text{Hj}}$ is determined by the helical pitch of the DNA h_{DNA} at the given force:

$$\delta z_{\text{Hj}} = \frac{h_{\text{DNA}}}{2\pi} \cdot \delta \vartheta_{\text{Hj}}. \quad (5.1)$$

In the magnetic tweezers assay, the DNA is torsionally constrained due to the attachments of its ends to the substrate surface and the magnetic microsphere (Fig. 5.1c). This confinement causes a back-driving torque as soon as the DNA is moved out of its torsional equilibrium position during spontaneous branch migration. Thus, the DNA acts as a torsional spring with an effective spring constant for the movement of the Holliday junction in the z direction k_{Hj} that controls the branch migration. The mean torsional energy of the DNA E_{tor} (see Eq. 3.1) is given by the equipartition theorem (see section 2.3.1):

$$E_{\text{tor}} = \frac{1}{2} \frac{C_s}{L_0} \cdot \langle \delta \vartheta_{\text{Hj}}^2 \rangle = \frac{1}{2} k_{\text{B}} T = \frac{1}{2} k_{\text{Hj}} \langle \delta z_{\text{Hj}}^2 \rangle \quad (5.2)$$

where C_s denotes the force dependent effective DNA torsional modulus (see Eq. 3.2) and L_0 the contour length of the DNA. Therefore the root-mean-square rotation change of the Holliday junction during spontaneous branch migration is given by

$$\delta \vartheta_{\text{Hj rms}} = \sqrt{\frac{L_0}{C_s} \cdot k_{\text{B}} T}. \quad (5.3)$$

For a DNA length of 3230 nm and an effective torsional modulus of $95 k_B T$ nm (at a force of 9.6 pN) this relation yields that the root-mean-square rotation change of the Holliday junction during spontaneous branch migration corresponds to 0.93 helical turns.

The corresponding root-mean-square of the length change can be calculated by inserting Eq. 5.3 into Eq. 5.1:

$$\delta z_{\text{Hj rms}} = \frac{h_{\text{DNA}}}{2\pi} \sqrt{\frac{L_0}{C_s} \cdot k_B T}. \quad (5.4)$$

For the values given above and a helical pitch of 3.6 nm, this relation yields a length change of 3.3 nm.

Inserting Eq. 5.4 into Eq. 5.2 and rearranging allows then the derivation of the constant of the torsional spring which is loaded during spontaneous branch migration:

$$k_{\text{Hj}} = \left(\frac{2\pi}{h_{\text{DNA}}} \right)^2 \cdot \frac{C_s}{L_0} \quad (5.5)$$

which corresponds to 0.37 pN/nm for the values given above.

In the magnetic tweezers experiment, the DNA molecule is stretched by applying a force F . Therefore the spring describing the branch migration of the Holliday junction is extended by a distance Δz_{Hj} :

$$\Delta z_{\text{Hj}} = \frac{F}{k_{\text{Hj}}}. \quad (5.6)$$

Due to the twist-stretch coupling, this extension is translated into a rotational change $\Delta \vartheta_{\text{Hj}}$ according to Eq. 5.1:

$$\Delta \vartheta_{\text{Hj}} = F \cdot \frac{h_{\text{DNA}}}{2\pi} \cdot \frac{L_0}{C_s}. \quad (5.7)$$

This effect has also been described previously [92] and results in a negative offset between the rotations of the permanent magnets and the number of turns that are actually stored in the DNA. At a force of 9.6 pN, this offset is 7.3 turns.

5.2.2. Power spectral density of a coupled system

The spontaneous branch migration is thought to occur in one base-pair steps possibly on a sub-millisecond time scale. Therefore even with the improvements that were made to the conventional magnetic tweezers instrument the steps cannot be resolved directly. However, as already discussed in section 2.3.2, the frequency spectrum of the fluctuations can be analyzed to extract additional information.

In a typical experiment, the length of the extruded arms is small relative to the overall extension. Hence the system can be modeled by three coupled springs (Fig. 5.3a). The upper spring represents the part of the DNA molecule between the magnetic microsphere and the Holliday junction, while the lower spring describes the length fluctuations of the DNA between the junction and the substrate surface. The spring

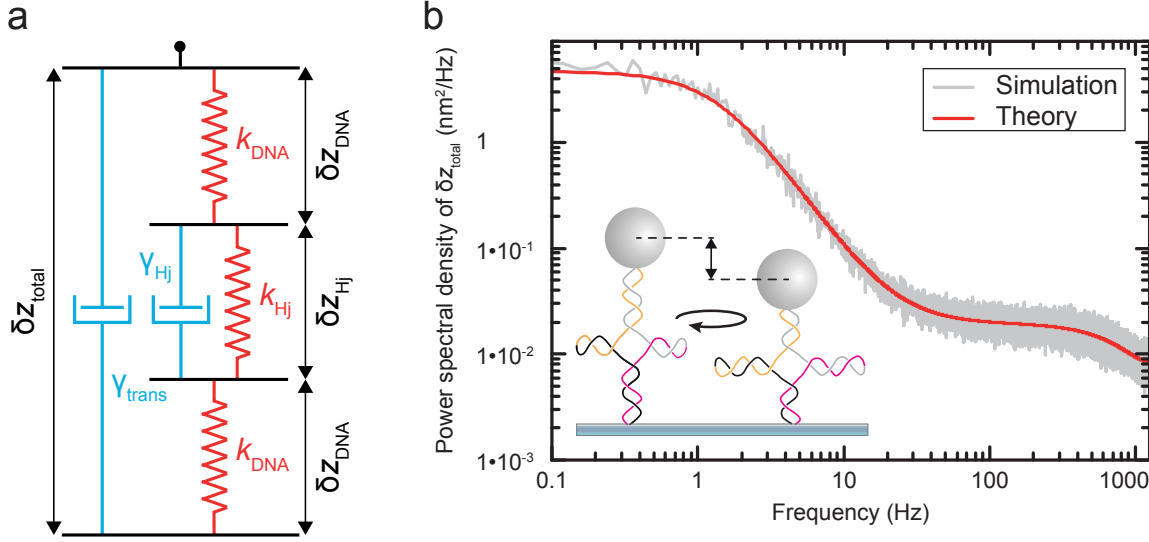


Figure 5.3. Modeling branch migration as a system of coupled springs. (a) Model used for the description of the branch migration with basic mechanical elements (after Ref. 93 and modified). The drag is modeled by a dashpot because the force scales linearly with velocity. The stiffness is expected to be constant in the range of movement and is modeled by a spring, for which the force linearly depends on the displacement. The mass is neglected since the system is overdamped (see section 2.3.2). (b) Power spectrum of the result of a Brownian dynamics simulation of the spontaneous branch migration (gray curve). The simulated time is 1000 s. The algorithm used for the simulations was written by Ralf Seidel. A fit with Eq. 5.13 (red line) allows to quantitatively determine the stepping rate and thus the friction of the branch migration process. The RMS and the cutoff frequency of the spontaneous branch migration determined with this fit deviate 0.3% and 7.4% from the simulation parameters, respectively.

in the center with constant k_{Hj} accounts for the fluctuations of the DNA due to spontaneous branch migration. The system can be simplified by combining the upper and the lower spring by a single one with constant k_{DNA} because for both springs the dynamics of the length fluctuations are dominated by the microsphere. The following Langevin equation in the axial direction then describes the motion of the magnetic microsphere (Eq. 2.4):

$$-\gamma_{\text{trans}}\delta\dot{z}_{\text{total}} - k_{\text{DNA}}\delta z_{\text{DNA}} = F_{\text{trans}}(t) \quad (5.8)$$

where $F_{\text{trans}}(t)$ defines the thermal force acting on the microsphere. γ_{trans} corresponds to the translational drag coefficient that a spherical particle experiences when moving in a viscous environment according to Eq. 2.10. An additional correction term that arises due to the close proximity of the bead to the substrate surface can be included for the calculation of the drag coefficient as described in Ref. 93.

The Holliday junction is a second “friction element” at which the random forces are acting. This contribution can be incorporated into a second linear Langevin equation:

$$-\gamma_{Hj}\delta\dot{z}_{Hj} - k_{Hj}\delta z_{Hj} + k_{DNA}\delta z_{DNA} = F_{Hj}(t). \quad (5.9)$$

Here γ_{Hj} is the friction coefficient limiting the migration of the junction. The thermal force driving this process is represented by $F_{\text{Hj}}(t)$.

The DNA extension change of the non-branched region that contributes to these fluctuations δz_{DNA} corresponds to the difference between the total DNA extension change δz_{total} and the DNA extension change of the Holliday junction during spontaneous branch migration δz_{Hj} :

$$\delta z_{\text{DNA}} = \delta z_{\text{total}} - \delta z_{\text{Hj}}. \quad (5.10)$$

Using Eq. 5.10 allows to reformulate equations Eqs. 5.8 and 5.9 in terms of δz_{total} and δz_{Hj} , such that a set of coupled, linear Langevin equations is obtained:

$$F_{\text{trans}}(t) = -\gamma_{\text{trans}}\delta\dot{z}_{\text{total}} - k_{\text{DNA}}(\delta z_{\text{total}} - \delta z_{\text{Hj}}) \quad (5.11)$$

$$F_{\text{Hj}}(t) = -\gamma_{\text{Hj}}\delta\dot{z}_{\text{Hj}} - k_{\text{Hj}}\delta z_{\text{Hj}} + k_{\text{DNA}}(\delta z_{\text{total}} - \delta z_{\text{Hj}}). \quad (5.12)$$

For this coupled system the power spectral density $Z_c(f)$ can be determined [93, 94] and is given by the sum of two Lorentzians with two characteristic frequencies f_{\pm}^{coupl} :

$$Z_c(f) = \frac{4k_{\text{B}}T}{1 + C^2\gamma_{\text{trans}}\gamma_{\text{Hj}}} \cdot \left\{ \frac{\gamma_{\text{Hj}}C^2}{(2\pi f_+^{\text{coupl}})^2 + (2\pi f)^2} + \frac{1}{\gamma_{\text{trans}} \left[(2\pi f_-^{\text{coupl}})^2 + (2\pi f)^2 \right]} \right\} \quad (5.13)$$

with

$$C = \left(2\pi f_-^{\text{coupl}} - \frac{k_{\text{DNA}} + k_{\text{Hj}}}{\gamma_{\text{Hj}}} \right) k_{\text{DNA}}^{-1} \quad (5.14)$$

and

$$f_{\pm}^{\text{coupl}} = \frac{k_{\text{DNA}} + k_{\text{Hj}}}{4\pi\gamma_{\text{Hj}}} + \frac{k_{\text{DNA}}}{4\pi\gamma_{\text{trans}}} \pm \frac{1}{4\pi} \sqrt{\left(\frac{k_{\text{DNA}} + k_{\text{Hj}}}{\gamma_{\text{Hj}}} + \frac{k_{\text{DNA}}}{\gamma_{\text{trans}}} \right)^2 - \frac{4k_{\text{DNA}}k_{\text{Hj}}}{\gamma_{\text{trans}}\gamma_{\text{Hj}}}}. \quad (5.15)$$

By fitting a measured PSD with Eq. 5.15, one should obtain the trap stiffnesses as well as the drag coefficients for both the DNA bending fluctuations and the fluctuations due to the spontaneous branch migration. The mean square displacements are related to the corresponding trap stiffnesses by the equipartition theorem (section 2.3.2), such that

$$\langle \delta z_{\text{total}}^2 \rangle = k_{\text{B}}T \left(\frac{1}{k_{\text{DNA}}} + \frac{1}{k_{\text{Hj}}} \right) \quad \text{and} \quad \langle \delta z_{\text{Hj}}^2 \rangle = \frac{k_{\text{B}}T}{k_{\text{Hj}}}. \quad (5.16)$$

To test the theoretical description, the spontaneous branch migration was modeled by Brownian dynamics simulations.* Apart from the branch migration the model considers the elastic coupling of DNA bending fluctuations as well as rotations of the magnetic microsphere. The power spectrum of the simulated time trace of 1000 s at a force of 9.6 pN and a DNA extension of 2.75 μm is shown in Fig. 5.3b. A fit with Eq. 5.13 well describes the data resulting from the simulations over the entire frequency range.

*The algorithm for the Brownian dynamics simulations was written by Ralf Seidel.

5.2.3. Determination of the time per spontaneous migration step

Once the friction coefficient γ_{Hj} describing the spontaneous branch migration is determined (see section 5.2.2), a diffusion coefficient D_{Hj} can be calculated from the Einstein relation describing the random walk of the spontaneous branch migration at the Holliday junction:

$$D_{\text{Hj}} = \frac{k_{\text{B}}T}{\gamma_{\text{Hj}}}. \quad (5.17)$$

The mean-square displacement $\langle \delta z_{\text{Hj}}^2 \rangle$ of the random branch migration is then given by [39]:

$$\langle \delta z_{\text{Hj}}^2 \rangle = 2D_{\text{Hj}}t. \quad (5.18)$$

In addition the mean-square displacement of a random walk can be calculated from the distance of a single migration step Δ_{Hj} and the number of branch migration steps n :

$$\langle \delta z_{\text{Hj}}^2 \rangle = n \cdot \Delta_{\text{Hj}}^2. \quad (5.19)$$

The number of steps in return is defined as the total time t divided by the average time per branch migration step t_{step} :

$$n = \frac{t}{t_{\text{step}}}. \quad (5.20)$$

Inserting Eq. 5.20 into Eq. 5.19 yields:

$$\langle \delta z_{\text{Hj}}^2 \rangle = \frac{t}{t_{\text{step}}} \cdot \Delta_{\text{Hj}}^2. \quad (5.21)$$

Comparing Eqs. 5.21 and 5.18 provides:

$$D_{\text{Hj}} = \frac{\Delta_{\text{Hj}}^2}{2t_{\text{step}}}. \quad (5.22)$$

Reformulating this expression and inserting Eq. 5.17 allows to calculate the mean time for a single step from the friction coefficient:

$$t_{\text{step}} = \frac{\Delta_{\text{Hj}}^2}{2D_{\text{Hj}}} = \frac{\Delta_{\text{Hj}}^2 \gamma_{\text{Hj}}}{2k_{\text{B}}T}. \quad (5.23)$$

The results from the magnetic tweezers experiments are presented in the following section.

5.3. Experimental determination of the friction coefficient

After developing a theoretical background the characteristic parameters describing the spontaneous branch migration can be inferred from the results of the magnetic tweezers measurements. The advantage of the Holliday junction assay presented in section 5.1.2 is that the same molecule can be used both for the migration and the

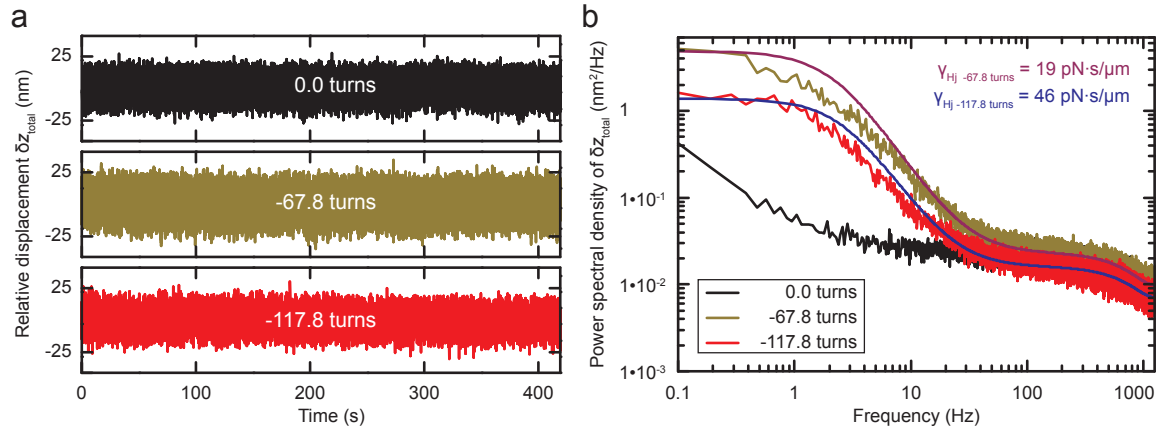


Figure 5.4. Branch migration for different amounts of applied turns. (a) The length variation of the DNA molecule for no (*top*), -67.8 (*middle*), and -117.8 (*bottom*) induced turns was recorded with 2500 Hz at a force of 9.6 pN in a 10 mM phosphate buffer containing 300 mM NaCl at pH 7.4. The total root-mean-square displacement varies only slightly between the traces, because the contribution of branch migration is small compared to the one from the DNA bending fluctuations alone. (b) The power spectral densities of the trajectories shown follow the shape of two coupled Lorentzians for the experiments with induced Holliday junction. Fits of the corresponding power spectral densities with Eq. 5.13 (purple and blue lines for -67.8 and -117.8 induced turns, respectively) allow the quantitative determination of the stepping rate (273 and 652 μs per 1 bp step, respectively) and of the friction of the branch migration process (values given in the figure). The data recorded at -67.8 turns (olive) are shifted upwards due to a larger mean square displacement of the microsphere. The control experiment without an extruded Holliday junction (black) shows the influence of some residual low frequency oscillations. See also section 2.2.2 for a possible explanation of this effect.

control experiments. In the torsionally relaxed state, i.e. prior to the application of turns with the permanent magnets, no Holliday junction is present and thus no branch migration can occur. A time trajectory over several minutes corresponding to a torsionally relaxed DNA molecule without Holliday junction is shown in Fig. 5.4a (top). The power spectral density has the typical Lorentzian shape of a tethered particle (black curve in Fig. 5.4b) as predicted by the theory (see section 2.3.2). The increase of the PSD towards lower frequencies corresponds to the influence of some residual low frequency oscillations, whose origin remains unknown (see section 2.2.2).

Once the Holliday junction was extruded (see section 5.1.2), the number of induced turns was increased from approximately -400 to -117.8 turns. The helical pitch depends on the applied force and was determined from a linear fit of the extension versus applied turns curve during branch migration similar to the one shown in Fig. 5.2b. At a force of 9.6 pN it corresponds to approximately 3.6 nm. Hence, inducing 117.8 turns reduces the DNA length by approximately 420 nm. For the spontaneous branch migration experiments enough turns have to be induced such that the junction is stably extruded (and is not released by spontaneous fluctuations). Alternatively an excess of turns changes the length too much such that a comparison to the control

measurement is no longer meaningful.

The time trajectory of the DNA length at -117.8 and -67.8 turns are shown in Fig. 5.4a (bottom and middle, respectively). The length fluctuations can be characterized in terms of the total root-mean-square displacement. The RMS for -117.8 and the control measurement is 4.4 nm and differ only by 0.1%. This is reasonable because the expected contribution of the fluctuations from the spontaneous branch migration (3.3 nm, see section 5.2.1) is much lower than the one from the bending fluctuations. For -67.8 induced turns the RMS is slightly larger (5.9 nm). This might originate from an increased bending flexibility due to a formed kink at the Holliday junction.

The corresponding power spectral densities are depicted in Fig. 5.4b. Both curves of the experiments with induced Holliday junction follow the predicted shape of two coupled Lorentzians (see section 5.2.2). Each curve shows two distinct plateaus followed by two cutoff frequencies. The higher plateau and the smaller cutoff frequency correspond to the fluctuations caused by the spontaneous branch migration. The bending fluctuations of the DNA result in the lower plateau and the higher cutoff frequency. As their contribution is not expected to change once the Holliday junction is extruded, the lower plateaus of the experiments performed at no and -117.8 turns coincide.

A fit with Eq. 5.13 allows the determination of the cutoff frequencies as well as the mean-square displacements for both regions of the PSD. The curve with -117.8 induced turns (which provides a better coincidence with the control at high frequencies) yields a root-mean-square displacement caused by the fluctuations of the spontaneous branch migration of the Holliday junction of 2.3 nm. Fitting the curve corresponding to -67.8 induced turns results in an RMS of 4.0 nm for the Holliday junction migration. Both values are on the same order of magnitude as the value calculated based on the assumption that the junction is confined in a simple harmonic potential (3.3 nm, see section 5.2.1).

Furthermore the friction coefficients describing the spontaneous branch migration can be calculated from the cutoff frequencies of the two curves. The values for -117.8 and -67.8 induced turns are $46 \text{ pN} \cdot \text{s}/\mu\text{m}$ and $19 \text{ pN} \cdot \text{s}/\mu\text{m}$, respectively. According to Eq. 5.17 this corresponds to diffusion coefficients of $766 \text{ bp}^2/\text{s}$ and $1830 \text{ bp}^2/\text{s}$ (for -117.8 and -67.8 turns, respectively). With Eq. 5.23 the friction coefficient can be directly converted into the mean time the Holliday junction waits before taking a 1 bp step. These values are $652 \mu\text{s}$ and $273 \mu\text{s}$.

To see if the rate of the branch migration can be influenced by external parameters, fluctuations of the DNA were recorded for different ionic strengths. The stability of the experimental assay allowed the exchange of the buffer solution in the sample chamber and thus the performance of experiments for different salt concentrations on one and the same molecule. The control experiment without an extruded Holliday junction shows hardly any difference if the NaCl concentration is decreased from 300 to 0 mM (Fig. 5.5a). The ionic strength influences mechanical properties of the DNA, such as its persistence length. Therefore the overall extension increases by approximately 2% when reducing the salt concentration. However, the fluctuations in the axial direction should not be affected greatly by this change.

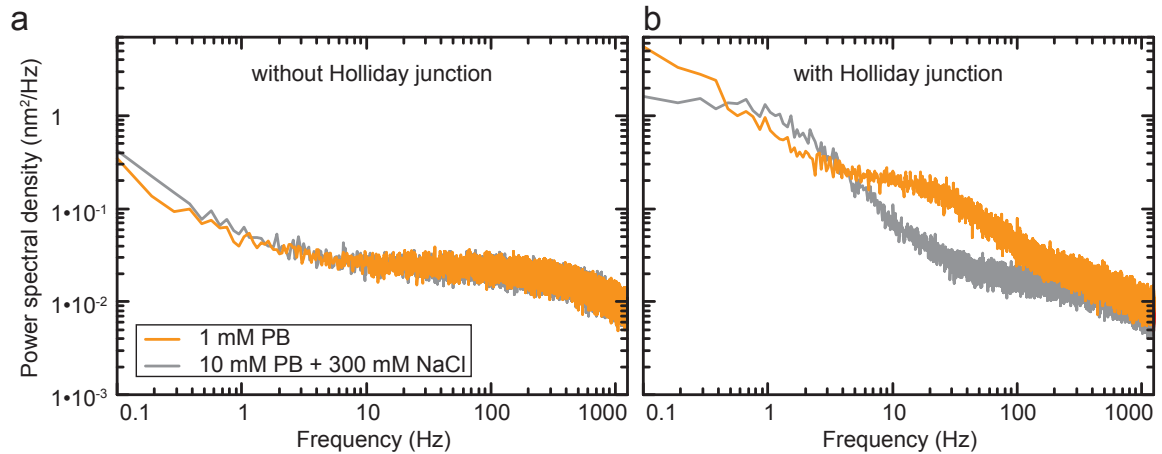


Figure 5.5. Salt dependence of the branch migration. Power spectral densities of the axial length fluctuations in solutions of different ionic strength for (a) no and (b) -117.8 induced turns. While the PSD does not change significantly when no Holliday junction is extruded, it varies greatly once branch migration is allowed. A decreased ion concentration destabilizes the migration process, thus producing a PSD differing from the characteristic shape of a coupled Lorentzian. Data were recorded with 2500 Hz at a force of 9.6 pN.

The branch migration process consists of the spontaneous formation and breaking of hydrogen bonds connecting the base pairs. As salt is known to stabilize the double helix of the DNA, one expects that the fluctuations at the Holliday junction should occur more frequently. Indeed a PSD deviating from the one at moderate ionic strength was found in the experiment (Fig.5.5b). However, as its shape differs from that of a coupled Lorentzian function, a quantification of the effect with the model presented here does yield ambiguous results.

5.4. Intramolecular friction in other single molecule assays

To verify the model presented in this chapter an alternative experiment was performed which allowed to determine the friction coefficient directly from the time trajectories recorded with magnetic tweezers. After the extrusion of the Holliday junction in the magnetic tweezers assay the torsional confinement of the DNA was removed by the induction of a nick in one of the phosphate backbones. To this end the sample chamber was illuminated by a 488 nm laser (for the description of the instrument see section 6.2). Such illumination has been reported to induce photodamage in biomolecules by increasing the formation of oxygen radicals [95]. In case of DNA these radicals are able to break the bonds in the phosphate backbones. Once a nick is induced in one of the phosphate backbones the DNA molecule is able to release the induced torsion by swiveling around the nick. Due to the twist-stretch coupling that occurs during branch migration, a reduction of twist causes a length change which can be detected in the magnetic tweezers assay.

In the nicking experiments, regimes could be identified where the speed at which the branch migration occurs upon the release of torsion is constant (data not shown).

Although the spread of the values of the friction coefficient determined with this assay was relatively large (10 to 50 pN · s/ μ m), the values determined from the axial fluctuations of the DNA (19-46 pN · s/ μ m) are within this range.

The reason for the different values of the friction coefficient determined from the spontaneous branch migration might be a possible sequence dependence. The base pairs formed by adenine (A) and thymine (T) are connected by two while the ones formed by guanine (G) and cytosine (C) are linked by three hydrogen bonds. Therefore the pairing energy that must be overcome during branch migration depends on the sequence of base pairs. When -67.8 turns were induced in the DNA, the region enclosing 5 base pairs upstream and 5 base pairs downstream of the center of the Holliday junction had a G-C content of 50%. At -117.8 induced turns this content is 40%. This might explain the larger friction coefficient at -117.8 turns. However, additional experiments for various numbers of induced turns should be performed to verify this hypothesis.

The increasing root-mean-square displacement at -67.8 turns compared to the control measurement might also be due to a higher flexibility of the DNA once the Holliday junction is extruded. This flexibility might depend on the DNA length, which would explain the decreased RMS at -117.8 induced turns.

Furthermore a more elaborate model should account for the fact that branch migration is not a continuous process. As the migration causes the rupture and formation of bonds between individual base pairs at the Holliday junction, it should be modeled by a series of discrete steps.

Friction has also been reported to occur in other biomolecules. For instance, the friction that kinesin motors experience when moving on microtubule could be measured with an optical tweezers assay [96]. Compared to the friction coefficient found for DNA branch migration, the one corresponding to the protein movement is by 5 orders of magnitude smaller.

In the experiments shown in Ref. 28, a time of approximately 50 μ s was estimated for the removal of one supercoil upon spontaneous torsional relaxation. This is much shorter than the mean time that it takes the Holliday junction to migrate a distance corresponding to 1 bp which is on the order of several 100 μ s. The underlying processes in branch migration and supercoil dynamics are, of course, fundamentally different, however, it shows that PSD analysis is well suited for the characterization of the intramolecular friction that occurs upon refolding of nucleic acids, and potentially for the understanding of similar dynamic phenomena in proteins.

6. Using DNA as a nanomechanical gear

6.1. Characterization of inhomogeneous illumination fields

The characterization of three-dimensional inhomogeneous illumination fields is a challenge in modern microscopy. Based on the Holliday junction assay presented in the previous chapter a DNA construct was developed which could be used as a nanomechanical translation stage to move a single fluorescent quantum dot through an exponentially decaying evanescent field. The objective of the project presented in this chapter was to record the emission of the quantum dot within the evanescent field as well as under homogeneous illumination. This allows to directly obtain the intensity distribution of the excitation field without additional deconvolution.

The technique presented here is of particular interest because nowadays several techniques combining single molecule manipulation assays and fluorescence microscopy have been published. The first example of a combined optical tweezers apparatus and a fluorescence microscope has been reported already more than a decade ago [97]. This led the way to several other hybrid techniques, in particular in combination with atomic force microscopy (AFM) [98] and magnetic tweezers [7]. Recently such a hybrid instrument has been used to show the diffusion of fluorescently labeled plectonemes along DNA [89].

In parallel to the development of hybrid instruments, the past two decades have boosted a broad range of techniques in modern fluorescence microscopy that use sophisticated illumination schemes and geometries. This includes confocal techniques such as fluorescence correlation spectroscopy [99], two-photon laser scanning fluorescence microscopy [100], and super-resolution stimulated emission depletion [101] microscopy. In addition, in widefield microscopy the use of inhomogeneous illumination profiles has gained increasing popularity and promoted the development as well as the application of total internal reflection fluorescence (TIRF) microscopy [102–104], fluorescence interference contrast microscopy [105, 106], surface plasmon assisted optics [107], super-resolution microscopy using layered metallic structures [108], and structured illumination microscopy [109, 110]. The unifying principle of such excitation schemes is a narrowed excitation volume in one or more dimensions to increase the signal-to-noise ratio by orders of magnitudes and in part to even bypass the Abbe/Rayleigh-limit for the spatial resolution.

When applying non-homogeneous illumination often knowledge about the exact shape of the applied illumination profile is essential, e.g. for quantitative data analysis [99, 111], 3D image reconstructions in microscopy [101, 110], and absolute distance measurements [106, 112]. The characterization of excitation profiles in all three dimensions is up to now still a challenging task when using microscopy, in particular for the axial direction. It is mainly limited by the fact that the measured intensity I_m emitted from a probe results from a convolution of its emitted signal $I_{em}(x, y, z)$

with the three-dimensional point-spread function (PSF) of the optical measurement system [111, 113]. Typically one can assume proportionality between $I_{em}(x, y, z)$ and the excitation intensity $I_{ex}(x, y, z)$ at a given position. Using the fluorescent object function $F_{obj}(x, y, z)$ as proportionality factor, which describes the distribution of fluorescent molecules in the object, their extinction coefficients, and quantum efficiencies, one obtains:

$$\begin{aligned} I_m &= I_{em} \otimes PSF \\ &= [I_{ex} \cdot F_{obj}] \otimes PSF. \end{aligned} \quad (6.1)$$

To extract the distribution of the excitation light from the measured intensity requires therefore a deconvolution of Eq. 6.1, which, for example, has been applied previously to characterize evanescent fields [113, 114]. This demands precise knowledge of the fluorescent object function and most problematic of the PSF , which is an intrinsic characteristic of each experimental setup. In particular the PSF variation along the optical axis is difficult to obtain, since it arises from a combination of an effective reduction of the numerical aperture for image planes that are out of focus [111] and a decreased near-field coupling of the emission light into the glass substrate [115].

To circumvent an elaborate deconvolution one can, however, use a single point-like light source, such as a small fluorescent molecule or a quantum dot, instead of an extended fluorescent object. In this case $F_{obj}(x, y, z)$ becomes proportional to a delta-function such that also the measured intensity becomes proportional to the product of the excitation intensity and the PSF at the position of the light source

$$I_m \sim I_{ex} \cdot PSF. \quad (6.2)$$

For conventional widefield (CW), i.e. for a homogeneous illumination, the measured intensity of a point-like light source becomes even directly proportional to the PSF of the optical system

$$I_m^{CW} \sim PSF. \quad (6.3)$$

Combining Eqs. 6.2 and 6.3 for an inhomogeneous and a homogeneous excitation field one obtains

$$I_m \sim I_{ex} \cdot I_m^{CW} \iff I_{ex} \sim \frac{I_m}{I_m^{CW}}. \quad (6.4)$$

Thus, the relative distribution of the inhomogeneous illumination can be obtained by scanning the excitation volume with the point-like light source and recording its intensity under inhomogeneous as well as conventional widefield illumination. The deconvolution is then readily obtained via the ratio of both intensities.

This conceptually simple approach is experimentally difficult to realize, since the emitter has to be attached to an external translation stage for scanning the illumination field. Previously this was realized by using an atomic force microscope to linearly translate a fluorescent quantum dot that had been attached to the tip of the silicon nitride cantilever of the device [98, 116]. The attachment of the fluorescent probe to a solid-state surface, however, is itself problematic, because it influences both

the distribution of the excitation light as well as the emission from the probe by introducing an additional large boundary with differing optical properties.

Here a new method is introduced to linearly translate a single point-like light source in free solution, i.e. practically in the absence of a disturbing interface, in order to probe the intensity distribution of an inhomogeneous illumination in axial direction. The DNA-based device used here is based on the assay described in chapter 5 and includes as a central piece a Holliday junction. Additionally a fluorescent probe is attached to the DNA. The Holliday junction now allows to use the DNA itself as a linear translation stage with nanometer precision. Due to its composition and size, double-strand DNA represents a minimal disturbance. It negligibly scatters and absorbs visible light [117] and does not significantly quench the emission from a

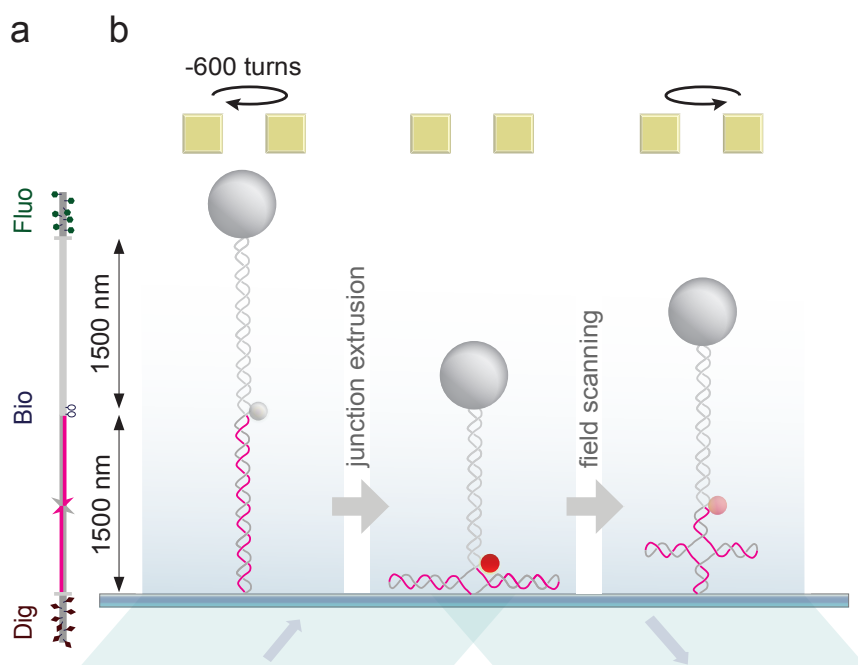


Figure 6.1. Scanning evanescent fields using a nanomechanical DNA gear. (a) Used DNA construct consisting of an ~ 600 bp long fluorescein labeled tail (Fluo) followed by a 4.5 kbp spacer region, a 4.4 kbp inverted repeat (orientation of the two 2.2 kbp regions with identical sequence indicated by the arrows), and an ~ 600 bp long digoxigenin labeled tail (Dig). Two internal biotin modifications (Bio) are introduced upstream of the inverted repeat. A detailed procedure for the preparation of the construct is given in section B.3. (b, left) A streptavidin conjugated quantum dot is bound to the internal label of the DNA and stretched in a magnetic tweezers instrument. (b, middle) After inducing 600 negative turns in the DNA, a Holliday junction is spontaneously extruded where the branches cover the full length of the inverted repeat (Fig. 5.2). (b, right) Adding sufficient positive turns drives branch migration of the junction and the quantum dot is lifted from its position proximal to the surface upwards by about the length of the helical pitch per turn. Monitoring the emission of the quantum dot with an EMCCD camera during branch migration allows thus the scanning of the excitation field distribution in axial direction, e.g. of an evanescent field resulting from TIRF illumination as shown here.

nearby emitter by energy transfer [118]. As a proof of principle, this method is used to scan the evanescent fields resulting from sample illumination in TIRF geometry with a quantum dot as a point-like light source (Fig. 6.1).

6.2. Components of the biological nano translation stage

This single-molecule branch migration assay was adapted to build a translation stage for a fluorescent probe. An 8.9 kbp (3000 nm) linear DNA molecule was constructed (see Appendix B.3 for a detailed preparation procedure of the DNA construct) of

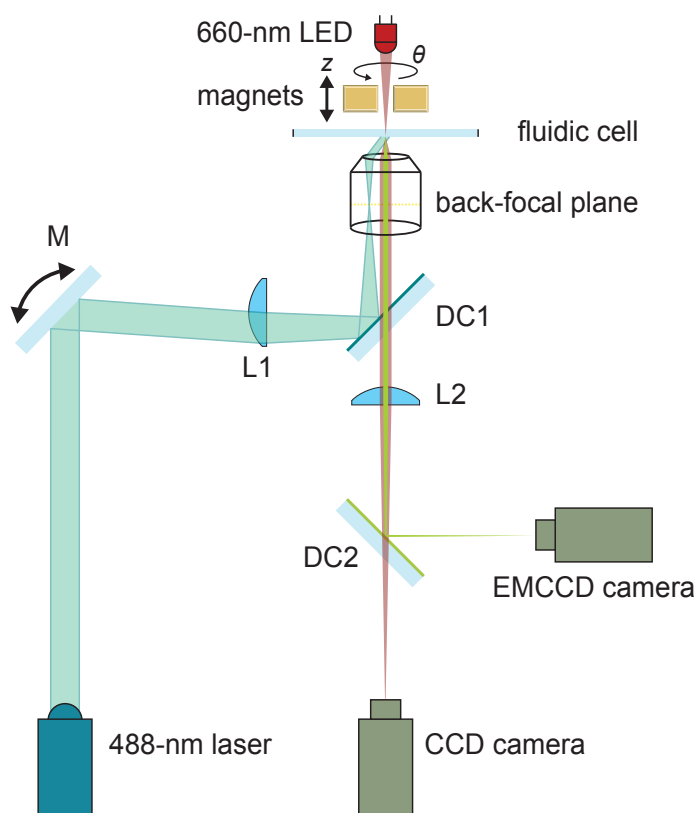


Figure 6.2. Instrument combining magnetic tweezers and TIRF microscopy. Fluorescence excitation is performed by a 488 nm laser. The beam is focused into the back-focal plane of the high numerical aperture objective by lens L1. By tilting of mirror M, which is placed on a gimbal mount and located in the back-focal plane of L1, the beam can be laterally displaced from the optical axis of the objective such that it emerges under an angle at the sample position. Fluorescence emission from the sample passes through the dichroic mirror DC1, is reflected by the dichroic mirror DC2 and is focused by L2 on an EMCCD camera. As illumination for the imaging of the magnetic beads, the emission light from a 660 nm LED is focused onto the fluidic sample cell. The beam passes DC1 and DC2 and is focused by L2 onto the chip of a CCD camera. Above the fluidic cell a pair of permanent magnets can be translated vertically to generate different stretching forces on the DNA construct and rotated for twisting. A more detailed description of the instrument is given in Ref. 32.

which the initial 4.4 kbp (1500 nm) are composed of two 2.2 kbp long fragments of identical sequence that are arranged in an inverted orientation to each other in order to form a long palindrome (6.1a). From the center of this palindromic region a Holliday junction can be extruded by applying external twist (see below) [119]. The remaining 4.5 kbp stretch that serves as a spacer is labeled internally 7 bp (2.4 nm) upstream of the inverted repeat with two biotin molecules that are 11 bp apart. The biotin modifications serve as attachment sites for the fluorescent probe for which a streptavidin-coated quantum dot (Qdot 625, Invitrogen) was used. The 8.9 kbp molecule carries two additional ~ 600 bp fragments at its ends that comprise either multiple digoxigenin- (for the end at the repeat region) or fluorescein-labeled bases (for the other end).

To scan evanescent fields the DNA construct was incubated with an excess of quantum dots and subsequently with $1\ \mu\text{m}$ anti-fluorescein coated magnetic beads (MyOne, Invitrogen) in order to allow their binding to the biotin and fluorescein modifications of the molecule, respectively. The construct was flushed into the fluidic cell of a magnetic tweezers apparatus (see section 2.1), in which the digoxigenin-labeled DNA end was allowed to attach to the anti-digoxigenin coated bottom. A pair of permanent magnets (W-05-N50-G, Supermagnete) was used to generate a force on the magnetic bead and to stretch the DNA construct (6.1b, left). The length of the DNA, i.e. the vertical position of the magnetic bead with respect to a non-magnetic reference bead attached to the surface of the fluidic cell, was determined from videoimages using a Pulnix TM-6710CL CCD camera and real-time 3D particle tracking with sub-nm accuracy [35, 93]. The magnetic tweezers instrument was additionally equipped with a sensitive EMCCD camera (iXon DU897-COO-BV, Andor Technology) for fluorescence detection and a 488 nm laser (Sapphire 488-50, Coherent) that allowed illumination of the sample both in conventional widefield and TIRF geometry through the high numerical aperture objective of the instrument (Nikon, CFI Apo TIRF 100x, NA = 1.49) (Fig. 6.2).*

6.3. Determination of the angle of incidence

The numerical aperture NA of an objective is defined as

$$NA = n \cdot \sin \theta_{\max} \quad (6.5)$$

where n is the index of refraction of the immersion oil and θ_{\max} is the half-angle of the maximum cone of light that can enter or exit the objective. The numerical aperture is related to the ratio of the focal length f_{obj} and the diameter of the exit pupil D through:

$$NA = \frac{D}{2f_{\text{obj}}}. \quad (6.6)$$

This equation holds if the entire objective is illuminated.

*Friedrich W. Schwarz assembled and designed the instrument combining magnetic tweezers and single-molecule TIRF microscopy and performed an initial experiment with the quantum dot-DNA assay. A detailed description of the instrument is given in Ref. 32.

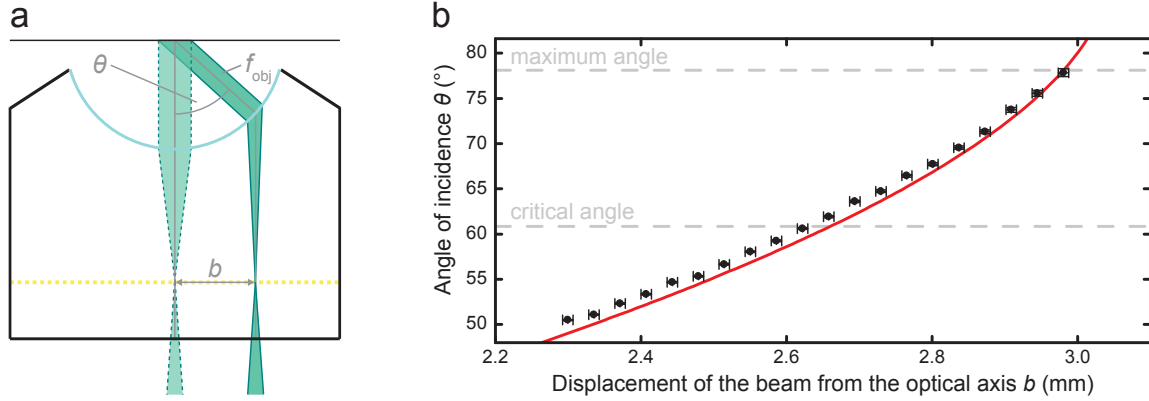


Figure 6.3. Determination of the angle of incidence. (a) Schematic representation of the beam geometry within the objective. If the incident beam is displaced by a distance b from the optical axis, the light emerges from the objective under an angle θ . The focal length of the objective is denoted by f_{obj} , the position of the back-focal plane by a yellow dashed line. (b) Measured dependence of the angle of incidence on the displacement of the beam from the optical axis (black squares). The red line is the theoretical prediction according to Eq. 6.7.

If the beam entering the objective does not fill the entire width of the objective and is focused on the backfocal plane, the beam emerging from the objective will consist of parallel rays. Displacing the beam from the optical axis by a distance b causes the light to emerge from the objective under an angle of incidence θ (Fig. 6.3a). The maximal displacement of the beam is limited by the exit pupil at which $b_{\text{max}} = D/2$. Inserting Eq. 6.5 into Eq. 6.6 and solving for θ yields the angle of incidence at b_{max} and in more general also the dependence of the angle of incidence for any displacement of the beam from the optical axis:

$$\theta(b) = \arcsin \frac{b}{n \cdot f_{\text{obj}}}. \quad (6.7)$$

The prediction of this dependence is shown in Fig. 6.3b for an objective with $NA = 1.49$ and 2 mm focal length and an immersion oil with an index of refraction of 1.5229 at 488 nm.

In the experiments the beam displacement from the optical axis was adjusted with a micrometer screw to set a particular angle of incidence. The micrometer screw was calibrated to provide defined angles of incidence at particular screw positions using an isosceles triangular prism as previously described [113]. The obtained angles of incidence from the calibration procedure reproduced the theoretically predicted dependence on the beam displacement (Fig. 6.3b).

6.4. Scanning evanescent fields using a pointlike light source

The considerable anisotropy of the used magnetic beads [93] allows to twist the DNA molecule by rotating the magnet configuration (see chapters 3 and 4). To start an

experiment first approximately 600 negative turns with respect to the helicity of the DNA were applied at a force of ~ 3 pN (Fig. 6.1b, left). Subsequently, the force was lowered in order to stimulate the spontaneous extrusion of the Holliday junction from the linear inverted repeat [119]. Junction extrusion is seen as a DNA shortening that covers the full length of the repeat at elevated force (Figs. 5.2 and 6.1b, middle). In this configuration the quantum dot is in close proximity to the surface of the fluidic cell.

Then positive turns were added slowly at 2 Hz while simultaneously recording DNA

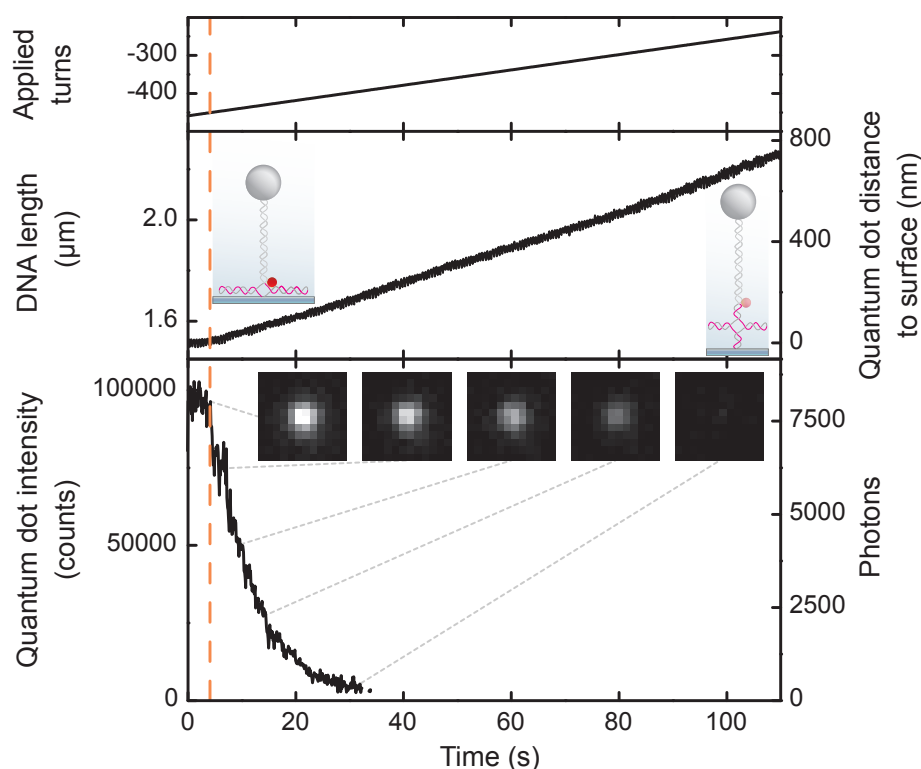


Figure 6.4. Linear translation of a quantum dot through an evanescent field.

The quantum dot moves due to the induced branch migration of the Holliday junction. The evanescent field was generated by illuminating the sample in TIRF geometry. Shown are the time courses of applied turns, DNA length and detected fluorescence emission intensity of the quantum dot. After extrusion of the Holliday junction (see Fig. 6.1), where the quantum dot is in a proximal position to the surface (see sketch), positive turns were added to the DNA at a rate of 2 Hz. As soon as excess turns are removed (marked by a vertical dashed line, see text), branch migration occurs which is seen as a DNA length increase with ~ 3.5 nm per turn and a simultaneous decrease of the quantum dot emission. Snapshot images of the quantum dot are shown for selected times indicated by the dotted lines. As the spacing between the magnetic bead and the quantum dot remains unchanged, the distance of the quantum dot to the surface can be calculated from the DNA length by subtracting an offset of ~ 1.5 μm . The DNA length was measured at a frequency of 120 Hz, fluorescence images were acquired at 10 Hz. A constant force of 3 pN was applied throughout the experiment. The angle of incidence is 70.5° . All measurements were performed at room temperature in 0.1% Tween 20, 100 $\mu\text{g}/\text{ml}$ BSA, and 1 mM DTT in 10 mM phosphate buffer pH 7.4.

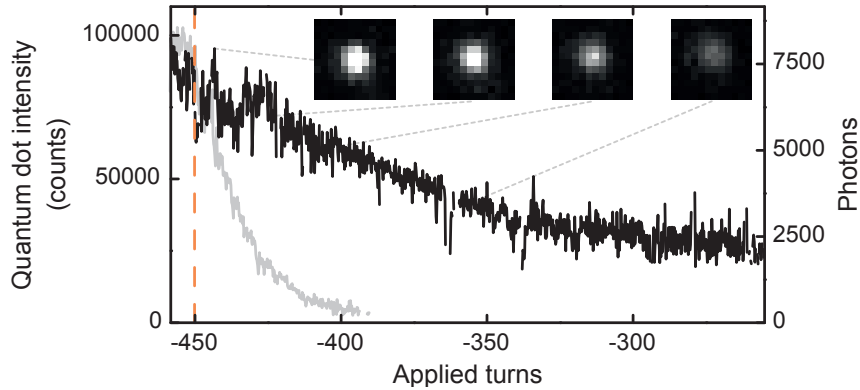


Figure 6.5. Intensity decay measured for conventional widefield illumination. Experimental conditions are as in Fig. 6.4. The change in intensity is due to the change of the point spread function when the quantum dot moves out of focus. The signal recorded in TIRF illumination (from Fig. 6.4) is depicted in gray. The onset of branch migration is indicated by the vertical dashed line.

length and fluorescent images of the quantum dot under TIRF illumination at 120 Hz and 10 Hz, respectively (Fig. 6.4). The objective was positioned such that its focus in the fluorescence channel coincided with the bottom of the fluidic cell. First the excess of negative turns was removed while the DNA length remained constant, since only ~ 420 turns can be stored in the arms of the Holliday junction according to the number of base pairs forming the inverted repeat. Subsequently, the onset of branch migration (indicated by the dashed line in Fig. 6.4) could be seen as a linear increase of the DNA length with the number of turns added. The DNA lengthening caused also the quantum dot to decrease its emission (Fig. 6.4) because it moves together with the magnetic bead away from the surface and thus out of the illumination field (Fig. 6.1c). As the average distance between the magnetic bead and the quantum dot remains unchanged throughout the measurement, the distance change of the quantum dot to the substrate surface can be directly calculated from the length change of the DNA (Fig. 6.4). Fitting the DNA extension versus added turns with a linear relation provides a slope of 3.5 nm. This is slightly less than the actual helical pitch, since the DNA is only extended to 92% of its full contour length at a force of 3 pN due to thermal fluctuations. These fast fluctuations cause also the quantum dot to fluctuate around its average axial position with a root-mean-square displacement of ~ 2.5 nm for a surface distance of 100 nm at 3 pN force [93]. Nonetheless, it shows that the Holliday junction allows to linearly couple macroscopic rotations into translation on the nanometer scale, where the DNA pitch even serves as an intrinsic ruler. The effects of incomplete stretching can be easily compensated by using the well characterized force-extension behavior of DNA [86].

To quantitatively evaluate the detected fluorescence emission, the images of the quantum dot were fit with a symmetric two-dimensional Gaussian function whose volume provides the detected intensity. While it remains almost constant before branch migration it decreases exponentially with the quantum dot distance from the substrate (Fig. 6.4).

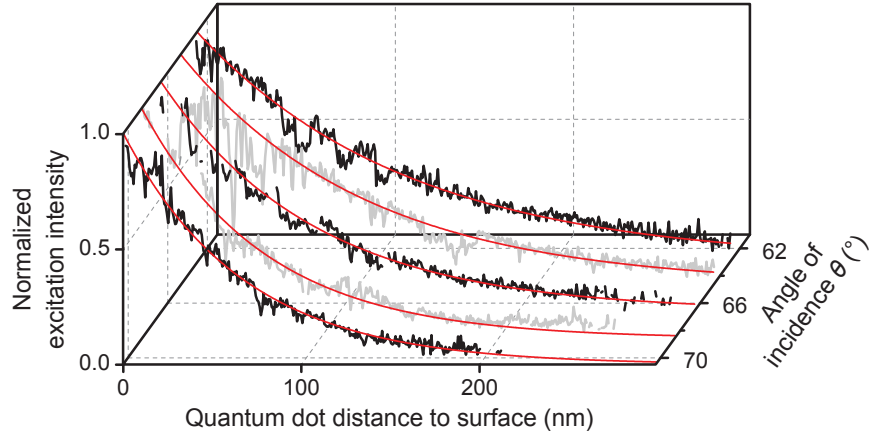


Figure 6.6. Excitation intensity profiles for various angles of incidence. The measured dependence of the normalized intensity profiles in TIRF illumination on the angle of incidence of the laser are shown in black and gray. Data was obtained as described in the text by correcting the measured intensity profiles in TIRF illumination for the variation of the point spread function. Red lines are fits to the data with a single exponential function according to Eq. 6.9. Periods of occasional, sudden intensity drops due to quantum dot blinking were removed from the profiles.

The measured intensity decay with distance, does not directly reflect the intensity distribution of the evanescent field. This is due to the changing *PSF* when the quantum dot moves out of focus. As detailed above, the intensity decay of the evanescent field can, however, be obtained by dividing the recorded signal in TIRF illumination by the one recorded in conventional widefield illumination, since a quantum dot is a point-like light source. The signal recorded in conventional widefield illumination is shown in Fig. 6.5. The intensity decay with distance is much smaller than the one recorded in TIRF illumination, indicating that the correction due to the changing *PSF* is relatively small.

One finally obtain the normalized axial intensity distribution of the evanescent field $\bar{I}_{\text{ex}}(z)$ from the ratio of the intensities measured for TIRF $\bar{I}_{\text{m}}(z)$ and conventional widefield illumination $\bar{I}_{\text{m}}^{\text{CW}}(z)$ that were previously normalized by the corresponding intensities obtained for the proximal position of the quantum dot to the surface $I_{\text{m}}(0)$ and $I_{\text{m}}^{\text{CW}}(0)$:

$$\bar{I}_{\text{ex}}(z) = \frac{I_{\text{m}}(z)/I_{\text{m}}(0)}{I_{\text{m}}^{\text{CW}}(z)/I_{\text{m}}^{\text{CW}}(0)} = \frac{\bar{I}_{\text{m}}(z)}{\bar{I}_{\text{m}}^{\text{CW}}(z)}. \quad (6.8)$$

For noise reduction the widefield data was smoothed to 1 Hz prior division. Fig. 6.6 shows the obtained normalized intensity profiles of the evanescent field recorded for the same quantum dot at different angles of incidence θ of the laser, which were adjusted by displacing the laser beam from the optical axis of the objective (Fig. 6.3). As expected, as the angle of incidence increases, the evanescent field becomes shallower.

For each angle of incidence the excitation intensity profile can be well fitted by a

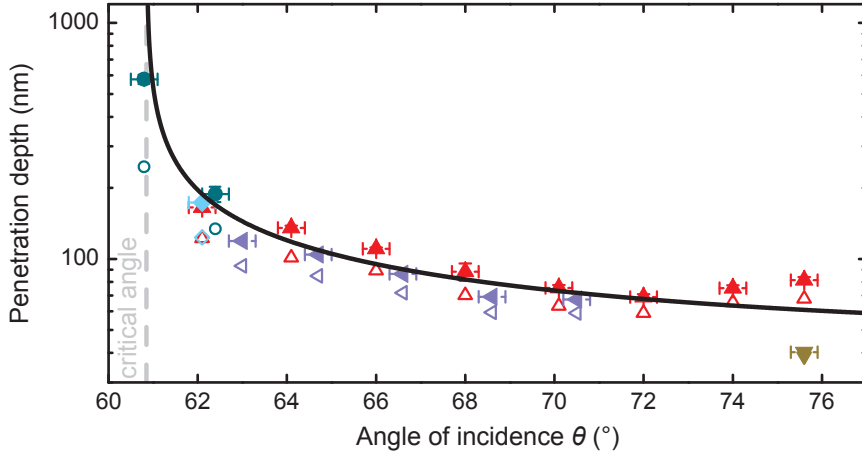


Figure 6.7. Dependence of the penetration depth on the angle of incidence. The filled symbols indicate the penetration depth, i.e. the mean length of the exponential intensity decay of the evanescent excitation field, for the given angles of incidence. Each color-symbol combination corresponds to data taken for an individual quantum dot-DNA construct. Open symbols represent the corresponding decay lengths of the measured, i.e. uncorrected, intensity profiles, which are shown for comparison. The theoretically expected dependence of the penetration depth according to 6.10 is shown as a solid black line, the critical angle for total internal reflection as a gray dashed line.

single exponential function (red lines in Fig. 6.6):

$$\bar{I}_{\text{ex}}(z, \theta) = \exp\left[-\frac{z}{d(\theta)}\right], \quad (6.9)$$

from which the penetration depth $d(\theta)$ of the evanescent field is obtained. The dependence of the penetration depth on the angle of incidence is shown in Fig. 6.7 (filled symbols). Experiments for different DNA molecules demonstrate the reproducibility of the measurements. The theoretical dependence of the penetration depth on the angle of incidence according to classical electrodynamics is given by [120, 121]:

$$d(\theta) = \frac{\lambda}{4\pi\sqrt{n_1^2\sin^2\theta - n_2^2}} \quad (6.10)$$

where λ is the wavelength of the incident light and $n_1 > n_2$ are the indices of refraction of the media at the interface where the light is totally internally reflected. As an oil immersion objective was used, n_1 corresponds to the index of refraction of the immersion oil (Immersionol 518F immersion oil, Zeiss) with $n_1 = 1.5229$ at 488 nm, and n_2 to the index of refraction of the buffer ($n_2 = 1.33$). Using these values the theoretical dependence of the penetration depth on the angle of incidence reproduces well the experimentally obtained values (filled symbols in Fig. 6.7).

The slight increase of the measured penetration depth at larger angles can be attributed to the fact that optical aberrations become more important close to the maximum angle of incidence, which is 78° as calculated from the numerical aperture of the objective. Fitting the uncorrected measured intensity profiles (as shown in

Fig. 6.4) with an exponential relation results in decay lengths (open symbols in Fig 6.7) that are only slightly smaller than the experimentally obtained and the theoretical predicted penetration depths.

The determination of illumination profiles with the method presented here does not require additional knowledge of the optical properties of the microscope, because the deconvolution correction is directly obtained from recordings in conventional widefield illumination. It is therefore potentially less error-prone compared to the deconvolution of microscopy images of extended objects. For example, field distributions for TIRF illumination following a double exponential dependency have been obtained from imaging 9 μm -sized fluorescent beads [114], while other studies reported a single exponential relation [98, 113] in agreement with the results from this work and the prediction from classical electrodynamics [120]. Recently, an alternative, deconvolution-free technique that allows to determine absolute intensity distributions of laser foci has been introduced. It is not microscopy-based and relies on ionic current measurements through a nanopore [122]. This technique is, however, limited to rather large laser powers and confocal setups, while the present measurements have been obtained at excitation intensities, which are typically used for detection of single-molecule fluorescence.

Beyond characterizing the electromagnetic field distribution in a TIRF microscope which is important for various applications [98, 112], this method should be a versatile tool to experimentally characterize other intensity distributions, e.g. near metal surfaces [107], metallic multilayers [108], and in structured illumination microscopy [109]. Mounting the fluidic cell on an XY -nanopositioning system will enable the three-dimensional scanning of intensity distributions. This measurement scheme can also be used to experimentally determine the three-dimensional PSF of an optical system as function of distance from the typically present glass interface, which can currently only be obtained from theoretical calculations [111].

In addition, this technique will allow to directly investigate the distance-dependent near-field coupling between two optically active probes, e.g. fluorescence resonance energy transfer (FRET) between a fluorescent donor and an acceptor molecule [123] or the near-field enhancement of the emission of a fluorophore near a gold nanoparticle [124]. The probes can be conveniently attached below and above the Holliday junction using the here applied internal labeling method [125]. The distance between the two probes can then be changed continuously by branch migration while the emission is recorded simultaneously. Therefore this nanomechanical DNA gear will become a versatile tool for anchoring and moving small optically active probes with minimal optical interference.

7. Conclusion

The genome inside the cell is constantly subjected to force and torque. While torsion causes supercoiling of the DNA, the tension can change the distribution of the supercoils in terms of twist and writhe. A large variety of biological processes crucially depend on the degree of supercoiling and may even change it by inducing or removing additional turns. This work focused both on the understanding of some mechanical aspects related to twisted DNA under tension as well as the dynamics during a refolding process of the DNA. To this end a variety of experiments has been performed, in which force and torque were applied to single DNA molecules with a magnetic tweezers instrument.

As a first example, the buckling transition that stretched DNA undergoes upon overwinding was studied and found to depend on the applied force as well as the ionic strength of the solution. Generally, the extent of the buckling allows the measurement of the energetic differences of bent, kinked, or other structured DNA compared to non-kinked DNA. Since one role of chromatin is to serve as a torsional buffer, it is of interest to see whether nucleosome positioning sequences [126] support pinning of the plectoneme position or whether plectoneme formation is independent of the sequence of base pairs. Furthermore it has been shown recently that after the formation of a superhelix plectonemes are able to diffuse along the DNA [89]. Therefore it might be of interest to understand how this plectoneme diffusion is affected by a kink in the DNA. Such a kink can also be modeled in Monte Carlo simulations as shown in Ref. 56. The ability to detect a single kink on a DNA molecule can potentially be used to observe enzymes that kink or bend DNA upon binding to it.

By combining single-molecule experiments, theoretical considerations, coarse-grained and all-atom simulations, it was shown that within a cylinder approximation, DNA-DNA interactions can only be described by a significantly reduced DNA charge. Furthermore, a theory that accurately describes DNA supercoils over a broad range of tension and ionic strength was provided. Supercoiling under tension is a unique way to confine and align two DNA molecules into close proximity to each other in absence of interfering surfaces [63]. In contrast to previous topological investigations of long DNA [61, 67, 68], the force-based experiments shown in this work allow a more reliable quantification of DNA-DNA interactions since much smaller distances are achieved. The surprisingly small DNA-DNA interactions result from a complex interplay of a highly charged and structured molecule with solvent molecules and ions.

The simple effective interaction potential will be an important contribution for quantitative models of complex biomolecular systems which cannot be treated with atomic detail such as DNA packaging in chromatin and viruses. Possibly also protein-DNA interactions could be modeled with higher precision. The findings reveal that particular caution is necessary when applying effective charge parameters obtained from experiments that probe a different physics, such as electrophoresis [69], resulting

from a complex interplay between hydrodynamics and electrostatics [63, 64, 127].

Varying the type of monovalent counterion in the solution surrounding the DNA does not influence its bending mechanics. However, the torsional modulus is affected by such a change as the buckling transition occurs earlier and more pronounced for smaller alkali metals. While the bending persistence length primarily depends on the charge and the amount of counterions, the torsional mechanics is affected additionally by the actual size of the individual counterions [83].

In addition several improvements were made to the magnetic tweezers instrument in order to increase the stability and the spatio-temporal resolution. In a review which was published this year, Bryant et al. stated that the current resolution limits of magnetic tweezers corresponded to the unwinding of 3 bp at a time resolution of ~ 1 s [8]. Unwinding of a single base pair would cause a change of the DNA length of 1.1 nm. In this work it has been shown that with the improved magnetic tweezers instrument DNA extension changes as small as 0.5 nm can be resolved unambiguously at a time resolution of 1 s.

Furthermore a major part of the noise contributing to the detected signal is due to the fact that the bead is anchored by a DNA tether. To increase the resolution even more, a more rigid attachment of the DNA to the magnetic bead and the substrate surface could be utilized. Instead of bond-formation between a single double strand and the surface of the microsphere and the substrate, ends with multiple attachment points such as multi-helix DNA origami structures could be used [128]. Besides the stability these multi-helix structures could be used for the supercoiling experiments, for which DNA constructs with multiple attachment sites are required. The labeled DNA handles that were used in this work cause a high DNA curvature at the binding region to the substrate and the bead, which might influence the overall DNA mechanics, especially for shorter DNA constructs.

The increased resolution of the magnetic tweezers instrument allowed then the study of a dynamic process that twisted DNA undergoes under tension. This is of particular interest since DNA supercoiling *in vivo* is a dynamic process, in which supercoils can be formed, propagated and removed. These processes depend on the molecular friction in the nucleic acid. The intramolecular friction that occurs when supercoils are removed, however, is much lower than the drag of a micrometer-sized bead [28], which is used as a typical probe in magnetic tweezers experiments. Hence a considerable effort has been made to study a similar type of intramolecular friction that arises upon unfolding and refolding of DNA double strands. Such a process occurs during spontaneous branch migration of a Holliday junction. By means of power-spectral-density analysis of the length fluctuations the overall dynamics of the branch migration process could clearly be resolved. Theoretical modeling considering the elastic coupling of DNA bending fluctuations and the junction movement allowed the quantitative determination of the stepping rate and thus the friction of the branch migration process. This method will be widely applicable to study local-scale molecular friction in biological systems.

Apart from studying intramolecular friction, the Holliday junction assay also allowed to drive the branch migration by rotating a pair of permanent magnets above the sample. Hence the DNA served as a nanomechanical gear, which was then used as a linear nanometer-precise translation stage for a small fluorescent probe to axially scan

intensity distributions of the evanescent field in a TIRF microscope. Using DNA as a carrier for a fluorescent probe provided minimal optical interference. In addition the DNA helical pitch served as an intrinsic ruler by coupling one macroscopic rotation to about 3.5 nm linear translation. This nanomechanical DNA gear will allow the characterization of a broad range of inhomogeneous illumination fields and to study near-field effects between small optical probes.

Bibliography

- [1] J. Vinograd, J. Lebowitz, R. Radloff, R. Watson and P. Laipis, *The twisted circular form of polyoma viral DNA.*, Proc Natl Acad Sci U S A **53**(5), 1104–1111 (1965)
- [2] T. J. Richmond and C. A. Davey, *The structure of DNA in the nucleosome core.*, Nature **423**(6936), 145–150 (2003)
- [3] J. D. Watson and F. H. Crick, *Molecular structure of nucleic acids; a structure for deoxyribose nucleic acid.*, Nature **171**(4356), 737–738 (1953)
- [4] L. Baranello, D. Levens, A. Gupta and F. Kouzine, *The importance of being supercoiled: How DNA mechanics regulate dynamic processes.*, Biochim Biophys Acta **1819**(7), 632–638 (2012)
- [5] B. J. Peter, J. Arsuaga, A. M. Breier, A. B. Khodursky, P. O. Brown and N. R. Cozzarelli, *Genomic transcriptional response to loss of chromosomal supercoiling in Escherichia coli.*, Genome Biol **5**(11), R87 (2004)
- [6] J. J. Champoux, *DNA topoisomerases: structure, function, and mechanism.*, Annu Rev Biochem **70**, 369–413 (2001)
- [7] J. Gore, Z. Bryant, M. D. Stone, M. N. Nollmann, N. R. Cozzarelli and C. Bustamante, *Mechanochemical analysis of DNA gyrase using rotor bead tracking.*, Nature **439**(7072), 100–104 (2006)
- [8] Z. Bryant, F. C. Oberstrass and A. Basu, *Recent developments in single-molecule DNA mechanics.*, Curr Opin Struct Biol **22**(3), 304–312 (2012)
- [9] D. A. Koster, A. Crut, S. Shuman, M.-A. Bjornsti and N. H. Dekker, *Cellular strategies for regulating DNA supercoiling: a single-molecule perspective.*, Cell **142**(4), 519–530 (2010)
- [10] E. L. Zechiedrich and N. R. Cozzarelli, *Roles of topoisomerase IV and DNA gyrase in DNA unlinking during replication in Escherichia coli.*, Genes Dev **9**(22), 2859–2869 (1995)
- [11] S. V. Komen, G. Petukhova, S. Sigurdsson, S. Stratton and P. Sung, *Superhelicity-driven homologous DNA pairing by yeast recombination factors Rad51 and Rad54.*, Mol Cell **6**(3), 563–572 (2000)
- [12] T. L. R. Tan, R. Kanaar and C. Wyman, *Rad54, a jack of all trades in homologous recombination.*, DNA Repair (Amst) **2**(7), 787–794 (2003)

- [13] A. Vologodskii and N. R. Cozzarelli, *Effect of supercoiling on the juxtaposition and relative orientation of DNA sites.*, *Biophys J* **70**(6), 2548–2556 (1996)
- [14] R. Kanaar and N. R. Cozzarelli, *Roles of supercoiled DNA structure in DNA transactions*, *Curr Opin Struct Biol* **2**(3), 369–379 (1992)
- [15] C. F. Kuo, A. H. Zou, M. Jayaram, E. Getzoff and R. Harshey, *DNA-protein complexes during attachment-site synapsis in Mu DNA transposition.*, *EMBO J* **10**(6), 1585–1591 (1991)
- [16] Z. Wang and R. M. Harshey, *Crucial role for DNA supercoiling in Mu transposition: a kinetic study.*, *Proc Natl Acad Sci U S A* **91**(2), 699–703 (1994)
- [17] K. Luger, A. W. Mäder, R. K. Richmond, D. F. Sargent and T. J. Richmond, *Crystal structure of the nucleosome core particle at 2.8 Å resolution.*, *Nature* **389**(6648), 251–260 (1997)
- [18] A. Bancaud, N. C. E. Silva, M. Barbi, G. Wagner, J. F. Allemand, J. Mozziconacci, C. Lavelle, V. Croquette, J. M. Victor, A. Prunell and J. L. Viovy, *Structural plasticity of single chromatin fibers revealed by torsional manipulation.*, *Nat Struct Mol Biol* **13**(5), 444–450 (2006)
- [19] N. Rovinskiy, A. A. Agbleke, O. Chesnokova, Z. Pang and N. P. Higgins, *Rates of gyrase supercoiling and transcription elongation control supercoil density in a bacterial chromosome.*, *PLoS Genet* **8**(8), e1002845 (2012)
- [20] T. R. Strick, J. F. Allemand, D. Bensimon, A. Bensimon and V. Croquette, *The elasticity of a single supercoiled DNA molecule.*, *Science* **271**(5257), 1835–1837 (1996)
- [21] T. R. Strick, V. Croquette and D. Bensimon, *Homologous pairing in stretched supercoiled DNA.*, *Proc Natl Acad Sci U S A* **95**(18), 10579–10583 (1998)
- [22] J. F. Allemand, D. Bensimon, R. Lavery and V. Croquette, *Stretched and overwound DNA forms a pauling-like structure with exposed bases.*, *Proc Natl Acad Sci U S A* **95**(24), 14152–14157 (1998)
- [23] Z. Bryant, M. D. Stone, J. Gore, S. B. Smith, N. R. Cozzarelli and C. Bustamante, *Structural transitions and elasticity from torque measurements on DNA.*, *Nature* **424**(6946), 338–341 (2003)
- [24] T. Lionnet, A. Dawid, S. Bigot, F.-X. Barre, O. A. Saleh, F. Heslot, J.-F. Allemand, D. Bensimon and V. Croquette, *DNA mechanics as a tool to probe helicase and translocase activity.*, *Nucleic Acids Res* **34**(15), 4232–4244 (2006)
- [25] J. Gore, Z. Bryant, M. Nöllmann, M. U. Le, N. R. Cozzarelli and C. Bustamante, *DNA overwinds when stretched.*, *Nature* **442**(7104), 836–839 (2006)

- [26] C. Deufel, S. Forth, C. R. Simmons, S. Dejgoshia and M. D. Wang, *Nanofabricated quartz cylinders for angular trapping: DNA supercoiling torque detection.*, Nat Methods **4**(3), 223–225 (2007)
- [27] F. Mosconi, J. F. Allemand, D. Bensimon and V. Croquette, *Measurement of the torque on a single stretched and twisted DNA using magnetic tweezers.*, Phys Rev Lett **102**(7), 078301 (2009)
- [28] A. Crut, D. A. Koster, R. Seidel, C. H. Wiggins and N. H. Dekker, *Fast dynamics of supercoiled DNA revealed by single-molecule experiments.*, Proc Natl Acad Sci U S A **104**(29), 11957–11962 (2007)
- [29] D. Marenduzzo, E. Orlandini, A. Stasiak, D. W. Sumners, L. Tubiana and C. Micheletti, *DNA-DNA interactions in bacteriophage capsids are responsible for the observed DNA knotting.*, Proc Natl Acad Sci U S A **106**(52), 22269–22274 (2009)
- [30] A. A. Kornyshev and S. Leikin, *Sequence recognition in the pairing of DNA duplexes.*, Phys Rev Lett **86**(16), 3666–3669 (2001)
- [31] Y. Kao-Huang, A. Revzin, A. P. Butler, P. O’Conner, D. W. Noble and P. H. von Hippel, *Nonspecific DNA binding of genome-regulating proteins as a biological control mechanism: measurement of DNA-bound Escherichia coli lac repressor in vivo.*, Proc Natl Acad Sci U S A **74**(10), 4228–4232 (1977)
- [32] F. W. Schwarz, *The role of 1D diffusion for directional long-range communication on DNA.*, Ph.D. thesis, TU Dresden (2012)
- [33] D. Klaue, *DNA unwinding by helicases investigated on the single molecule level.*, Ph.D. thesis, TU Dresden (2012)
- [34] I. D. Vlamincx, T. Henighan, M. T. J. van Loenhout, I. Pfeiffer, J. Huijts, J. W. J. Kerssemakers, A. J. Katan, A. van Langen-Suurling, E. van der Drift, C. Wyman and C. Dekker, *Highly parallel magnetic tweezers by targeted DNA tethering.*, Nano Lett **11**(12), 5489–5493 (2011)
- [35] O. Otto, F. Czerwinski, J. L. Gornall, G. Stober, L. B. Oddershede, R. Seidel and U. F. Keyser, *Real-time particle tracking at 10,000 fps using optical fiber illumination.*, Opt Express **18**(22), 22722–22733 (2010)
- [36] J. Lipfert, X. Hao and N. H. Dekker, *Quantitative modeling and optimization of magnetic tweezers.*, Biophys J **96**(12), 5040–5049 (2009)
- [37] T. Butz, *Fouriertransformation für Fußgänger.*, fifth edition (B.G. Teubner Verlag, Wiesbaden, Germany, 2007)
- [38] P. Langevin, *Sur la theorie du mouvement Brownien.*, C R Acad Sci **146**, 530–532 (1908)

- [39] J. Howard, *Mechanics of motor proteins and the cytoskeleton*. (Sinauer Associates, Sunderland, MA, USA, 2001)
- [40] L. D. Landau, E. M. Lifshits and L. P. Pitaevskii, *Statistical physics.*, third edition (Pergamon Press, New York, NY, 1980)
- [41] K. C. Neuman, T. Lionnet and J. F. Allemand, *Single-molecule micromanipulation techniques.*, *Annu Rev Mater Res* **37**, 33–67 (2007)
- [42] Y. Harada, O. Ohara, A. Takatsuki, H. Itoh, N. Shimamoto and K. Kinoshita, *Direct observation of DNA rotation during transcription by Escherichia coli RNA polymerase.*, *Nature* **409**(6816), 113–115 (2001)
- [43] R. Seidel and C. Dekker, *Single-molecule studies of nucleic acid motors.*, *Curr Opin Struct Biol* **17**(1), 80–86 (2007)
- [44] D. A. Koster, K. Palle, E. S. M. Bot, M.-A. Bjornsti and N. H. Dekker, *Antitumour drugs impede DNA uncoiling by topoisomerase I.*, *Nature* **448**(7150), 213–217 (2007)
- [45] F. Kouzine, S. Sanford, Z. Elisha-Feil and D. Levens, *The functional response of upstream DNA to dynamic supercoiling in vivo.*, *Nat Struct Mol Biol* **15**(2), 146–154 (2008)
- [46] J. F. Marko and E. D. Siggia, *Statistical mechanics of supercoiled DNA.*, *Phys Rev E Stat Phys Plasmas Fluids Relat Interdiscip Topics* **52**(3), 2912–2938 (1995)
- [47] T. R. Strick, J. F. Allemand, D. Bensimon and V. Croquette, *Behavior of supercoiled DNA.*, *Biophys J* **74**(4), 2016–2028 (1998)
- [48] T. R. Strick, M. N. Dessinges, G. Charvin, N. H. Dekker, J. F. Allemand, D. Bensimon and V. Croquette, *Stretching of macromolecules and proteins.*, *Rep Prog Phys* **66**(1), 1–45 (2003)
- [49] S. Forth, C. Deufel, M. Y. Sheinin, B. Daniels, J. P. Sethna and M. D. Wang, *Abrupt buckling transition observed during the plectoneme formation of individual DNA molecules.*, *Phys Rev Lett* **100**(14), 148301 (2008)
- [50] J. D. Moroz and P. Nelson, *Entropic elasticity of twist-storing polymers.*, *Macromolecules* **31**(18), 6333–6347 (1998)
- [51] J. F. Marko, *Torque and dynamics of linking number relaxation in stretched supercoiled DNA.*, *Phys Rev E Stat Nonlin Soft Matter Phys* **76**(2 Pt 1), 021926 (2007)
- [52] B. C. Daniels, S. Forth, M. Y. Sheinin, M. D. Wang and J. P. Sethna, *Discontinuities at the DNA supercoiling transition.*, *Phys Rev E Stat Nonlin Soft Matter Phys* **80**(4 Pt 1), 040901 (2009)

- [53] J. D. Moroz and P. Nelson, *Torsional directed walks, entropic elasticity, and DNA twist stiffness.*, Proc Natl Acad Sci U S A **94**(26), 14418–14422 (1997)
- [54] N. Clauvelin, B. Audoly and S. Neukirch, *Elasticity and electrostatics of plectonemic DNA.*, Biophys J **96**(9), 3716–3723 (2009)
- [55] K. V. Klenin, A. V. Vologodskii, V. V. Anshelevich, A. M. Dykhne and M. D. Frank-Kamenetskii, *Computer simulation of DNA supercoiling.*, J Mol Biol **217**(3), 413–419 (1991)
- [56] R. Schöpflin, H. Brutzer, O. Müller, R. Seidel and G. Wedemann, *Probing the elasticity of DNA on short length scales by modeling supercoiling under tension.*, Biophys J **103**(2), 323–330 (2012)
- [57] S. Neukirch, *Extracting DNA twist rigidity from experimental supercoiling data.*, Phys Rev Lett **93**(19), 198107 (2004)
- [58] P. K. Purohit, *Plectoneme formation in twisted fluctuating rods.*, J Mech Phys Solids **56**(5), 1715–1729 (2008)
- [59] S. Goyal and N. C. Perkins, *Looping mechanics of rods and DNA with non-homogeneous and discontinuous stiffness.*, Int J Non-Linear Mechanics **43**(10, Sp. Iss. SI), 1121–1129 (2008)
- [60] J. Ubbink and T. Odijk, *Electrostatic-undulatory theory of plectonemically supercoiled DNA.*, Biophys J **76**(5), 2502–2519 (1999)
- [61] K. Klenin, H. Merlitz and J. Langowski, *A Brownian dynamics program for the simulation of linear and circular DNA and other wormlike chain polyelectrolytes.*, Biophys J **74**(2 Pt 1), 780–788 (1998)
- [62] J. A. Schellman and D. Stigter, *Electrical double layer, zeta potential, and electrophoretic charge of double-stranded DNA.*, Biopolymers **16**(7), 1415–1434 (1977)
- [63] S. van Dorp, U. F. Keyser, N. H. Dekker, C. Dekker and S. G. Lemay, *Origin of the electrophoretic force on DNA in solid-state nanopores.*, Nat Phys **5**(5), 347–351 (2009)
- [64] B. Luan and A. Aksimentiev, *Electro-osmotic screening of the DNA charge in a nanopore.*, Phys Rev E Stat Nonlin Soft Matter Phys **78**(2 Pt 1), 021912 (2008)
- [65] D. C. Rau and V. A. Parsegian, *Direct measurement of the intermolecular forces between counterion-condensed DNA double helices. Evidence for long range attractive hydration forces.*, Biophys J **61**(1), 246–259 (1992)
- [66] X. Qiu, L. W. Kwok, H. Y. Park, J. S. Lamb, K. Andresen and L. Pollack, *Measuring inter-DNA potentials in solution.*, Phys Rev Lett **96**(13), 138101 (2006)

- [67] A. Vologodskii and N. Cozzarelli, *Modeling of long-range electrostatic interactions in DNA.*, Biopolymers **35**(3), 289–296 (1995)
- [68] M. Hammermann, C. Steinmaier, H. Merlitz, U. Kapp, W. Waldeck, G. Chirico and J. Langowski, *Salt effects on the structure and internal dynamics of superhelical DNAs studied by light scattering and Brownian dynamics.*, Biophys J **73**(5), 2674–2687 (1997)
- [69] D. Stigter, *Interactions of highly charged colloidal cylinders with applications to double-stranded DNA*, Biopolymers **16**(7), 1435–1448 (1977)
- [70] S. L. Brenner and V. A. Parsegian, *A physical method for deriving the electrostatic interaction between rod-like polyions at all mutual angles.*, Biophys J **14**(4), 327–334 (1974)
- [71] D. Stigter, *The charged colloidal cylinder with a Gouy double layer.*, J. Colloid Interface Sci. **53**(2), 296–306 (1975)
- [72] D. Harries, *Solving the Poisson-Boltzmann equation for two parallel cylinders.*, Langmuir **14**(12), 3149–3152 (1998)
- [73] H. Zhang and J. F. Marko, *Maxwell relations for single-DNA experiments: Monitoring protein binding and double-helix torque with force-extension measurements.*, Phys Rev E Stat Nonlin Soft Matter Phys **77**(3 Pt 1), 031916 (2008)
- [74] A. V. Vologodskii and J. F. Marko, *Extension of torsionally stressed DNA by external force.*, Biophys J **73**(1), 123–132 (1997)
- [75] C. Maffeo, R. Schöpflin, H. Brutzer, R. Stehr, A. Aksimentiev, G. Wedemann and R. Seidel, *DNA-DNA interactions in tight supercoils are described by a small effective charge density.*, Phys Rev Lett **105**(15), 158101 (2010)
- [76] B. Luan and A. Aksimentiev, *DNA attraction in monovalent and divalent electrolytes.*, J Am Chem Soc **130**(47), 15754–15755 (2008)
- [77] C. G. Baumann, S. B. Smith, V. A. Bloomfield and C. Bustamante, *Ionic effects on the elasticity of single DNA molecules.*, Proc Natl Acad Sci U S A **94**(12), 6185–6190 (1997)
- [78] D. A. Koster, V. Croquette, C. Dekker, S. Shuman and N. H. Dekker, *Friction and torque govern the relaxation of DNA supercoils by eukaryotic topoisomerase IB.*, Nature **434**(7033), 671–674 (2005)
- [79] A. A. Brian, H. L. Frisch and L. S. Lerman, *Thermodynamics and equilibrium sedimentation analysis of the close approach of DNA molecules and a molecular ordering transition.*, Biopolymers **20**(6), 1305–1328 (1981)

- [80] V. V. Rybenkov, N. R. Cozzarelli and A. V. Vologodskii, *Probability of DNA knotting and the effective diameter of the DNA double helix.*, Proc Natl Acad Sci U S A **90**(11), 5307–5311 (1993)
- [81] V. V. Rybenkov, A. V. Vologodskii and N. R. Cozzarelli, *The effect of ionic conditions on the conformations of supercoiled DNA. II. Equilibrium catenation.*, J Mol Biol **267**(2), 312–323 (1997)
- [82] A. V. Vologodskii, S. D. Levene, K. V. Klenin, M. Frank-Kamenetskii and N. R. Cozzarelli, *Conformational and thermodynamic properties of supercoiled DNA.*, J Mol Biol **227**(4), 1224–1243 (1992)
- [83] S. W. Kowalczyk, D. B. Wells, A. Aksimentiev and C. Dekker, *Slowing down DNA translocation through a nanopore in lithium chloride.*, Nano Lett **12**(2), 1038–1044 (2012)
- [84] K. Günther, M. Mertig and R. Seidel, *Mechanical and structural properties of YOYO-1 complexed DNA.*, Nucleic Acids Res **38**(19), 6526–6532 (2010)
- [85] C. Bustamante, J. F. Marko, E. D. Siggia and S. Smith, *Entropic elasticity of lambda-phage DNA.*, Science **265**(5178), 1599–1600 (1994)
- [86] C. Bouchiat, M. D. Wang, J. Allemand, T. Strick, S. M. Block and V. Croquette, *Estimating the persistence length of a worm-like chain molecule from force-extension measurements.*, Biophys J **76**(1 Pt 1), 409–413 (1999)
- [87] P. A. Wiggins, T. van der Heijden, F. Moreno-Herrero, A. Spakowitz, R. Phillips, J. Widom, C. Dekker and P. C. Nelson, *High flexibility of DNA on short length scales probed by atomic force microscopy.*, Nat. Nanotechnol. **1**(2), 137–141 (2006)
- [88] M. Hinczewski, Y. von Hansen and R. R. Netz, *Deconvolution of dynamic mechanical networks.*, Proc Natl Acad Sci U S A **107**(50), 21493–21498 (2010)
- [89] M. T. J. van Loenhout, M. V. de Grunt and C. Dekker, *Dynamics of DNA supercoils.*, Science (2012)
- [90] A. Dawid, F. Guillemot, C. Brème, V. Croquette and F. Heslot, *Mechanically controlled DNA extrusion from a palindromic sequence by single molecule micromanipulation.*, Phys Rev Lett **96**(18), 188102 (2006)
- [91] N. Sigal and B. Alberts, *Genetic recombination: the nature of a crossed strand-exchange between two homologous DNA molecules.*, J Mol Biol **71**(3), 789–793 (1972)
- [92] S. Forth, C. Deufel, S. S. Patel and M. D. Wang, *Direct measurements of torque during Holliday junction migration.*, Biophys J **101**(2), L5–L7 (2011)

- [93] D. Klaue and R. Seidel, *Torsional stiffness of single superparamagnetic microspheres in an external magnetic field.*, Phys Rev Lett **102**(2), 028302 (2009)
- [94] J. R. Moffitt, Y. R. Chemla, D. Izhaky and C. Bustamante, *Differential detection of dual traps improves the spatial resolution of optical tweezers.*, Proc Natl Acad Sci U S A **103**(24), 9006–9011 (2006)
- [95] M. P. Landry, P. M. McCall, Z. Qi and Y. R. Chemla, *Characterization of photoactivated singlet oxygen damage in single-molecule optical trap experiments.*, Biophys J **97**(8), 2128–2136 (2009)
- [96] V. Bormuth, V. Varga, J. Howard and E. Schäffer, *Protein friction limits diffusive and directed movements of kinesin motors on microtubules.*, Science **325**(5942), 870–873 (2009)
- [97] A. Ishijima, H. Kojima, T. Funatsu, M. Tokunaga, H. Higuchi, H. Tanaka and T. Yanagida, *Simultaneous observation of individual ATPase and mechanical events by a single myosin molecule during interaction with actin.*, Cell **92**(2), 161–171 (1998)
- [98] A. Sarkar, R. B. Robertson and J. M. Fernandez, *Simultaneous atomic force microscope and fluorescence measurements of protein unfolding using a calibrated evanescent wave.*, Proc Natl Acad Sci U S A **101**(35), 12882–12886 (2004)
- [99] K. Bacia and P. Schuille, *Practical guidelines for dual-color fluorescence cross-correlation spectroscopy.*, Nat Protoc **2**(11), 2842–2856 (2007)
- [100] W. Denk, J. H. Strickler and W. W. Webb, *Two-photon laser scanning fluorescence microscopy*, Science **248**(4951), 73–76 (1990)
- [101] T. A. Klar, S. Jakobs, M. Dyba, A. Egner and S. W. Hell, *Fluorescence microscopy with diffraction resolution barrier broken by stimulated emission.*, Proc Natl Acad Sci U S A **97**(15), 8206–8210 (2000)
- [102] D. Toomre and D. J. Manstein, *Lighting up the cell surface with evanescent wave microscopy.*, Trends Cell Biol **11**(7), 298–303 (2001)
- [103] D. Axelrod, *Total internal reflection fluorescence microscopy in cell biology.*, Traffic **2**(11), 764–774 (2001)
- [104] M. Tokunaga, K. Kitamura, K. Saito, A. H. Iwane and T. Yanagida, *Single molecule imaging of fluorophores and enzymatic reactions achieved by objective-type total internal reflection fluorescence microscopy*, Biochem Biophys Res Commun **235**(1), 47–53 (1997)
- [105] C. M. Ajo-Franklin, C. Yoshina-Ishii and S. G. Boxer, *Probing the structure of supported membranes and tethered oligonucleotides by fluorescence interference contrast microscopy*, Langmuir **21**(11), 4976–4983 (2005)

- [106] J. Kerssemakers, J. Howard, H. Hess and S. Diez, *The distance that kinesin-1 holds its cargo from the microtubule surface measured by fluorescence interference contrast microscopy.*, Proc Natl Acad Sci U S A **103**(43), 15812–15817 (2006)
- [107] W. L. Barnes, A. Dereux and T. W. Ebbesen, *Surface plasmon subwavelength optics.*, Nature **424**(6950), 824–830 (2003)
- [108] K. Elsayad and K. G. Heinze, *Defining a superlens operating regime for imaging fluorescent molecules.*, PLoS One **4**(12), e7963 (2009)
- [109] J. Mertz, *Optical sectioning microscopy with planar or structured illumination.*, Nat Methods **8**(10), 811–819 (2011)
- [110] P. Lemmer, M. Gunkel, D. Baddeley, R. Kaufmann, A. Urich, Y. Weiland, J. Reymann, P. Muller, M. Hausmann and C. Cremer, *SPDM: light microscopy with single-molecule resolution at the nanoscale*, Appl Phys B: Lasers Opt **93**(1), 1–12 (2008)
- [111] M. J. Nasse and J. C. Woehl, *Realistic modeling of the illumination point spread function in confocal scanning optical microscopy.*, J Opt Soc Am A **27**(2), 295–302 (2010)
- [112] M. Singh-Zocchi, S. Dixit, V. Ivanov and G. Zocchi, *Single-molecule detection of DNA hybridization.*, Proc Natl Acad Sci U S A **100**(13), 7605–7610 (2003)
- [113] C. Gell, M. Berndt, J. Enderlein and S. Diez, *TIRF microscopy evanescent field calibration using tilted fluorescent microtubules.*, J Microsc **234**(1), 38–46 (2009)
- [114] A. L. Mattheyses and D. Axelrod, *Direct measurement of the evanescent field profile produced by objective-based total internal reflection fluorescence.*, J Biomed Opt **11**(1), 014006 (2006)
- [115] J. Enderlein and M. Böhmer, *Influence of interface-dipole interactions on the efficiency of fluorescence light collection near surfaces.*, Opt Lett **28**(11), 941–943 (2003)
- [116] E. M. Puchner, S. K. Kufer, M. Strackharn, S. W. Stahl and H. E. Gaub, *Nanoparticle self-assembly on a DNA-scaffold written by single-molecule cut-and-paste.*, Nano Lett **8**(11), 3692–3695 (2008)
- [117] J. C. Sutherland and K. P. Griffin, *Absorption spectrum of DNA for wavelengths greater than 300 nm.*, Radiat Res **86**(3), 399–409 (1981)
- [118] S. Sindbert, S. Kalinin, H. Nguyen, A. Kienzler, L. Clima, W. Bannwarth, B. Appel, S. Müller and C. A. M. Seidel, *Accurate distance determination of nucleic acids via Förster resonance energy transfer: implications of dye linker length and rigidity.*, J Am Chem Soc **133**(8), 2463–2480 (2011)

- [119] T. Ramreddy, R. Sachidanandam and T. R. Strick, *Real-time detection of cruciform extrusion by single-molecule DNA nanomanipulation.*, Nucleic Acids Res **39**(10), 4275–4283 (2011)
- [120] J. D. Jackson, *Classical electrodynamics.*, third edition (John Wiley & Sons, Inc., New York, NY, USA, 1998)
- [121] D. Axelrod, E. Hellen and R. Fulbright, *Total internal reflection fluorescence.*, volume 3 (Springer US, New York, NY, USA, 1992)
- [122] U. F. Keyser, D. Krapf, B. N. Koeleman, R. M. M. Smeets, N. H. Dekker and C. Dekker, *Nanopore tomography of a laser focus.*, Nano Lett **5**(11), 2253–2256 (2005)
- [123] A. Hillisch, M. Lorenz and S. Diekmann, *Recent advances in FRET: distance determination in protein-DNA complexes.*, Curr Opin Struct Biol **11**(2), 201–207 (2001)
- [124] T. Härtling, P. Reichenbach and L. M. Eng, *Near-field coupling of a single fluorescent molecule and a spherical gold nanoparticle.*, Opt Express **15**(20), 12806–12817 (2007)
- [125] N. Luzzietti, S. Knappe, I. Richter and R. Seidel, *Nicking enzyme-based internal labeling of DNA at multiple loci.*, Nat Protoc **7**(4), 643–653 (2012)
- [126] T. E. Cloutier and J. Widom, *DNA twisting flexibility and the formation of sharply looped protein-DNA complexes.*, Proc Natl Acad Sci U S A **102**(10), 3645–3650 (2005)
- [127] B. Luan and A. Aksimentiev, *Electric and electrophoretic inversion of the DNA charge in multivalent electrolytes.*, Soft Matter **6**, 243–246 (2010)
- [128] D. J. Kauert, T. Kurth, T. Liedl and R. Seidel, *Direct mechanical measurements reveal the material properties of three-dimensional DNA origami.*, Nano Lett **11**(12), 5558–5563 (2011)
- [129] N. Luzzietti, H. Brutzer, D. Klaue, F. W. Schwarz, W. Staroske, S. Clausing and R. Seidel, *Efficient preparation of internally modified single-molecule constructs using nicking enzymes.*, Nucleic Acids Res **39**(3), e15 (2011)

List of Figures

1.1. Supercoiling of a circular ribbon	8
2.1. Schematic illustration of the magnetic tweezers apparatus	14
2.2. Real-time three dimensional tracking of an immobilized microsphere .	18
2.3. Real-time 3D differential tracking of two immobilized microspheres .	19
2.4. Mimicked motion of a fixed particle by moving the piezo stage	20
2.5. 3D tracking of a magnetic microsphere tethered to a DNA molecule .	21
2.6. Mimicked motion of a microsphere tethered to a DNA molecule . . .	23
2.7. Force calculation from the microsphere fluctuations	24
3.1. Buckling transition at different ionic strengths and DNA lengths . . .	30
3.2. Equilibrium occupancy of pre- and postbuckling state	32
3.3. Kinetics of the buckling transition	34
3.4. Mean position of the pre- and postbuckling state	36
3.5. Slopes from the supercoiling curves vs. theoretical predictions	38
3.6. Supercoiling curves vs. predictions from the end loop model	39
3.7. Force dependence of the buckling transition	42
3.8. Salt dependence of the buckling transition	43
3.9. Supercoiling kinked DNA	44
4.1. Dependence of DNA supercoiling on force and salt concentration . . .	48
4.2. Electrostatic potential around the DNA	49
4.3. Interaction energies and forces between two DNA molecules	50
4.4. Supercoiling slopes for different amounts of charge adaptation	51
4.5. Charge adaptation model vs. data from Croquette and coworkers . .	52
4.6. Coarse-grained Monte Carlo simulations of DNA supercoiling	53
4.7. Molecular dynamics simulations of two interacting DNA molecules . .	54
4.8. The distribution of monovalent ions around double-stranded DNA . .	55
4.9. Charge distribution and potential around double-stranded DNA . . .	56
4.10. Fluctuations of the superhelical radius for various forces	58
4.11. Model predictions including fluctuations	59
4.12. Entropic contributions to superhelix formation	60
4.13. DNA force-extension characteristics for different counterions	66
4.14. Dependence of DNA supercoiling on the type of counterion	67
4.15. Force dependence of the supercoiling slopes for different counterions .	68
4.16. Dependence of the buckling transition on the type of counterion . . .	69
5.1. Branch migration of a Holliday junction	72
5.2. Extrusion of the Holliday junction in the magnetic tweezers	73
5.3. Modeling branch migration as a system of coupled springs	76

5.4.	Branch migration for different amounts of applied turns	79
5.5.	Salt dependence of the branch migration	81
6.1.	Scanning evanescent fields using a nanomechanical DNA gear	85
6.2.	Instrument combining magnetic tweezers and TIRF microscopy	86
6.3.	Determination of the angle of incidence.	88
6.4.	Linear translation of a quantum dot through an evanescent field	89
6.5.	Intensity decay measured for conventional widefield illumination	90
6.6.	Excitation intensity profiles for various angles of incidence	91
6.7.	Dependence of the penetration depth on the angle of incidence	92

List of Publications

Chapter 3

- H. Brutzer, N. Luzziatti, D. Klaue and R. Seidel
Energetics at the DNA supercoiling transition.
Biophys. J. **98**(7), 1267-1276 (2010)
- N. Luzziatti, H. Brutzer, D. Klaue, F. W. Schwarz, W. Staroske, S. Clausing and R. Seidel
Efficient preparation of internally modified single-molecule constructs using nicking enzymes.
Nucleic Acids Res. **39**(3), e15 (2011)
- R. Schöpflin, H. Brutzer, O. Müller, R. Seidel and G. Wedemann
Probing the elasticity of dna on short length scales by modeling supercoiling under tension.
Biophys. J. **103**(2), 323-330 (2012)

Chapter 4

- C. Maffeo*, R. Schöpflin*, H. Brutzer*, R. Stehr, A. Aksimentiev, G. Wedemann and R. Seidel
DNA-DNA interactions in tight supercoils are described by a small effective charge density.
Phys. Rev. Lett. **105**(15), 158101 (2010)

Chapter 6

- H. Brutzer*, F. W. Schwarz* and R. Seidel
Scanning evanescent fields using a pointlike light source and a nanomechanical DNA gear.
Nano Lett. **12**(1), 473-478 (2012)

Earlier work

- C. Wagner, C. Olbrich, H. Brutzer, M. Salomo, U. Kleinekathöfer, U. F. Keyser and F. Kremer
DNA condensation by TmHU studied by optical tweezers, AFM and molecular dynamics simulations.
J. Biol. Phys. **37**(1) 117-131 (2011)

*These authors contributed equally to this paper.

Abbreviations and nomenclature

α	deflection angle of a pendulum
χ_{CA}	charge adaptation factor
χ_{PB}	correction for linearizing Poisson-Boltzmann equation
χ_{rod}	correction for cylindrical geometry of the DNA
ΔL_1	length reduction for the end loop
ΔN_b	amount of twist transferred into writhe during buckling
ΔN_b^{post}	twist difference between transition and postbuckl. state
ΔN_b^{pre}	twist difference between transition and prebuckling state
ΔN_b^P	mean writhe transferred during buckling (end loop model)
δz_{DNA}	DNA extension change of the non-branched region
δz_{Hj}	DNA extension change of the Holliday junction
δz_{total}	total DNA extension change
$\delta \vartheta_{Hj}$	rotation change of the Holliday junction
Δ_{Hj}	length change per migration step of the Holliday junction
η	viscosity
Γ	mean torque of the DNA
γ	drag coefficient
γ_{Hj}	friction coefficient at the Holliday junction
γ_{trans}	translational drag coefficient of the microsphere
λ	wavelength of the incident light
λ_D	Debye length
\bar{I}_{ex}	normalized excitation intensity
\bar{I}_m	normalized intensity measured in TIRF illumination

\bar{I}_m^{CW}	normalized intensity measured in CW illumination
Φ	electrostatic potential
ρ	superhelical radius
dL/dN	slope of the supercoiling curves after buckling
τ^c	time const. of the contrib. of drag to the eq. of mot.
τ^{inert}	time const. of the inertial contrib. to the eq. of mot.
τ_b	mean residence time at the buckling transition
τ_b^{post}	mean residence time for the postbuckling state
τ_b^{pre}	mean residence time for the prebuckling state
θ	angle of incidence
θ_{max}	half-angle of the maximum light cone exiting an objective
ξ	nominal charge density of the DNA
ξ^*	adapted charge density of the DNA
a	radius of the DNA (cylinder approximation)
b	displacement of the beam from the optical axis
b_{max}	maximal displacement of the beam from the optical axis
C	torsional modulus of the DNA
C_s	effective torsional modulus of the DNA
D	diameter of the exit pupil
d	penetration depth of an evanescent field
d_{eff}	diameter of the effective hard-wall potential
D_{Hj}	diffusion coefficient for spontaneous branch migration
d_r	confinement length of the DNA
e	elementary charge
$E_{\text{bend}}^{\text{DNA}}$	bending energy of the DNA within the superhelix
$E_{\text{Estat}}^{\text{DNA}}$	DNA-DNA electrostatic interaction energy
$E_{\text{pot}}^{\text{force}}$	potential energy change due to shortening of the DNA

$E_{\text{tot}}^{\text{sh}}$	energy per added turn to form an ideal DNA superhelix
E_1	free energy for the first turn of writhe in the plectoneme
E_2	free energy for every but the first turn in the plectoneme
E_{b}	free energy penalty of the DNA for undergoing buckling
E_{entr}	entropic energy of the DNA
E_{osc}	mean energy of an oscillator
$E_{\text{post},0}^{\text{p}}$	mean free energy after buckling (end loop model)
E_{post}	free energy of the DNA after buckling
$E_{\text{post}}^{\text{p}}$	free energy after buckling (end loop model)
E_{pre}	free energy of the DNA prior to buckling
F	applied force
f	frequency
F_{b}	restoring force of a pendulum
f_c	cutoff frequency
F_{Hj}	thermal force driving spontaneous branch migration
F_{mag}	force applied in the stretching direction
F_{obj}	fluorescent object function
f_{obj}	focal length of the objective
f_{therm}	thermal force
F_{trans}	thermal force acting on the microsphere
g	negative free energy of stretched, nicked DNA
h	superhelical repeat length
h_{DNA}	helical pitch of the DNA
I_{em}	emitted intensity from a probe
I_{ex}	excitation intensity
I_{m}	measured intensity emitted from a probe
I_{m}^{CW}	measured intensity in conventional widefield illumination

K_1	1 st order modified Bessel function of the second kind
k_B	Boltzmann constant
k_{DNA}	trap stiffness in the non-branched region
k_{Hj}	trap stiffness in the extruded arms
k_y	trap stiffness
L	mean length of the DNA
L_0	contour length of the DNA
l_B	Bjerrum length
L_{jump}	jump size at the buckling transition
m	mass of the particle
N	number of turns added to the DNA
n	index of refraction
n_1	index of refraction on the objective side of the interface
n_2	index of refraction on the sample side of the interface
N_b	number of turns added to the DNA at the buckling point
N_b^P	turns added at the buckling point (end loop model)
$N_{\text{wr},0}$	mean number of turns of writhe in the plectoneme
N_{wr}	number of turns of writhe in the plectoneme
NA	numerical aperture of an objective
P	plectonemic twist stiffness
p	bending persistence length of the DNA
p_{post}	probability that the postbuckling state is occupied
p_p	probability for the postbuckling state (end loop model)
p_{tor}	torsional persistence length of the DNA
PSF	point spread function
R	radius of the end loop
r	distance between the two double-strands

R_{\min}	radius of the end loop for minimum energy
R_s	radius of a sphere
$R_{f\text{ therm}}$	autocorrelation function of the thermal force
s	position of the center-line of one double-strand
T	absolute temperature
t	time
t_{step}	time per step during spontaneous branch migration
z	relative extension of the DNA
Z_c	power spectral density of a coupled system
2D	two-dimensional
3D	three-dimensional
AFM	atomic force microscopy
bp	base pair
BSA	bovine serum albumin
CCD	charge-coupled device
CMOS	complementary metal–oxide–semiconductor
CPU	central processing unit
CW	conventional widefield
D-loop	displacement loop
DAQ	data acquisition
DH	Debye-Hückel
DNA	deoxyribonucleic acid
DTT	dithiothreitol
EDTA	ethylenediaminetetraacetic acid
EMCCD	electron-multiplying charge-coupled device
FPN	fixed-pattern noise
FRET	fluorescence resonance energy transfer

LED	light emitting diode
MC	Monte Carlo
MD	molecular dynamics
MSD	mean square displacement
PB	Poisson-Boltzmann
PBS	phosphate buffered saline
PSD	power spectral density
RMS	root mean square displacement
RNA	ribonucleic acid
TAE	mixture of TRIS base, acetic acid, and EDTA
TIRF	total internal reflection fluorescence
TRIS	tris(hydroxymethyl)aminomethane
WLC	worm-like chain

Appendix

A. Preparation of the fluidic chamber

At first the two holes in the top cover slide of the fluidic chamber as well as the Parafilm (Pechiney Plastic Packaging Company, Chicago, IL, USA) that serves as a spacer between bottom and top slide were prepared using a laser cutter (Speedy 100, Trotec, Marchtrenk, Austria). Then bottom and top slides were cleaned thoroughly by ultrasonication for 10 min first in double-distilled water, then in acetone (Merck, Darmstadt, Germany), and finally in isopropanol (Merck). Next the slides were removed from the solution and dried by a stream of nitrogen.

The bottom slide was spin-coated (Polos Spin 150, Cpk Industries, Harleysville, PA, USA) with polystyrene (100 kDa, Sigma-Aldrich, St. Louis, MO, USA) dissolved in toluene (Merck) to create a hydrophobic surface: 50 μl of 1% polystyrene-toluene solution was quickly pipetted onto the glass at 6000 rpm and dried by further spinning for 1 min. Afterwards the coated slides were placed in an oven for 1 h at 150°C.

Then the spacer made of Parafilm was placed between bottom and top slides and used to fuse the slides together on a heating plate at 100°C. The assembled flow cell was mounted onto a custom-made holder, with an inlet and outlet connector. The outlet is connected by a small tube to a syringe pump to fill the fluidic chamber with liquid and allow an exchange of the solution. Then 200 μl of a solution containing 1 M NaCl was flushed into the chamber.

Carboxylated latex microspheres (Invitrogen, Carlsbad, CA, USA), which were used as immobilized reference particles, were diluted 1:500 in 300 mM NaCl. 20 μl of this dilution were washed 3 times by centrifugation for 3 min at 16,000 g, subsequent removal of the supernatant, and resuspension in 20 μl of 10 mM TRIS-HCl with 300 mM NaCl. Then 1 μl of the washed beads was diluted with 29 μl of 1 M NaCl, flushed into the flow cell, and incubated for 1 h.

For the experiments with DNA, the fluidic chamber was subsequently flushed with 200 μl of phosphate buffered saline (PBS) and then with a solution containing 50 $\mu\text{g}/\text{ml}$ of anti-digoxigenin (Roche, Penzberg, Germany) in PBS. The flow cell was incubated with the antibody for approximately 1 h. Afterwards the flow cell was incubated with BSA (NEB, Ipswich, MA, USA) for 1 h to prevent unspecific binding to the hydrophobic surface. Finally the unbound BSA was removed by flushing with 1 ml of PBS.

B. DNA substrate preparation

B.1. DNA buckling transition and effective charge studies

The shorter substrate for the supercoiling experiments in chapters 3 and 4 was prepared by cutting a custom-made plasmid (pAMS3) using the restriction enzymes *XhoI* and *PvuI*, providing a linear fragment of 1865 bp length with corresponding sticky ends on either side. Biotin- or digoxigenin-modified tails were made by digesting a 1.2 kbp biotin- and a digoxigenin dUTP-labeled PCR fragment from plasmid pBluescript II SK+ (Stratagene, La Jolla, CA, USA) with *XhoI* or *PvuI*, respectively, approximately in the middle of the fragments. The labeled fragments were subsequently ligated to the 1865 bp fragment. The longer (10.9 kbp) substrate was prepared similarly by digesting an appropriate plasmid and the labeled tails with *PciI* and *SacI*.

The kinked DNA substrate (1845 bp) was prepared from a plasmid containing five directly repeated *BbvCI* sites with 16 bp spacing [129]. The plasmid was nicked at the *BbvCI* sites using *Nt.BbvCI* and simultaneously cut with *BsrGI* and *PspOMI*. The single-stranded gap resulting from the nicking reaction was filled with a DNA single strand containing a 20 bp hairpin. Subsequently the DNA fragment was ligated as described above to labeled tails cut with *BsrGI* and *PspOMI*.

B.2. Intramolecular friction of a migrating Holliday junction

The DNA substrate used for the spontaneous branch migration studies contained an inverted repeat (see Fig. 5.1b) and was prepared in a one-pot reaction by ligating four individual fragments through suitable sticky ends:* These fragments are in particular two labeled tails, a fragment containing a short spacer and half of the inverted repeat as well as a fragment containing the other half of the repeat. The two fragments forming the inverted repeat were prepared from a 8778 bp long custom-made plasmid (pBluescript+1+2+4 lambda frag).

The fragment containing the spacer and half of the inverted repeat was prepared by digesting the plasmid with *PspOMI* and *PciI*. The desired fragment was gel-purified.

The fragment containing the other half of the inverted repeat was prepared by digesting the plasmid with *XbaI*, *XhoI*, and *PciI*. The longest of the three resulting fragments was gel-purified.

Labeled tail fragments were made by digesting a 1.2 kbp biotin- and a digoxigenin dUTP-labeled PCR fragment from plasmid pBluescript II SK+ (Stratagene, La Jolla, CA, USA) with *PspOMI* and *XhoI*, respectively, approximately in the middle of the fragments.

*This DNA sample was prepared by Sylvia Clausing.

The DNA fragments were purified with a commercial PCR clean-up kit, mixed together and ligated with T4 ligase at 16°C overnight. The resulting mix of ligation products was separated on an 1.0% TAE agarose gel. Then the desired construct of ~10.6 kbp length was purified from the gel carefully avoiding any exposure to ethidium bromide and UV light.

B.3. DNA Holliday junction as a nanomechanical gear

The DNA substrate containing the inverted repeat for the evanescent-field calibration studies (see Fig. 6.1a) was prepared in a one-pot reaction by ligating four individual fragments through suitable sticky ends.[†] These fragments are in particular the two labeled tails, a fragment containing the spacer with the internal biotinylations and half of the inverted repeat as well as a fragment containing the other half of the repeat. The two fragments forming the inverted repeat were prepared from the 6868 bp long plasmid pNLrep, which carries a region with five equally spaced (15-16 bp) target sites for the nicking enzyme *Nt.BbvCI* at which the internal biotin modifications are introduced [129]. A unique site for the restriction enzyme *SacI* is located ~4.5 kbp upstream of this region. Unique sites for the restriction enzymes *EcoRI* and *XbaI* are situated 7 bp and 2.2 kbp downstream of the region, respectively.

The fragment containing the spacer with the internal biotinylations and half of the inverted repeat was prepared by digesting pNLrep with *SacI*, *XbaI* and *Nt.BbvCI*. Subsequently a 63 bp long phosphorylated insert oligomer with two internal 11 bp spaced biotin modifications was added, that replaces the 15-16 bp long fragments resulting from the nicking reaction. The solution was heated to 80°C for 2 min and slowly cooled down to 20°C to allow the replace to occur. The fragment containing the other half of the inverted repeat was prepared by digesting pNLrep with *EcoRI* and *XbaI*.

Labeled tail fragments were made by digesting a 1.2 kbp fluorescein- and a digoxigenin dUTP-labeled PCR fragment from plasmid pBluescript II SK+ (Stratagene, La Jolla, CA, USA) with *SacI* and *EcoRI*, respectively, approximately in the middle of the fragments.

The DNA fragments were purified with a commercial PCR clean-up kit, mixed together and ligated with T4 ligase at 16°C overnight. The resulting mix of ligation products was separated on an 0.7% TAE agarose gel. Then the desired construct of ~10.1 kbp length was purified from the gel carefully avoiding any exposure to ethidium bromide and UV light.

[†]This DNA sample was prepared by Friedrich W. Schwarz.

Acknowledgements

Finally, I would like to thank everyone who helped me carry out my work in the past four years. I believe that more people than I can think of contributed to the success of my project, from the staff taking care of cleaning the office windows up to the tax payer providing the funding. Some of them I would like to mention in particular.

I thank Dr. Ralf Seidel for accepting me as a research student in his lab and for the excellent mentoring throughout the entire project. A supervisor who comes into the lab himself to help solve problems and has the experience to envision future trends in the field is hard to find.

Furthermore I'd like to thank Prof. Dr. Stefan Diez from the B CUBE for reviewing and examining as well as Prof. Dr. Klaus Kroy from the University of Leipzig for reviewing.

Great thanks also to our collaborators: Prof. Dr. Gero Wedemann and his lab at the University of Applied Sciences in Stralsund, in particular Robert Schöpflin for the Monte Carlo simulations on DNA supercoiling and, more importantly, the mutual visits and fruitful discussions. Also I'd like to thank Prof. Dr. Aleksei Aksimentiev and Christopher Maffeo at the University of Illinois in Urbana Champaign for the molecular dynamics simulations on the charge distribution around DNA.

From the first to the last day of my work I was in the lucky situation to be around some great scientists and, for me more importantly, colleagues. That's why I would like to thank: Nicholas Luzzietti for showing a physicist that it is indeed advantageous to wear gloves when working with biological matter...and many other useful things. Daniel Klaue for sharing his immense knowledge on handling magnetic tweezers, writing a thesis, and, last but not least, windsurfing. Friedrich W. Schwarz for trusting me the MTP miracle machine and introducing me to the world of fluorescence. Dominik Kauert for right on the spot help and taking care of virtually anything my computer did to annoy me. Claudius Hammer for taking on with a remarkable persistence and neatness a tricky project (which originally wasn't intended to be his). Alexander Huhle for making all my LabVIEW dreams come true. Jasmina Dikic for making sure that there is no biological nonsense written in this work. Sylvia Clausing for the thorough preparation of constructs. Isabel Richter for taking on the obnoxious but indispensable job of building flow cells. Heike Neumann for dealing with all the behind-the-scenes paperwork.

Many thanks also to Don and Wendy Storey for, once more, great proofreading, encouraging comments, and, most of all, providing me with the linguistic skills for this work.

I would like to mention my parents, Hilde and Roland Brutzer, who more than just once spontaneously drove across Germany to help out with all kinds of little and big things/persons.

Lastly, greatest thank to my wife Melissa, who left everything that mattered to her

behind and came all the way across the Atlantic, just so that I could carry out this thesis. Similarly, Emilio and *N.N.* were never asked to compensate Papi's stress but did so with divine patience.

Erklärung

Hiermit versichere ich, dass ich die vorliegende Arbeit ohne unzulässige Hilfe Dritter und ohne Benutzung anderer als der angegebenen Hilfsmittel angefertigt habe; die aus fremden Quellen direkt oder indirekt übernommenen Gedanken sind als solche kenntlich gemacht. Die Arbeit wurde bisher weder im Inland noch im Ausland in gleicher oder ähnlicher Form einer anderen Prüfungsbehörde vorgelegt.

Die Dissertation wurde im Zeitraum vom 15. Oktober 2008 bis 29. November 2012 verfasst und von Prof. Dr. Stefan Diez, B CUBE der Technischen Universität Dresden, betreut.

Weiterhin versichere ich hiermit, dass keine früheren erfolglosen Promotionsverfahren stattgefunden haben.

Ich erkenne die Promotionsordnung der Fakultät für Mathematik und Naturwissenschaften, Technische Universität Dresden an.

Hergen Brutzer

Dresden, 29. November 2012